

AFRL-IF-RS-TR-2001-160
Final Technical Report
August 2001



MICRO-FLOW STUDIES IN THE 1 TO 50 MICRON DOMAIN

Saddleback Aerospace Corporation

Sponsored by
Defense Advanced Research Projects Agency
DARPA Order No. G220/4

APPROVED FOR PUBLIC RELEASE; DISTRIBUTION UNLIMITED.

The views and conclusions contained in this document are those of the authors and should not be interpreted as necessarily representing the official policies, either expressed or implied, of the Defense Advanced Research Projects Agency or the U.S. Government.


AIR FORCE RESEARCH LABORATORY
INFORMATION DIRECTORATE
ROME RESEARCH SITE
ROME, NEW YORK

20020308 043

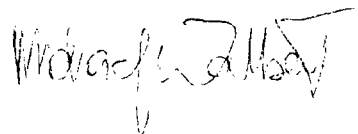
This report has been reviewed by the Air Force Research Laboratory, Information Directorate, Public Affairs Office (IFOIPA) and is releasable to the National Technical Information Service (NTIS). At NTIS it will be releasable to the general public, including foreign nations.

AFRL-IF-RS-TR-2001-160 has been reviewed and is approved for publication.

APPROVED:


GEORGE O. RAMSEYER
Project Engineer

FOR THE DIRECTOR:



MICHAEL L. TALBERT, Technical Advisor
Information Technology Division
Information Directorate

If your address has changed or if you wish to be removed from the Air Force Research Laboratory Rome Research Site mailing list, or if the addressee is no longer employed by your organization, please notify AFRL/IFTC, 26 Electronic Pky, Rome, NY 13441-4514. This will assist us in maintaining a current mailing list.

Do not return copies of this report unless contractual obligations or notices on a specific document require that it be returned.

MICRO-FLOW STUDIES IN THE 1 TO 50 MICRON DOMAIN

Geoffrey Campbell, David Underwood,
Brian Leung, David Paquette,
Richard Nelson, and Mark Bachman

Contractor: Saddleback Aerospace Corporation
Contract Number: F30602-98-C-0146
Effective Date of Contract: 11 September 1998
Contract Expiration Date: 10 September 2001
Short Title of Work: Micro-Flow Studies in the 1 to 50
Micron Domain
Period of Work Covered: Sep 98 - Sep 01

Principal Investigator: Geoffrey Campbell
Phone: (303) 776-1721
AFRL Project Engineer: George O. Ramseyer
Phone: (315) 330-3492

APPROVED FOR PUBLIC RELEASE; DISTRIBUTION
UNLIMITED.

This research was supported by the Defense Advanced Research
Projects Agency of the Department of Defense and was monitored
by George O. Ramseyer, AFRL/IFTC, 26 Electronic Pky, Rome, NY.

REPORT DOCUMENTATION PAGE			Form Approved OMB No. 0704-0188	
<small>Public reporting burden for this collection of information is estimated to average 1 hour per response, including the time for reviewing instructions, searching existing data sources, gathering and maintaining the data needed, and completing and reviewing the collection of information. Send comments regarding this burden estimate or any other aspect of this collection of information, including suggestions for reducing this burden, to Washington Headquarters Services, Directorate for Information Operations and Reports, 1215 Jefferson Davis Highway, Suite 1204, Arlington, VA 22202-4302, and to the Office of Management and Budget, Paperwork Reduction Project (0704-0188), Washington, DC 20503.</small>				
1. AGENCY USE ONLY (Leave blank)		2. REPORT DATE AUGUST 2001		3. REPORT TYPE AND DATES COVERED Final Sep 98 - Sep 01
4. TITLE AND SUBTITLE MICRO-FLOW STUDIES IN THE 1 TO 50 MICRON DOMAIN			5. FUNDING NUMBERS C - F30602-98-C-0146 PE - 63739E PR - E117 TA - 00 WU - 37	
6. AUTHOR(S) Geoffrey Campbell, David Underwood, Brian Leung, David Paquette, Richard Nelson, and Mark Bachman				
7. PERFORMING ORGANIZATION NAME(S) AND ADDRESS(ES) Saddleback Aerospace Corporation 7522 Slater, Suite 122 Huntington Beach CA 92647			8. PERFORMING ORGANIZATION REPORT NUMBER N/A	
9. SPONSORING/MONITORING AGENCY NAME(S) AND ADDRESS(ES) Defense Advanced Research Projects Agency Air Force Research Laboratory/IFTC 3701 North Fairfax Drive 26 Electronic Pky Arlington VA 22203-1714 Rome NY 13441-4514			10. SPONSORING/MONITORING AGENCY REPORT NUMBER AFRL-IF-RS-TR-2001-160	
11. SUPPLEMENTARY NOTES Air Force Research Laboratory Project Engineer: George O. Ramseyer/IFTC/(315) 330-3492				
12a. DISTRIBUTION AVAILABILITY STATEMENT APPROVED FOR PUBLIC RELEASE; DISTRIBUTION UNLIMITED			12b. DISTRIBUTION CODE	
13. ABSTRACT (Maximum 200 words) <p>This effort addressed fundamental issues in the characterization of the flow and heat transfer behavior of micro-systems, while at the same time providing an experimental database to reduce the need for scaling (typically 2 - 3 orders of magnitude) from available macroscopic correlations. The study began with the establishment of sample fabrication and testing techniques, and then progressed to actual thermal and flow measurements on the samples. During the program the following measurements were made:</p> <ul style="list-style-type: none"> • Friction factors (f) and transition Reynolds numbers ($Re_{transition}$) for 24 straight channels of varying surface roughness, using water, air, and FC-72 • Minor loss coefficients (K_{minor}) for 4 channels with Wyes, 4 channels with T's, and 32 channels with bends of varying aspect ratios and sharpnesses, using water, air, and FC-72 • Nusselt numbers (Nu) for 4 channel sizes using water and air <p>Notably, the experimental results showed that the transition Reynolds number and friction factors for smooth ducts gave no indication of any unusual effects at micro-scales, but that increasing the wall roughness tended to increase the friction factor and reduce the transition Reynolds number.</p>				
14. SUBJECT TERMS Micro-Electro Mechanical Systems (MEMS), Microchannels, Micro-Flows, Transition, Laminar Friction Factor, Roughness, Bends, T's, Wye's			15. NUMBER OF PAGES 146	
			16. PRICE CODE	
17. SECURITY CLASSIFICATION OF REPORT UNCLASSIFIED	18. SECURITY CLASSIFICATION OF THIS PAGE UNCLASSIFIED	19. SECURITY CLASSIFICATION OF ABSTRACT UNCLASSIFIED	20. LIMITATION OF ABSTRACT UL	

Table of Contents

SECTION	PAGE #
Table of Contents	i
List of Figures	iii
List of Tables	vii
Foreword	viii
Acknowledgements	viii
SUMMARY	1
1.0 INTRODUCTION	1
1.1 Program Overview	1
1.2 Survey of the Literature	3
1.2.1 Flow in Rectangular Microchannel Ducts	3
1.2.2 Heat Transfer in Microchannel Ducts	6
1.2.3 Other Micro-Flow Studies	8
2.0 STRAIGHT MICROCHANNEL FLOW STUDIES	9
2.1 Experimental Approach	9
2.1.1 Sample Fabrication	15
2.1.2 Microchannel Test Assembly	29
2.2 Results of Experiments	35
2.2.1 Laminar Friction Factor Coefficient Results	35
2.2.2 Transition Measurements	38
2.2.3 Roughness Measurements	40
3.0 STRAIGHT MICROCHANNEL HEAT TRANSFER STUDIES	45
3.1 Overview of the Experiment	45
3.2 μ Heat Exchange Test Samples	47
3.3 Description of the Experiment	52
3.4 Experimental Results	54
4.0 MINOR LOSS COEFFICIENT MEASUREMENTS	58
4.1 Minor Loss Coefficients of Bends	58

4.2	Minor Loss Coefficients of T's and Wye's	72
5.0	SUMMARY AND CONCLUSIONS	75
5.1	Program Summary and Conclusions	75
5.2	Recommendations	76
6.0	REFERENCES	77
Appendix 1	Straight Channel Specimen Descriptions and Test Data	79
Appendix 2	Bend Data	100
	List of Symbols	127
	List of Acronyms	128
	List of Definitions	129

List of Figures

<u>Figure No.</u>	<u>Title</u>	<u>Page</u>
1-1	Friction Factor vs. Re for Smooth Rectangular Micro-Ducts	4
2-1a	Predicted Flow Behavior for FC-72 in 1X4 Micron Channel at Room Temperature	11
2-1b	Predicted Developing Length Fraction for FC-72 in 1X4 Micron	11
2-2a	Predicted Flow Behavior for FC-72 in 1x4 Micron Channel at T=150°C	12
2-2b	Predicted Developing Length Fraction for FC-72 in 1x4-micron	12
2-3	Adiabatic Bulk Temperature Rise to Viscous Dissipation	13
2-4	Effect of Viscous Dissipation as Bulk Viscosity	13
2-5	Knudsen Number in Nitrogen Experiments	14
2-6	Plan View and Cross-sectional View of Nickel Plated Inconel Substrate	16
2-7	Typical Stainless Steel Substrates	17
2-8	Improved Microchannel Fabrication Approach	18
2-9a/b	Prototype Microchannel Specimen	21
2-9c	Close-up of Etched Silicon Wafer	21
2-9d	Close-up of 5µm x 50µm Channel	21
2-10	Profile Scan of 2µm Channel Plate	21
2-11	Ra of Two 20 µm Channels Upper Scan 130A, Lower Scan 70A	22
2-11a	Scan parallel to Channel, Average Roughness (absolute) =45A	23
2-11b	Scan Perpendicular to Channel, Average Roughness (absolute) = 50A	23
2-12	Roughness to Glass Slide Ra = 25A	24
2-13	Flow Experiment	29
2-14	Flow Performance Test Stand Schematic	30
2-15	Schematic of Flow Testing Experiment	30
2-16	Silicon Wafer Microchannel Fabrication and Test Design Update	32
2-17	Diagram Showing Channel Design and Jig Assembly for Holding the Assembly During Testing	32
2-18	Photos of 20µm Channel, 2µm Depth Showing Cleaved Ends	32
2-19	Silicon Microchannel Schematic	33
2-20	Photo of Cross-section of 2µm depth Silicon Microchannel	34
2-21	Sensitivity of Results to Errors in Channel Width Measurement	36
2-22	Typical Flow Data for 12.5µm	37
2-23	Typical Results of Data Reduction	38
2-24	Summary of Transitions	39
2-25	12.5 um 10X channels tested with water	41
2-26	Roughness Effect on Friction Factor for Nitrogen and Water	42
2-27	Raw Data Showing Transition (50µm, 4x Water)	42
2-28	Other Investigator's Measurements of the Dependence of Friction Factor in Roughness	43
2-29	Summary of Transition Data	44
3-1	Counterflow Provides Constant Heat Flux Boundary Condition	46
3-2	Parallel Flow Provides Constant Temperature Boundary Condition	46

3-3	Parallel Orientation μ Heat Exchange Schematic and Candidate Dimensions	49
3-4	Perpendicular Orientation μ Heat Exchange Schematic and Candidate Dimensions	49
3-5	Typical Foil Used in Fabrication of Perpendicular μ Heat Exchange Test Specimens	50
3-6	Typical Foil Used in Fabrication of Parallel μ Heat Exchange Test Specimens	50
3-7	Perpendicular μ Heat Exchange Specimens During Stacking	51
3-8	Perpendicular μ Heat Exchange Specimen After Diffusion Bonding, Machining and Mounting of Inlet and Outlet Tubes	51
3-9	Parallel μ Heat Exchange Specimen After Diffusion Bonding and Machining	52
3-10	Oblique View of μ Heat Exchange Test	53
3-11	Top View of μ Heat Exchange Test	53
3-12	Typical Raw Temperature Data for Water	55
3-13	Energy Balance and Effectiveness for Water	55
3-14	Raw Temperature Data for Air	56
3-15	Energy Balance and Measured Effectiveness for Air	56
3-16	Results of Counterflow μ Heat Exchange Experiments	57
3-17	Results of Parallel Flow μ Heat Exchange Experiments	57
4-1	45° Bend Data for 25 μ m and 128 μ m Channel Water	60
4-2	90° Bend Data for 25 μ m and 128 μ m Channel Water	60
4-3	45° Bend Data 25 μ m and 128 μ m Channel Comparison of FC-72 and Water Data	61
4-4	90° Bend Data 25 μ m and 128 μ m Channel Comparison of FC-72 and Water Data	61
4-5	45° Bend Data for 23 μ m x 178 μ m Channel Water	62
4-6	90° Bend Data for 23 μ m x 178 μ m Channel Water	62
4-7	45° Bend Data for 23 μ m x 172 μ m Channels Water versus FC-72	63
4-8	90° Bend Data for 23 μ m x 172 μ m Channels Water versus FC-72	63
4-9	45° Bend Data for 27 μ m x 185 μ m Channel Water	64
4-10	90° Bend Data for 27 μ m x 185 μ m Channel Water	64
4-11	45° Bend Data for 26 μ m x 185 μ m Channel Water	65
4-12	90° Bend Data for 26 μ m x 185 μ m Channel Water	65
4-13	45° Bend Data for 53 μ m x 243 μ m Channel Comparison of FC-72 and Water	66
4-14	90° Bend Data for 53 μ m x 243 μ m Channel Comparison of FC-72 and Water	66
4-15	45° Bend Data for 55 μ m x 344 μ m Channel Water	67
4-16	90° Bend Data for 55 μ m x 344 μ m Channel Water	67
4-17	45° Bend Data for 55 μ m x 356 μ m Channels Comparison of FC-72 and Water	68
4-18	90° Bend Data for 55 μ m x 356 μ m Channels Comparison of FC-72 and Water	68
4-19	45° Bends: Bend Sharpness Dependency	69
4-20	90° Bends: Bend Sharpness Dependency	69

4-21	Sensitivity to Bend Angle for 25 μm Channels	70
4-22	Sensitivity to Bend Angle for 50 μm Channels	70
4-23	45° Bends: Duct Aspect Ratio Dependence	71
4-24	90° Bends: Duct Aspect Ratio Dependence	71
4-25	Minor Loss Coefficients of 25 μm Wyes	73
4-26	Minor Loss Coefficients of 25 μm Tees	73
4-27	Minor Loss Coefficients of 50 μm Wyes	74
4-28	Minor Loss Coefficients of 50 μm Tees	74
A-1	Profilometer Traces of Bottom and Top Plates: Smooth 4X Channels	80
A-2	Profilometer Traces of Bottom and Top Plates: 2% Roughened 4X Channels	80
A-3	Profilometer Traces of Bottom and Top Plates: 10% Roughened 4X Channels	80
A-4	Profilometer Traces of Bottom and Top Plates: Smooth 10X Channels	81
A-5	Profilometer Traces of Bottom and Top Plates: 2% Roughened 10X Channels	81
A-6	Profilometer Traces of Bottom and Top Plates: 10% Roughened 10X Channels	81
A-7	Straight Channel: 13 μm x 95 μm and 13 μm x 178 μm Water	82
A-8	Straight Channel: 13 μm x 95 μm and 13 μm x 178 μm FC-72	82
A-9	Straight Channel: 13 μm x 95 μm and 13 μm x 178 μm Nitrogen	83
A-10	Sample A. Top and Bottom Steel Plates w/Roughened Areas	84
A-11	Photomicrograph of Sacrificial Channel Cross-section (200X)	84
A-12	Profilometer Traces of Bottom and Top Plates: Smooth 4X Channels	85
A-13	Profilometer Traces of Bottom and Top Plates: 2% Roughened 4X Channels	85
A-14	Profilometer Traces of Bottom and Top Plates: 10% Roughened 4X Channels	85
A-15	Straight Channel: 23 μm x 148 μm Water	86
A-16	Straight Channel: 23 μm x 148 μm FC-72	86
A-17	Straight Channel: 23 μm x 148 μm Nitrogen	87
A-18	Profilometer Traces of Bottom and Top Plates: Smooth 10X Channels	88
A-19	Profilometer Traces of Bottom and Top Plates: 2% Roughened 10X Channels	88
A-20	Profilometer Traces of Bottom and Top Plates: 10% Roughened 10X Channels	88
A-21	Straight Channel: 23 μm x 275 μm Water	89
A-22	Straight Channel: 23 μm x 275 μm FC-72	89
A-23	Straight Channel: 23 μm x 275 μm Air	90
A-24	Sample G. Top and Bottom Steel Plates w/Roughened Areas	91
A-25	Photomicrograph of Sacrificial Channel Cross-section (200X)	91
A-26	Profilometer Traces of Bottom and Top Plates: Smooth 4X Channels	92
A-27	Profilometer Traces of Bottom and Top Plates: 2% Roughened 4X Channels	92
A-28	Profilometer Traces of Bottom and Top Plates: 10% Roughened 4X Channels	93
A-29	Straight Channel: 66 μm x 243 μm Water	94
A-30	Straight Channel: 66 μm x 243 μm FC-72	94
A-31	Straight Channel: 66 μm x 243 μm Nitrogen	95

A-32	Cross-Section of Sacrificial Channel (200X)	96
A-33	Profilometer Traces of Bottom and Top Plates: Smooth 10X Channels	97
A-34	Profilometer Traces of Bottom and Top Plates: 1% Roughened 10X Channels	97
A-35	Profilometer Traces of Bottom and Top Plates: 10% Roughened 10X Channels	97
A-36	Straight Channel: 56 μm x 600 μm Water	98
A-37	Straight Channel: 56 μm x 600 μm FC-72	98
A-38	Straight Channel: 66 μm x 600 μm Air	99
A-39	45° Bends: 23 μm x 128 μm Water	102
A-40	90° Bends: 23 μm x 128 μm Water	102
A-41	45° Bends: 23 μm x 149 μm Water	104
A-42	90° Bends: 23 μm x 149 μm Water	104
A-43	45° Bends: 23 μm x 149 μm FC-72	105
A-44	90° Bends: 23 μm x 149 μm FC-72	105
A-45	45° Bends: 23 μm x 149 μm Nitrogen	106
A-46	90° Bends: 23 μm x 149 μm Nitrogen	106
A-47	45° Bends: 23 μm x 172 μm Water	108
A-48	90° Bends: 23 μm x 172 μm Water	108
A-49	45° Bends: 23 μm x 172 μm FC-72	109
A-50	90° Bends: 23 μm x 172 μm FC-72	109
A-51	45° Bends: 23 μm x 172 μm Nitrogen	110
A-52	90° Bends: 23 μm x 172 μm Nitrogen	110
A-53	45° Bends: 23 μm x 185 μm Water	112
A-54	90° Bends: 23 μm x 185 μm Water	112
A-55	45° Bends: 23 μm x 226 μm Water	114
A-56	90° Bends: 23 μm x 226 μm Water	114
A-57	45° Bends: 53 μm x 235 μm Water	116
A-58	90° Bends: 53 μm x 235 μm Water	116
A-59	45° Bends: 53 μm x 235 μm FC-72	117
A-60	90° Bends: 53 μm x 235 μm FC-72	117
A-61	45° Bends: 53 μm x 235 μm Nitrogen	118
A-62	90° Bends: 53 μm x 235 μm Nitrogen	118
A-63	45° Bends: 53 μm x 241 μm Water	120
A-64	90° Bends: 53 μm x 241 μm Water	120
A-65	45° Bends: 53 μm x 344 μm Water	122
A-66	90° Bends: 53 μm x 344 μm Water	122
A-67	45° Bends: 53 μm x 356 μm Water	124
A-68	90° Bends: 53 μm x 356 μm Water	124
A-69	45° Bends: 53 μm x 356 μm FC-72	125
A-70	90° Bends: 53 μm x 356 μm FC-72	125
A-71	45° Bends: 53 μm x 356 μm Nitrogen	126
A-72	90° Bends: 53 μm x 356 μm Nitrogen	126

List of Tables

<u>Table No</u>	<u>Title</u>	<u>Page</u>
1-1	Microchannel Cooler Heat Transfer Results	7
2-1	Surface Profiles Required to Satisfy Desired Roughness Factors and Channel Depth	15
2-2	Target Dimensions and Roughness of Silicon Microchannels	19
2-3	Silicon Etch With Anodic Bonding to Glass, KOH Method Process Outline	25
2-4	Silicon Etch With Anodic Bonding to Glass, Isotropic Etch Method Process Outline	26
2-5	Metal Build-up With Anodic Bonding to Glass Process Outline	27
2-6	Sacrificial Etchings Process Outline	28
2-7	Results of Smooth Channel Friction Factor Measurements	37
A-1	Guide to Straight Channel Specimen Description and Test Data	79
A-2	Sample P.	80
A-3	Sample A.	84
A-4	Sample G.	91
A-5	Sample D.	96
A-6	Summary of Bend Channel Specimens and Tests	100
A-7	Sample K.	101
A-8	Sample L.	103
A-9	Sample M.	107
A-10	Sample J.	111
A-11	Sample B.	113
A-12	Sample N.	115
A-13	Sample E.	119
A-14	Sample F.	121
A-15	Sample O.	123

Foreword

Saddleback Aerospace and the University of California, Irvine collaborated in this study to assist micro-fluidic system designers by resolving some basic questions concerning flowfields at the micro-scale, and by establishing useful flow and heat transfer correlations for typical flow designs. This program was designed as a survey study, where a set of simple experiments was conducted on a large number of common flow and heat transfer geometries. The test results were then disseminated to the research community via conferences and a web site at <http://www.microflowstudies.org>.

ACKNOWLEDGEMENTS

This project was funded by DARPA/MTO and monitored by Air Force Research Laboratory/IFTC as part of the DARPA Composite CAD program. The authors would like to express their thanks to DARPA program managers Dr. Heather Dussault and Dr. Anantha Krishnan for their support in this effort. The authors would also like to thank Dr. George Ramseyer of AFRL/IFTC for his monitoring of the contract and his help in coordinating with DARPA and other participants in the COMPOSITE CAD program.

Several people at Saddleback provided substantial assistance with the project. Mr. Jay Fryer and Mr. Steve Coley prepared many of the experimental setups and performed preliminary testing. Ms. Elizabeth Campbell performed many of the flow performance tests and assisted with the preparation of the final report. Ms. Denise Dunphy etched and stacked the foils for the heat transfer test specimens.

SUMMARY

The ongoing DARPA-sponsored MicroFlume and BioFlips programs are demonstrating that micro-electromechanical systems (MEMS) incorporating micro-fluidic designs can offer unique and important capabilities, particularly in the areas of miniaturized assays, detectors, and chemical processing. As these systems become more capable, the challenges in the design of the fluidic components become more severe due both to increasing complexity in the flows, and more stringent requirements for understanding and manipulating the flows.

Lab-on-chip researchers are currently investigating micro-flow systems with advanced mixing schemes, electrokinetic effects, and rigid and deformable particles, all of which offer formidable challenges in understanding, characterizing, and predicting the flows. Their design efforts have been supported through the simultaneous development of multiphysics computational simulation tools. But at the same time, a significant controversy exists in the experimental literature concerning the flow and heat transfer behavior of straight, smooth microchannels (Papautsky et al., (1999a, 1999b); Mala et al., (1999a, 1997); Peng et al., (1995a, 1995b)).

Thus there is a gap between the activities of MEMS designers and the ability of many experimentalists to reliably verify flow behavior at micro-scales in even the simplest geometries. This leads to questions concerning the foundations of MEMS fluid system designs: Are the discrepancies due to experimental error, dimensional uncertainties, or the appearance of an unexplained micro-scale phenomenon? All three possibilities have implications for the design of micro-fluidic systems. A second question would be: Given the difficulties experimentalists have had in reconciling classical predictions with experimental results for single channels, what are the prospects that mass-manufactured MEMS systems will perform reliably, consistently, and accurately?

The work described in this report represented an attempt to address some of these concerns, while at the same time providing an experimental database to reduce the need for scaling (typically 2 - 3 orders of magnitude) from available macroscopic correlations (such as those available in Fried & Idelchik (1989) and Kays & London (1984)). The motivation for pursuing the proposed study lies in the fact that while there are not expected to be any unusual physics in effect at this scale, the geometries and flow regimes of emerging micro-fluidic systems are sufficiently removed from their macroscale counterparts that scaling of existing correlations is risky. In addition, the complexity of many of the flow systems makes computational approaches prohibitively expensive, particularly when multidisciplinary design approaches are required.

1.0 INTRODUCTION

1.1 Program Overview

Saddleback Aerospace and the University of California, Irvine collaborated in this DARPA-sponsored study to assist micro-fluidic system designers by resolving some basic questions concerning flow fields at the micro-scale, and by establishing useful flow and heat transfer correlations for typical flow designs. This program was designed as a survey study, where a set of simple experiments was conducted on a large number of common flow and heat transfer geometries. The test results were then disseminated to the research community via conferences and a web site at <http://www.microflowstudies.org>.

The overall objective of the program was to improve the understanding of thermofluid physics for both laminar and transitional flow fields in a variety of complicated micro-geometries. Specific objectives of the program included:

Friction Factors. Measurement of friction factors for a variety of geometries.

Nusselt Numbers. Measurement of heat transfer coefficients for a variety of geometries.

Transition Behavior. Experimental characterization of the transition behavior of smooth and roughened rectangular channels.

Roughness Effects. Experimental examination of the influence of roughness on laminar friction factors and heat transfer coefficients, and on transition behavior.

Composite CAD Program Support. Derivation of flow and heat transfer correlations for a variety of geometries.

The focus of this effort was on the microflume size range from 50 μm down to 1 μm . It is believed that this covers the range of likely near-term MEMS-class applications. This scale selection places most simple liquids and gases solidly within the continuum flow regime, where classical treatments of flow and heat transfer behavior can normally be expected to apply. Non-continuum behavior such as slip flow or transitional regime effects was not directly addressed.

The philosophy of the program was that based on prior testing experiences and the literature, the theory for smooth straight microchannels was generally more reliable than experimental results. Thus, the quality of the experimental procedure was graded based upon how closely the results for smooth, straight microchannels matched theoretical expectations. Having established a measure of confidence in the experimental results, the program then proceeded with tests of more complex flow cases, adding roughness, bends, Wytes and T's to develop a full database for simple rectangular channel configurations.

A second major tenet of the program was that each channel should be tested with more than one fluid, so that any differences in flow or heat transfer behavior due to the fluid's characteristics or its interaction with the channel walls could be identified. Water and nitrogen (representing air) were used in both the flow and heat transfer experiments, since they are the most commonly encountered fluids in macro and micro systems. FC72 was selected as the third fluid for the flow experiments, since it is a non-polar fluid, and since its lower kinematic viscosity enabled experiments at higher Reynolds numbers. Polyalphaolefin was chosen as the third fluid for the heat transfer experiments due to its large Prandtl number (twenty times larger than water).

A significant portion of the program effort was devoted to testing at Reynolds numbers much higher than are commonly experienced in micro-fluid systems. This was done for several reasons. First, previous reports suggested that transition could occur at Reynolds numbers as low as 300 (Peng, 1994a). By extending the testing range to Reynolds numbers of 1000 – 2000, the appearance of transition could be more clearly identified. Second, the need to improve mixing has led some investigators to evaluate turbulent flows. Finally, while MEMS fluidic systems,

which use on-board pumps, are typically limited to very low Reynolds numbers, systems interfacing with off-board macro pumps can easily operate at much higher Reynolds numbers.

Program Accomplishments. The study began with the establishment of sample fabrication and testing techniques, and then progressed to actual thermal and flow measurements on the samples. The early portion of the program resulted in the development of methods for fabricating robust silicon and superalloy microchannel specimens, and in a method for mating a high-pressure flow system to a silicon sample.

The technical period of performance on the contract lasted approximately 13 months. During this period the program measured:

- Friction factors (f) and transition Reynolds numbers ($Re_{TRANSITION}$) for 24 straight channels of varying surface roughness, using water, air, and FC-72
- Minor loss coefficients (K_{MINOR}) for 32 channels with bends of varying aspect ratios and sharpnesses, using water, air, and FC-72
- Minor loss coefficients for 4 channels with Wyes and 4 channels with T's
- Nusselt numbers (Nu) for 4 channel sizes using water and air

With the exception of the roughness data, the measurements were reasonably consistent with scaling from macroscopic flow geometries. Notably, the experimental results showed that the transition Reynolds number and friction factors for smooth ducts gave no indication of any unusual effects at micro-scales, but that increasing the wall roughness tended to increase the friction factor and reduce the transition Reynolds number. The latter results are surprising, and suggest the need for further study of roughened wall contributions to micro-flow behavior.

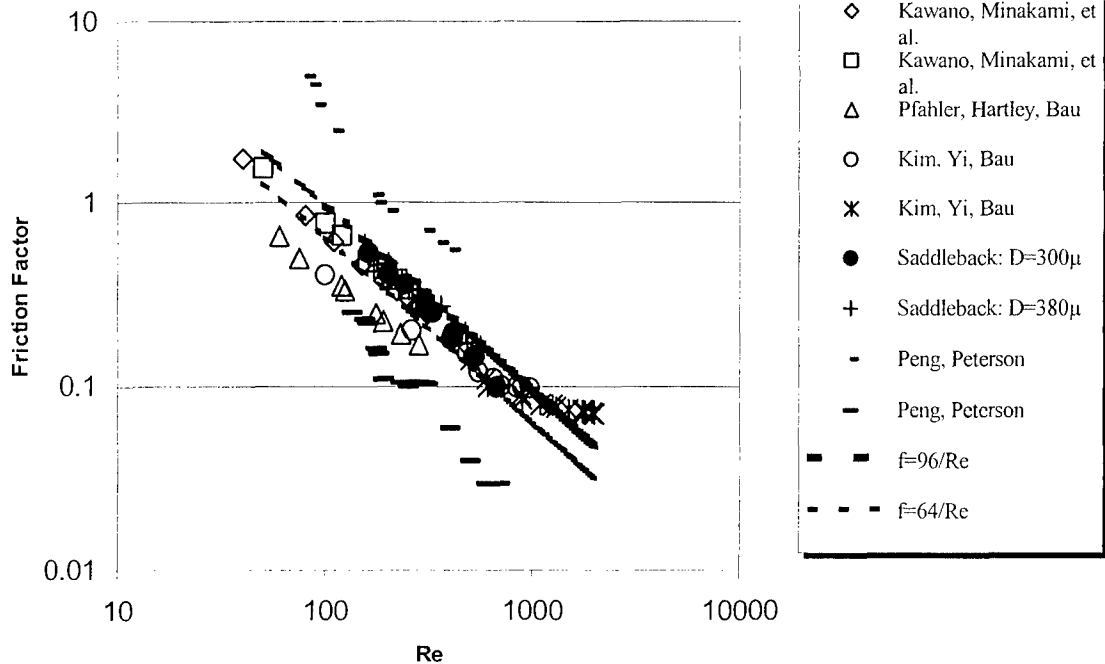
1.2 Survey of the Literature

This section provides background information on some of the microchannel flow and heat transfer data, and on interpretations of that data. The sub-sections discuss the appearance of anomalous results for straight channel flows in the literature, and provide a literature survey for flows other than simple straight channels. This section forms the basis for the design of the baseline program as well as many aspects of the program options being considered.

1.2.1 Flow in Rectangular Microchannel Ducts

A review of some of the available microchannel flow performance data is briefly summarized here. Figure 1 provides a plot of the apparent friction factor versus Reynolds number measured in several programs. As the figure shows, results from different teams vary widely. While many researchers (e.g., Tuckerman (1984), Wu and Little (1983, 1984), Phillips (1988), Pfahler et al. (1990), Harley et al. (1995), Campbell et al. (1997), and Kim et al. (1998)) have had reasonable success in using classical fluid/heat transfer analyses to explain experimental data down to channel sizes of $25\text{ }\mu\text{m} \times 200\text{ }\mu\text{m}$, there are consistent reports in the literature of experiments or theoretical approaches that yield results which are inconsistent with macroscopic duct theory. In summary papers, for example, Ho and Tai (1998) and Duncan and Peterson (1994) discuss the evidence for novel effects in flows at reduced scales. Much of the discussion in both cases is

Figure 1-1. Friction Factor vs. Re for Smooth Rectangular Micro-Ducts



based on the data obtained by Pfahler et al. (1991) using silicone oil and isopropyl alcohol in rectangular and trapezoidal channels ranging from 0.48 μm to 38.7 μm (in the narrow dimension).

In the Pfahler et al. experiments, the averaged normalized friction factor for the smaller channels was observed to be much smaller than in the larger channels, and the two fluids exhibited markedly different trends with channel size. This was attributed to the polar vs. non-polar nature of isopropyl alcohol and silicone oil, respectively. It should be noted that the reproduction of Pfahler et al.'s data for isoproponal in Ho and Tai's (1998) paper is very different than in the original publication. The data has never been duplicated, and there are indications that the data may have been compromised by experimental problems (Dussault, 1998; Kim et al., 1998; Bau, 1998).

Recent experiments were conducted by Tsinghua University (Wang & Peng, 1994; and Peng et al., 1995a, 1995b), which generated two results of note: first, the laminar to turbulent transition number was in the range of 300 - 800, much lower than the range of 1800 - 2300 typically assumed for larger pipes, and second, the friction factor had a non-linear dependence on the Reynolds number in the laminar regime. The friction factor was given as:

$$f = \frac{C_f}{Re^{1.98}}$$

where the term C_f is an empirical constant which is a function of the microchannel geometry. The C_f term varies from 5200 to 32400 in the two cases presented in the reference, which is a

much larger variation than the factor of two variation ($56 < f_{lam} < 96$) that classical theory predicts (Shah & London, 1978).

Papautsky et al. (1999a) recently proposed that the laminar friction factor discrepancies between theory and experiment might be due to micropolar effects. By adding terms for the gyration and 2nd order viscosity to the Navier-Stokes equation, and by employing a conservation of microinertia equation, 2D finite difference models yielded friction factors that were slightly higher (<10%) than those predicted without microinertia effects. This agreed well with cases in the literature where the friction factor was ~ 10% higher than expected, but did not address the larger amount of data in the literature that was either much higher or slightly lower than expected, including later data taken by Papautsky et al. (1999b) showing a 20% increase in friction factor. At this time it is difficult to determine whether microrotation is an important effect in microchannel flows.

The data presented by Papautsky et al. (1999b) were based on measurements of water flow through five arrays of nickel microchannels. The channels were roughly 25 μm wide, with aspect ratios varying from about 6 to about 30. The flow measurements, conducted over a Reynolds number range of 0.002 to 3, showed friction factors approximately 20% higher than predicted (as mentioned above), with a downward trend towards the upper end of the Reynolds number range.

The persistent problems in obtaining consistent results underscored the need for the development of a larger, consistently derived database - even for the simplest microchannel geometries. This provided the motivation for the experimental efforts described in this report.

1.2.1.1 Roughness Effects

Historically, roughness effects have been found to be negligible in laminar duct flows, due to the near-zero fluid velocities near the wall. Wu and Little (1983, 1984) examined roughened ducts in glass and silicon, and noticed a substantial increase in laminar friction factor, although an inverse linear dependence with Reynolds number was maintained. Floryan (1997) analytically simulated distributed wall roughness effects using a wall suction model. In this linear analysis, wall suction of a critical amplitude was shown to introduce instabilities which led to the generation of streamwise vortices. These vortices carry low momentum fluid away from the wall and distort the velocity profiles of the flow. The instabilities appeared at Reynolds numbers lower than the linear critical Reynolds number

Pfund, et al. (1998), compared a smooth 508 μm x 10000 μm polyimide channel to an identical brass channel with 0.1% roughness. They found that the laminar friction factor increased by 20 - 30%, even at this low roughness level. Observations of the flow on a microscopic level showed micro-convection cells within the troughs and pits of the roughness.

Mala et al. (1999) performed a series of experiments on stainless steel and fused silica tubes with diameters ranging from 50 μm to 250 μm . The tubes all had mean surface roughnesses of 1.75 μm . The equivalent "sand grain diameter" would then be 3.5 μm . The measured laminar friction factors were all higher than predicted using standard duct theory (Shah and London, 1978). There is some discrepancy in the reporting of the transition Reynolds number: while Mala et al.

report transition at $300 < Re < 900$, the data presented in the paper shows linear behavior up to Reynolds numbers of at least 900.

Mala et al. (1999) then used the approach developed by Merkle et al. (1974) to analytically assess the effects of roughness in laminar flows. The model is based on the assumption that the eddies induced in laminar flow by roughness elements behave similarly to eddies in turbulent flows. A roughness viscosity was obtained that is conceptually equivalent to the eddy viscosity, and this viscosity was then incorporated into a finite difference model to solve for the velocity profiles in the tubes. The results agreed with closely with the data.

1.2.1.2 Electrokinetic Effects

Electrophoretic and electroosmotic flows have been used in capillary systems for many years, with no apparent microchannel-specific effects. As the channel size begins to approach the double layer size, however, some interesting effects might appear. The University of Alberta has published a series of papers concerning increases in apparent viscosity in pressure-driven microchannels due to back-streaming flow effects (Yang et al. [1998], Mala et al. [1997], Yang & Lee [1997], and Mala et al. [1996]. This effect could be presumed to exist in silicon or glass channels using water as a fluid, and would perhaps aid in explaining some of the inconsistencies in experimental results.

In the area of electrokinetic flows, teams led by Microcosm, CFD Research, and the University of Illinois have conducted experimental programs to verify numerical models of electroosmotic and electrophoretic effects. These efforts have all met with success, although only a few flow geometries have been considered to date (for example, Molho et al. [1998] and Giridharan & Krishnan [1998]).

In general, electrokinetic flows involving simple fluids appear to be reasonably well understood. In flows with particles or bioconstituents, however, the interactions among the wall, electric field, fluid, and particles can be very complex. These situations are likely to spawn a number of experimental and numerical analysis efforts over the next decade.

1.2.2 Heat Transfer in Microchannel Ducts

Most of the available data concerning heat transfer in micro-systems is derived from studies of the performance of microchannel coolers. Table 1-1 gives a summary of microchannel cooler data obtained from the literature; some comparable cooler designs which do not use microchannels are also shown. In most cases the data obtained agreed well with existing correlations such as those in Shah and London (1978). Generally these deviations could be explained by: 1) thermal spreading effects which were not accounted for by the authors, and/or 2) errors in measuring the power absorbed by the cooler.

Wang and Peng (1994) and Peng et al., (1995b) measured heat transfer coefficients of small arrays of microchannels machined in stainless steel and capped with glass plates. They obtained a laminar Nusselt number (Nu) of:

$$Nu = 0.1165 \left(\frac{D_h}{W_c} \right)^{0.81} \left(\frac{H}{W} \right)^{-0.79} Re^{0.62} Pr^{1/3}$$

Where D_h is the hydraulic diameter, W_c is the channel-to-channel spacing, H is the channel height, W is the channel width, and Re and Pr are the Reynolds number and Prandtl number, respectively. This correlation was found to match the data for 12 channels within +/-30% over a range of Reynolds numbers from 90 to 900.

Table 1-1. Microchannel Cooler Heat Transfer Results

Agency	Mat'l	Channel Width (μm)	Channel Height (μm)	Channel Length (μm)	Flow Rate/ Channel	DP (psi)	Heat Flux (W/cm^2)	Thermal Resistance ($^{\circ}\text{C}\text{-cm}^2/\text{W}$)	Ratio of Cooled to Heated Area
LLNL	Si	50	302	14000	0.043 g/s	31	790	0.090	2.8
	Si	55 (Pin Fin)	400	14000	0.085 g/s	53	1309	0.083	3.0
	Si	25	150	1400	0.014 g/s	50	2700	0.014	4.2
	Si	25	200	1850	0.0175 g/s	55	1860	0.014	6.3
	Si	50	200	4000	0.155 g/s	50	111	0.094	1.0
MIT/LL	InP	160	160	9525	0.018 g/s	25	68	0.100	9.9
	InP	220	165	9700	0.033 g/s	50	114	0.072	9.3
	Si	100	400	10000	0.5 g/s	70	500	0.040	20.0
Cornell	Si	40	400	3200	0.027 g/s	50	100	0.05	39.4
Saddleback	Cu	25	225	600	0.012 g/s	45	490	0.083	1.0
Perkin Elmer	Si	36	420	10000	0.013 g/s	45	600	0.009	31.1
N. C. State	Cu	5870	1000	100000	31.5 g/s	16	42	0.35	3.2
	Cu	5870	100	100000	3.15 g/s	41	42	0.40	3.2
NTT	Al_2O_3	800	400	86000	0.46 g/s	?	24	8.0	4.0
McDonnell Douglas	Cu	?	?	10000	5.6 $\text{g}/\text{s}/\text{cm}^2$	~ 80	125	0.125	1.0
	BeO	?	?	10000	5.6 $\text{g}/\text{s}/\text{cm}^2$	20	125	0.26	1.0
Sunstrand (Jet Imp.)	Cu	100 μm Foils w/200 μm Jet Orifices			5.6 $\text{g}/\text{s}/\text{cm}^2$	~ 80	125	0.29	1.0
	Cu	100 μm Foils w/Larger Jet Orifices			5.6 $\text{g}/\text{s}/\text{cm}^2$	35	125	0.19	1.0

1.2.3 Other Micro-Flow Studies

1.2.3.1 Finned Microchannels

There is little data on low Reynolds number flows in finned channels, and little data on micro-finned structures. The backbone of the experimental database for flow through finned channels results from the work of Kays and London (1984), which generally measured flows down to a Reynolds number of about 600. These results were used by Weiting (1975) to create a commonly-used set of scaling laws for heat exchangers, but these laws were developed for air only, and may not be applicable to higher Prandtl number or to lower Reynolds number flows (Hu, 1993). It is also not clear that they can be extended to the dimensional regime considered in this proposal.

Tuckerman (1984) measured three rectangular pin fin arrays, with effective channel widths of 60 - 100 μm and heights of 255 - 367 μm . Rather than using a correlation such as that generated by Kays and London (1984), Tuckerman treated the pin fin array as a parallel array of uninterrupted rectangular channels to generate the predicted values of C shown in the table. He achieved good agreement between the measured and predicted results despite this simplification. His conclusion was that there was that the use of fins had little effect on the flow or heat transfer of micro-heat sinks.

Campbell et al. (1997) performed a series of tests on micro-finned arrays, with fin spacings ranging down to 500 μm x 500 μm , and with elliptical fin sizes of 64 μm high x 50 μm wide and 150 μm long. In general classical finned array correlations tended to overpredict the pressure drop by 25 - 50%. Only six specimens were tested, and the peak Reynolds number was limited to about 300 due to pressure limitations of the test setup. Yin and Bau (1997) provided numerical solutions for arrays of square micro-pins in microchannel ducts. The results showed that for shallow channels ($\sim 100 \mu\text{m}$), the pin fin arrays offered a lower thermal resistance than rectangular ducts. The authors also point out that due to large variations in the heat transfer coefficient (h) along the fin surface, classical uniform- h fin analyses are not likely to be valid.

1.2.3.2 Bends

Bends, T's, Wyes, Expansions and Contractions are common features of macro- and micro- flow systems, and so the characterization of their flow behavior is important to MEMS-class fluid designs. Very little experimental data is available for these features in the literature. Campbell et al. (1998) examined 90° bends in channels with depths ranging from 32 μm to 65 μm . The minor loss coefficients were measured from $Re = 10$ to $Re =$ about 350. The minor loss coefficients were extremely high - ranging from the hundreds at low Re to about 10 at the higher Re .

Kim et al. (1999) examined the flow in four channels with minimum dimensions of 200 μm . The apparent Poiseuille number was generally consistent with the expectations for a straight channel. No attempt was made to derive a minor loss coefficient, or to isolate the influence of the bend. The study also compared 2D and 3D simulations of the corner flow, which gave very different results. The 3D numerical simulations of a square cross-section duct showed a parabolic dependence of the apparent Poiseuille number on Reynolds number.

2.0 Straight Microchannel Flow Studies

Straight channels provide canonical flow systems, which lend themselves to straightforward experimentation and analysis of results. Thus, the straight channel experiments could be used to provide insight into both the fundamental physics of microchannel flows and any experimental or sample preparation issues. The specific goals of the flow studies were to generate the data required to address the following questions:

- 1) Is the experiment providing reasonable results? It was assumed based on prior results that the friction factors predicted for large rectangular ducts would be scaleable to microchannels, allowing the experimental results to be directly compared to theoretical predictions.
- 2) Do experimental results vary with the fluid tested? Three fluids were used in the testing: nitrogen gas, water, and FC-72. FC-72 is a non-polar liquid fluorocarbon with a kinematic viscosity an order of magnitude lower than that of water. These three fluids offered a number of differences in terms of compressibility, molecular size and mean free path, viscosity, and electrokinetic susceptibility.
- 3) Does transition in microchannels occur at lower Reynolds numbers than is observed in conventional ducts? The publications of Peng et al. (1994a, 1994b, 1995) indicate that transition in microchannels might occur at Reynolds numbers as low as 300.
- 4) Does increased wall roughness in microchannels affect either the apparent laminar friction factor or the transition Reynolds number? Pfund et al. (1998) measured a significant increase in friction factor for a mildly roughened microchannel.

As mentioned in the introduction, it was decided to extend the range of testing to relatively high Reynolds numbers, with the goal of testing to at least $Re = 1200$ for every sample. This aggressive goal drove the selection of the low viscosity fluid (FC-72), and dictated much of the sample fabrication and the experiment design, as discussed in Section 2.1. High Reynolds number testing and fabrication approaches for both silicon and metal samples were developed, although only the metal samples were successfully tested in this program.

The sections below detail the development of the sample fabrication approach, the design of the experiments, the experimental procedure, and the results of the testing. The conclusions resulting from the experiments are presented in Sections 2.2 and 5.2.

2.1 Experimental Approach

This section describes the design, fabrication and evaluation of the test samples and of the test fixtures for the flow performance experiments. In the cases of both the larger and the smaller microchannels, the sample fabrication and experiment design was driven by the requirement to test at Reynolds numbers of at least 1200. A flow test sizing spreadsheet model was developed to calculate the flow rates and pressure drops for each fluid and each specimen. The model included

entrance and exit effects, using classical rectangular channel friction factor and minor loss coefficient correlations in all cases. The spreadsheet was used to determine supply pressure requirements, developing flow lengths and test times.

From the results it quickly became apparent that polyalphaolefin (PAO) would not be a suitable choice for a flow test fluid, due to its high viscosity. A survey of alternate liquids identified FC-72 as a promising choice. FC-72 has a viscosity about one half that of water, and about sixteen times lower than PAO. PAO was been retained as a test fluid for the heat transfer tests due to its high Prandtl number.

Figure 2-1a shows a plot of the required supply pressure vs. Reynolds number for FC72 in a 1 x 4 μm channel at several passage lengths (this is the most stressing test design case). The developing flow lengths are shown in Figure 2-1b. The original goal was to keep the developing lengths to less than 10% of the passage length, to reduce the influence of developing flow, and to avoid obscuring the appearance of transition. A second goal was to keep the supply pressure below 3000 psi, to avoid further complicating the test design and unduly stressing the test specimens.

As can be seen in the figure, the 1 x 4 μm channel is too small to allow access to Reynolds numbers much over 10. It was decided to examine the effect of increasing the flow test temperature to 150°C to reduce the viscosity. This resulted in the plots shown in Figure 2-2, which show that a 2200 psi supply pressure could achieve Reynolds numbers of nearly 1000 at the higher test temperature [in this case the downstream pressure must be > 200 psi to prevent vaporization of the FC-72].

Viscous Dissipation Effects. The heating of the fluids due to viscous dissipation effects was a potential source of concern, due to the high pressure drops are encountered in testing. In the data reduction the fluids are assumed to be isothermal due to the large heat transfer coefficients associated with microchannel passages: if the walls were adiabatic, this assumption would lead to large errors in interpretation of the data. The walls are not adiabatic since the heat transfer coefficients in the microchannels are very high, but in the interest of bounding the problem, the maximum possible temperature rise due to viscous dissipation was evaluated.

Assuming that the fluid is incompressible, transverse temperature gradients are negligible, and the wall is adiabatic, the maximum temperature rise due to viscous dissipation may be written as:

$$\Delta T = \frac{\Delta P}{\rho \cdot C_p}$$

Figure 2-3 shows the bulk temperature rise predicted for water and FC-72 as a function of the pressure drop along the channels. As shown, the temperature rise can be significant if the walls are adiabatic. For the channels tested in the program, the actual pressure drops measured in the experiments were rarely above 2000 psi. As shown in Figure 2-4, the Figure 2-3 temperature increases would result in roughly a 5% change in the viscosity of water and a 10% change in the viscosity of FC-72 at 2000 psi.

For air, the temperature change is a result of viscous dissipation and compressibility effects, and is a function of the inlet temperature and inlet and exit Mach numbers. The maximum

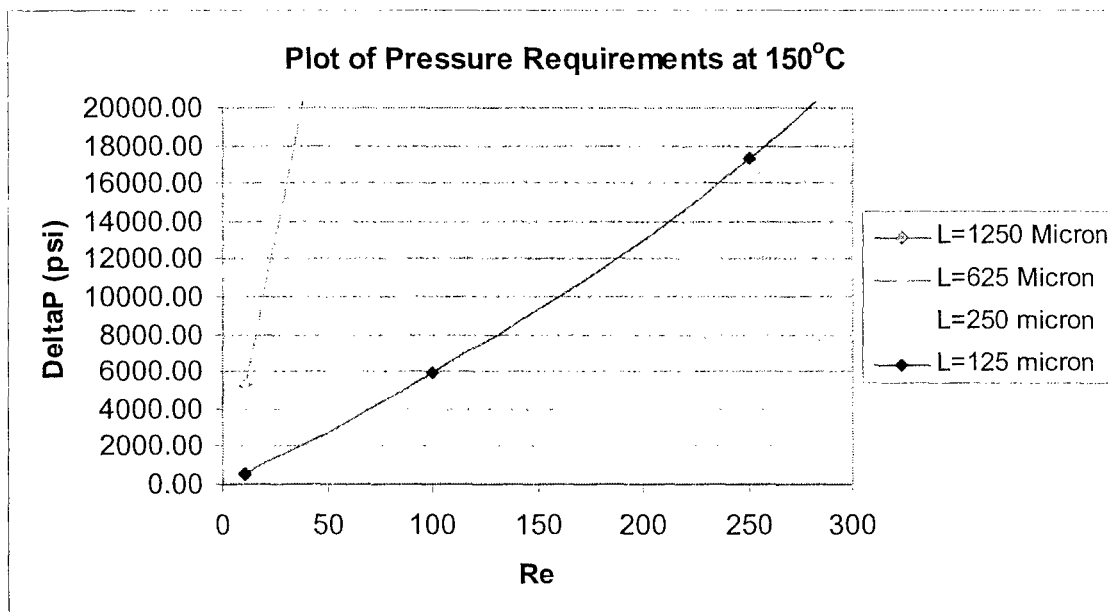


Figure 2-1a. Predicted flow behavior for FC-72 in 1 x 4-micron Channel at Room Temperature.

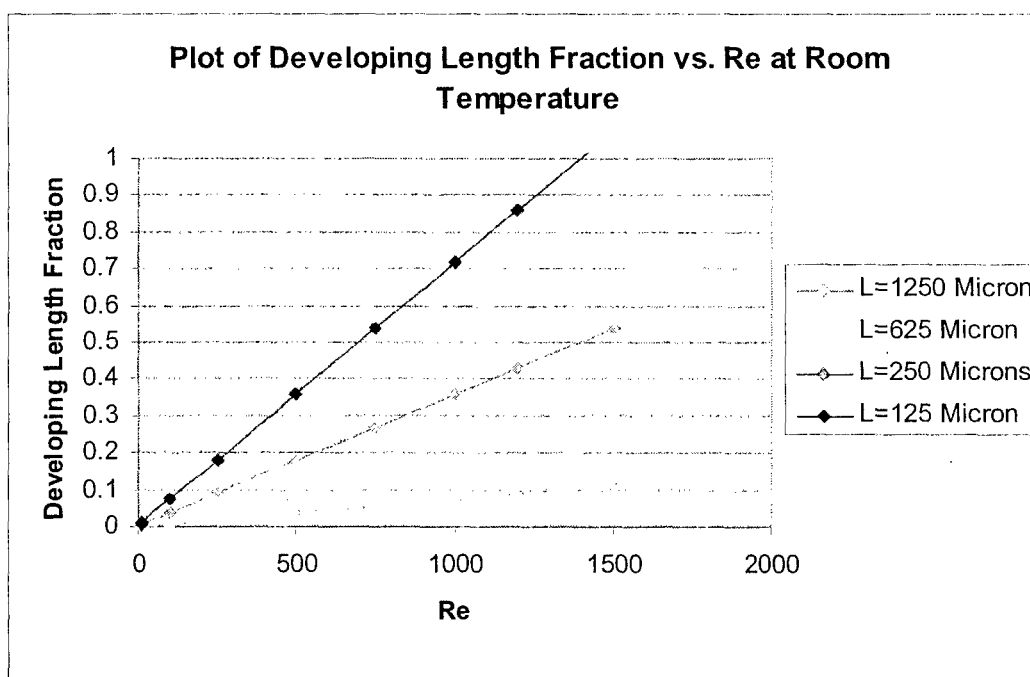


Figure 2-1b. Predicted Developing Length fraction for FC-72 in 1 x 4-micron Channel at Room Temperature.

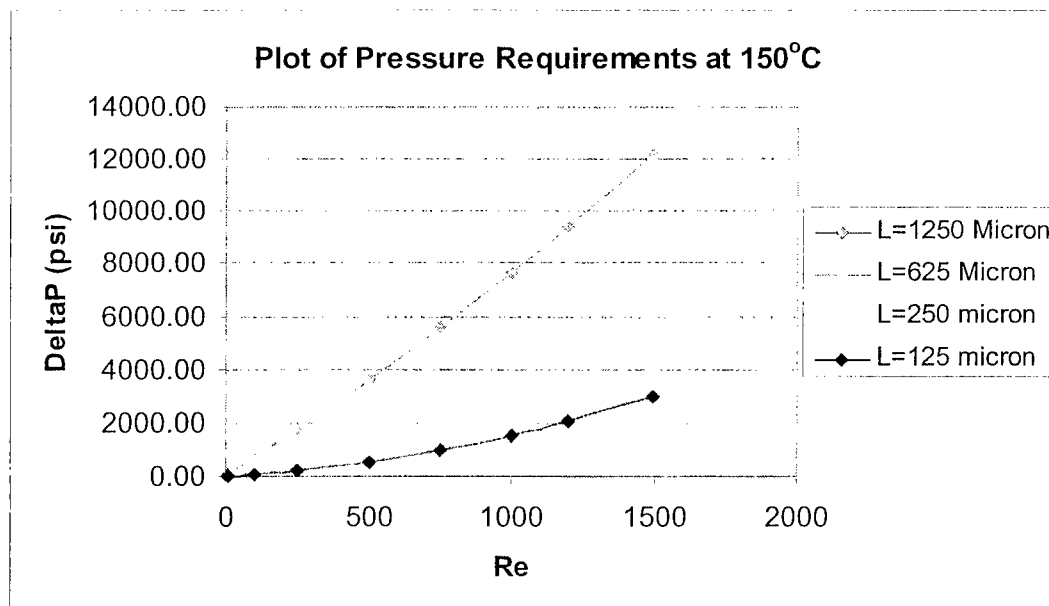


Figure 2-2a: Predicted flow behavior for FC-72 in 1 x 4-micron Channel at T=150°C.

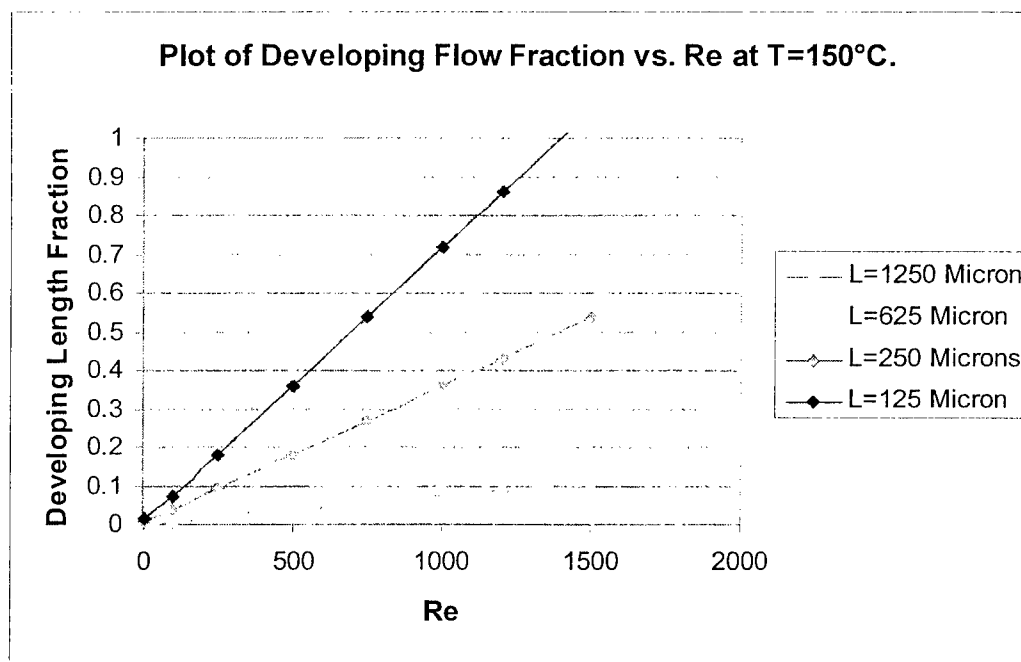


Figure 2-2b: Predicted Developing Length fraction for FC-72 in 1 x 4-micron Channel at T=150°C.

Figure 2-3. Adiabatic Bulk Temperature Rise Due to Viscous Dissipation

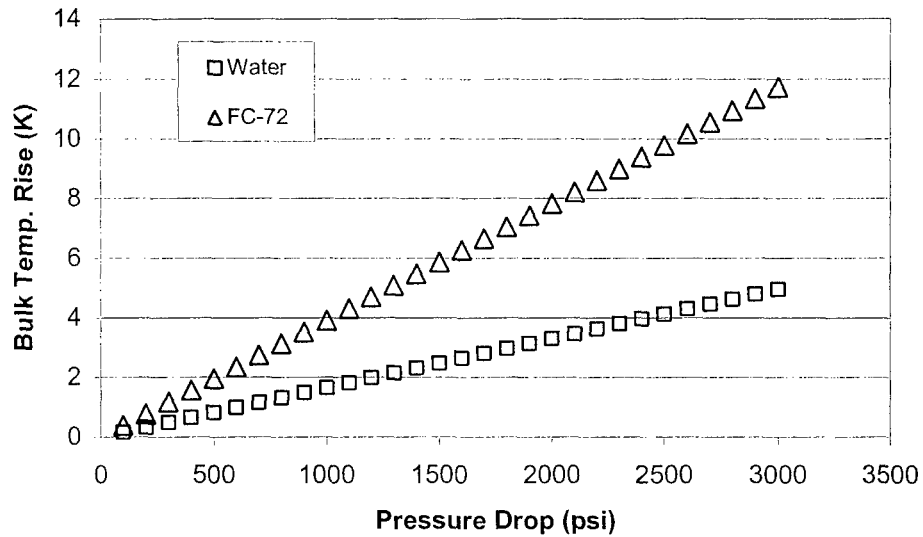


Figure 2-4. Effect of Viscous Dissipation on Bulk Viscosity

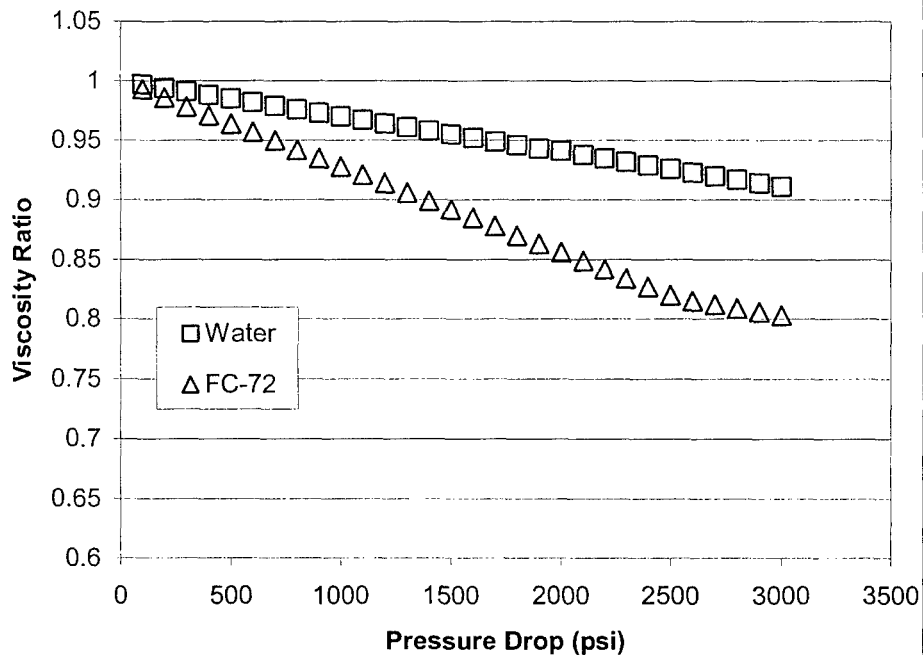
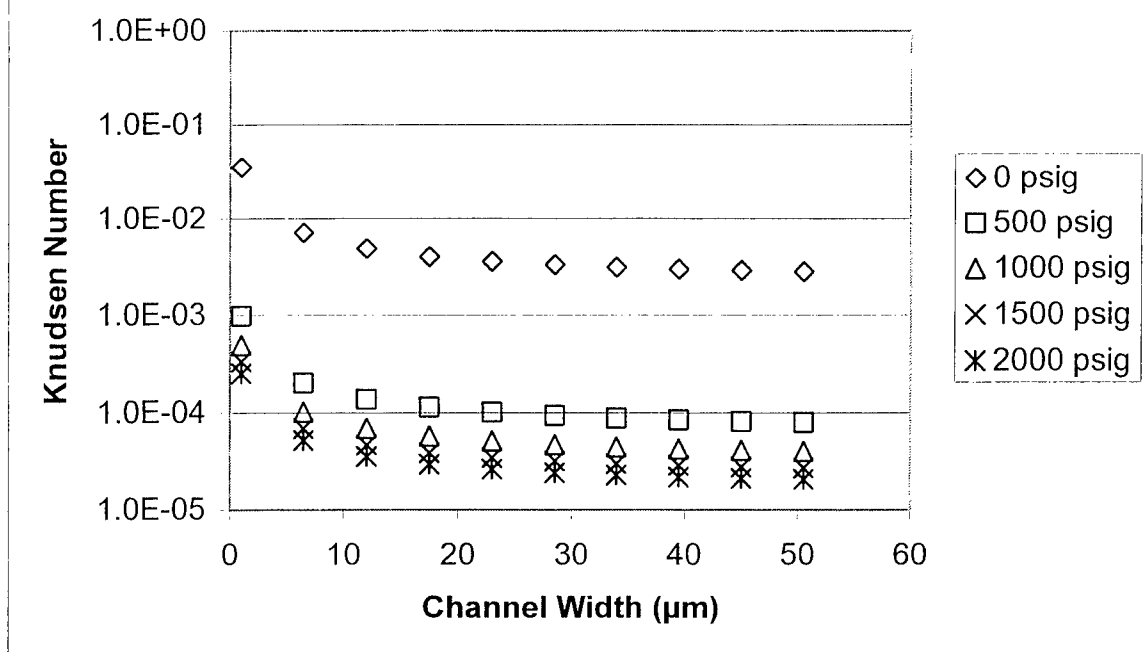


Figure 2-5. Knudsen Number in Nitrogen Experiments



temperature change would be for an inlet Mach number of 0, and an exit Mach number of 1. This would result in an 18% temperature drop, which is equivalent to a 10 – 15% decrease in the viscosity, depending upon the inlet pressure.

Continuum Regimes. Figure 2-5 shows the Knudsen number for nitrogen (taken as mean free path over channel width) as a function of channel width (the minimum channel dimension) at various pressures. Flows with Knudsen number less than 0.01 are generally considered to be operating in the continuum regime. As shown, the experiments conducted during this project (channel widths of 12.5 μm and higher) lie well within the continuum regime. Planned experiments using N₂ in the smallest microchannels (1 μm width) would have encroached on the transitional regime, but the actual experiments performed were at Knudsen numbers more than an order of magnitude higher. The Knudsen numbers for the liquids are orders of magnitude lower than those for nitrogen. Based on these results, non-continuum effects were not expected in the experiments.

2.1.1 Sample Fabrication

The test samples in the program were divided into two classes: "large" microchannels, with channel widths of 12.5 μm and above, and "small" microchannels, with channel widths of 10 μm and below. The larger microchannels were fabricated using metal processes in order to create very robust test specimens and to provide economy to the program. The small channels were fabricated using silicon processes to achieve greater dimensional control. The two approaches required the development of very different fabrication methods: each approach is described in the subsections below.

2.1.1.1 Fabrication of Large ($>10\mu\text{m}$) Microchannels

The goals of the metal microchannel fabrication method development included: 1) developing means of manufacturing microchannels capable of withstanding internal pressurization to 3000 psi with negligible deformation of the channels, 2) ensuring that the dimensions of the microchannel could be measured accurately during fabrication, and 3) developing methods for controlling and measuring the roughness of the channels during fabrication.

The nominal depths and target roughness factors of the channels are shown in Table 2-1. The roughness factors are large due to the philosophy that it is easier to measure an effect at the largest roughnesses, and that if no effect were observed at the largest roughnesses, then no effect would be seen at smaller roughness values. For the smallest roughness values, the actual surface finishes correspond more to an optical polished condition, rather than a "rough" surface. The "roughest" surfaces, 1.25 and 2.5 μ , correspond to a surface condition that would be obtained by scratching a polished surface with 400 grit silicon carbide paper.

Table 2-1. Surface Profiles Required to Satisfy Desired Roughness Factors & Channel Depths.

Channel Depth (microns)	Roughness Factors		
	0.05	0.01	0.001
12	600 nm	120 nm	12 nm
25	1.25 μm	250 nm	25 nm
50	2.5 μm	500 nm	50 nm

The initial approach in the program was to use unetchable substrates with an etchable plating layer for the larger channel specimens. In this approach, the substrate would be plated to a substrate to a precise depth, and then the desired microchannel patterns would be etched into the plating. The etch process would then be allowed to proceed until the etch-resistant substrate is exposed. This would give a channel with a well-defined, consistent height, and a channel floor with well-defined roughness. The roughness could be achieved by pre-roughening the surface of

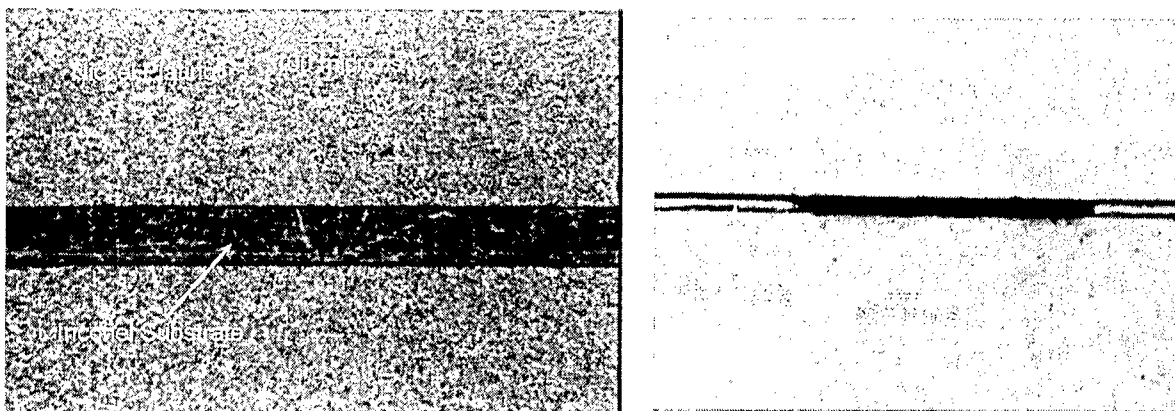


Figure 2-6. Plan View and Cross-sectional View of Nickel-Plated Inconel Substrate

the substrate prior to plating (or bonding), so that the roughened surface would be exposed after etching. The channel would then be capped with a cover plate, which would also possess a roughened surface.

At the outset of the program potential material systems for the flow test specimens were reviewed, resulting in the selection of a nickel/Inconel 625 systems. Nickel is easily etched in FeCl_3 , while Inconel 625 is extremely resistant to FeCl_3 , and is a stiff, strong material. An initial experiment was conducted to verify that an Inconel 625 foil could be plated with nickel and then diffusion bonded to an Inconel 625 cap plate. This experiment was performed using a $22\text{ }\mu\text{m}$ layer of Ni on a $250\text{ }\mu\text{m}$ Inconel 625 foil, diffusion bonded at $2100\text{ }^\circ\text{F}$. The sample was sectioned and examined metallographically for the quality of the bond. While no grain growth across the foil boundaries was observed, the cap plate appeared to be well-bonded to the nickel plating.

Subsequently the test was repeated with a $200\text{ }\mu\text{m}$ -wide channel etched through the nickel. The sample was sectioned in five places, and showed that the cap foil had collapsed to nearly completely fill the channel. This was attributed to the degraded mechanical properties of the Inconel at the diffusion bonding temperature, so a second trial was conducted at a temperature of $1600\text{ }^\circ\text{F}$. The sectioned sample showed no signs of collapse, with good dimensional stability ($\pm 5\%$) along the channel. Figure 2-6 shows a plan view and one of the cross-sections of the channel.

The need to achieve controlled roughness factors on microchannel surfaces was a primary factor in the decision to use the plating/etch-back fabrication approach described above. One series of experiments was performed to determine whether as-etched microchannels would meet the surface roughness requirements. Typically, electrolytically etched channels have a polished appearance and are smoother than chemically etched channels. To determine whether they would be smooth enough, test channels were etched in Inconel, stainless steel, and Invar in two different electrolytes. The channels were smooth by most standards, but were not smooth enough to meet the requirements set out in Table 2. This conclusion resulted in the decision to use prepolished plates with subsequent grinding, in order to achieve the needed roughness values.

Polishing experiments were performed on candidate materials for the outside sandwich plates (typical plates are shown in Figure 2-7). Hand polishing evaluations were performed on Inconel 625 and alloy 316 stainless steel. Both materials are easily polished. The Inconel 625 coupons appeared to have intrinsic inclusions, which were substantially harder than most of the metal. These inclusions resulted in an array of microscopic nodules on the surface with a typical dimension of about 1 micron. If one of these nodules occurred in a microchannel, it would result in a flow obstruction, an unacceptable result. The 316 stainless steel polished smoothly, so that 300 series stainless steel was selected for use in the outer sandwich layers.

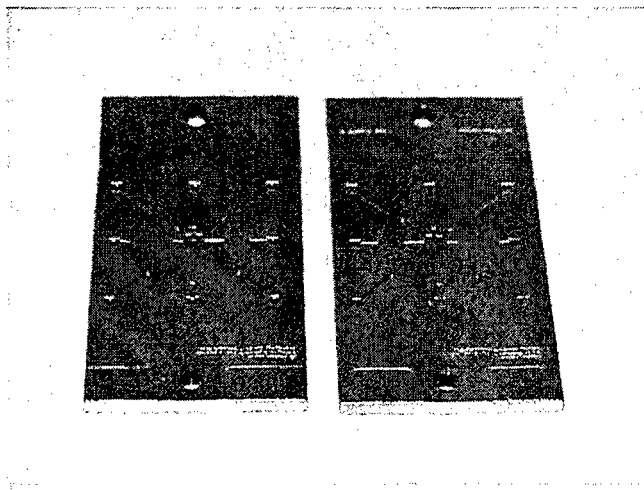


Figure 2-7. Typical Stainless Steel Substrates

Another experiment was performed to see if electroless nickel could be used in place of ordinary nickel plating. Electroless nickel plating has the advantage that it forms a uniform coating that it forms a uniform coating thickness all over a sheet so that edges and corners are not thicker and so that microchannels in any given sheet would all be the same thickness and would be uniform along their length. The disadvantage of electroless nickel is that it contains phosphorous, around 6% phosphorus in the type evaluated here. It was necessary to determine whether the electroless nickel would etch in ferric chloride or dilute nitric acid. Pure and commercial grades of nickel etch readily in these chemicals. Several coupons of Inconel 625 were coated with 25 microns of electroless nickel and tests were made to etch microchannels with ferric chloride and dilute nitric acid etchants. The electroless nickel did not etch normally in either etchant.

Modified Fabrication Process. The biggest inconvenience of the fabrication process described above (i.e., the nickel-plated Inconel substrate) was the fact that ordinary nickel plating is not flat from the corners to the edges to the center of a sheet of metal. On a research scale this effect can be minimized by using special baffles in the plating bath, but it is not practical for fabrication of a large number of specimens. For this reason, a modification of the initial approach for fabrication of microchannels was identified and implemented. The revised process involved diffusion bonding a sandwich made from two stainless steel plates and a thin piece of either copper or nickel foil, nickel being preferred because it is easier to diffusion bond.

The configuration is illustrated in Figure 2-8. Both of the stainless steel plates were lapped and polished. Then manifold grooves were etched in the stainless plates. Next, the microchannel area of each was ground to the desired roughness level using diamond grinding and polishing compounds. The copper or nickel foil was etched to include both the manifold grooves and the microchannels. Finally, the three-piece sandwich was diffusion bonded to seal the microchannels.

A flow test specimen with $20\text{ }\mu\text{m} \times 300\text{ }\mu\text{m}$ microchannels was fabricated and tested. There were several goals of the test: 1) verify the mechanical integrity of the specimens at internal pressures up to 2000 psi, 2) check out the prototype flow system, and 3) verify that the test data conformed to classical predictions. A simple flow testing apparatus was assembled, consisting of: 1) a high pressure gas bottle, 2) a high pressure tank with an internal bladder, 3) a fixture to hold the sample, and 4) an upstream pressure gauge and downstream beaker to collect the flow. The bottle was used to pressurize the tank, which contained deionized water. The water flowed through stainless steel tubing, through the pressure gauge (located just upstream of the specimen), through the microchannel and into the beaker.

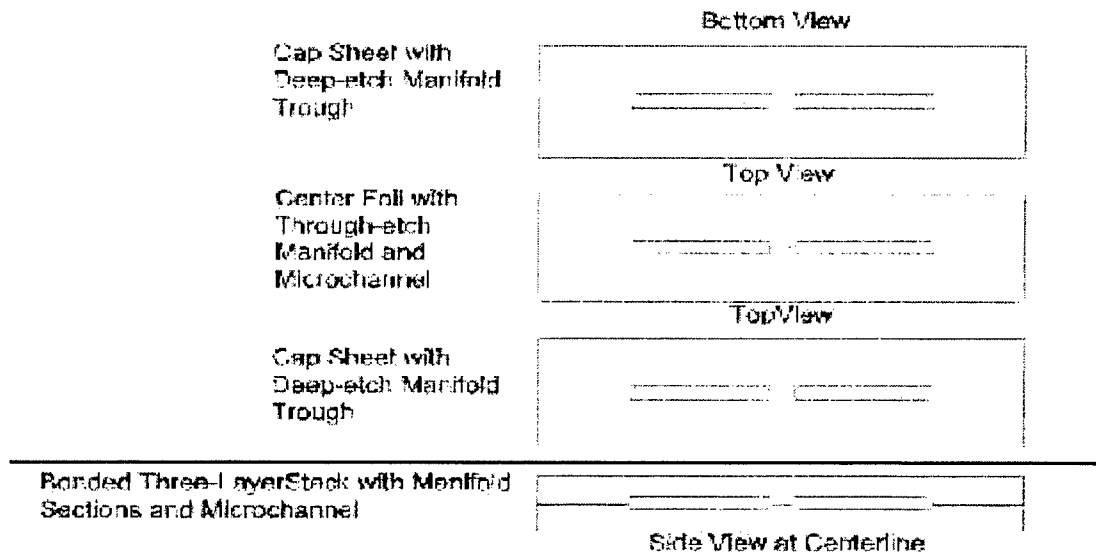


Figure 2-8. Improved microchannel fabrication approach.

The test data agreed with classical predictions; the tests were conducted at gauge pressures up to 2000 psi with no apparent effect on the sample. The tests were repeatable within a few percent, although the samples were repeatedly observed to clog with an organic material. This was found to come from the bladder of the tank, and so electropolished stainless steel tanks were ordered for use in the actual test series. It was found that heating the samples in a torch was sufficient to restore them to their original condition.

2.1.1.2 Fabrication of Small (<10 μ m) Microchannels

UCI was responsible for fabrication of samples with minimum dimensions below 10 μ m. The fabrication of the small channels required the micromachining and sealing of long microchannels in silicon. The target depths, widths, and surface roughnesses are outlined in Table 2-2 below. The construction of these channels is made difficult by the lengths involved coupled with the shallow depths required. For example, a 2 μ m channel will be unsealable if a single sub-micron particle falls anywhere within the seal region. For a 1 inch channel, the seal region is quite large, requiring very high clean room conditions for success. In addition, the testing requirements called for the seal to be good up to 3000 psi, at a temperature of 200° C. This requirement places extra difficulty in the design and construction of the channels, seals and mounting method.

Table 2-2. Target Dimensions and Roughnesses of Silicon Microchannels

Depth	Width	Length	Rough (1)	Rough (2)	Rough (3)
1.0 μ m	4.0 μ m	0.12 in	1.6 nm	34.6 nm	115.5 nm
1.0 μ m	10.0 μ m	0.15 in	1.8 nm	55.2 nm	144.3 nm
2.0 μ m	8.0 μ m	1.0 in	3.2 nm	121.7 nm	962.1 nm
2.0 μ m	20.0 μ m	1.25 in	3.6 nm	245.4 nm	1.2 μ m
5.0 μ m	20.0 μ m	2.0 in	8.0 nm	287.0 nm	1.92 μ m
5.0 μ m	50.0 μ m	2.5 in	9.1 nm	559.5 nm	2.4 μ m

Process Overview

The following processes were evaluated for creating the micromachined silicon channels.

Silicon etch with anodic bonding to glass

The first approach considered is to etch the silicon using a standard wet etchant, either potassium hydroxide (anisotropic) or a mixture of nitric acid, acetic acid, and hydrofluoric acid (isotropic). The concentration and temperature of the etch determine both the etch rate and the roughness of the surface. By varying these parameters, different roughnesses can be achieved. Following the silicon etch and subsequent cleaning, a flat glass plate of borofloat glass (similar to Pyrex 7740 glass) is anodically bonded to the channel to form the seal. The sealed unit is then mounted in a holder using high temperature, high strength epoxy. The details of this process are shown in Tables 2-3 and 2-4.

Metal growth with anodic bonding to glass

A second approach considered is to pre-roughen the silicon using an abrasive, then deposit metal on the silicon surface, building up to the desired channel depth. After metallization, the channels are etched into the metal, using standard metal etchant chemistries. Since the metal is etched all the way to the silicon, the etch roughness is unimportant. Finally, glass plate is anodically bonded to the metal. This method has attractive features, however, the thicknesses required (greater than 1 micron) make vacuum deposition unsuitable and metal deposition must be done by electroplating. Furthermore, not all metals will anodically bond to glass. The details of this process are shown in Table 2-5.

Sacrificial etching

A third approach, which may have merit, is to build the microchannel by etching away a sacrificial material. The sacrificial material is deposited on a pre-roughened silicon substrate and patterned in the shape of the channel. Following this, a structural layer is deposited over the pattern. This structural material may be oxide, or it may be a high strength, high temperature epoxy. The piece is then soaked in an etchant, which is selective to the sacrificial layer, to remove it. This method eliminates many of the problems associated with sealing in an ultra-clean environment. However, it has the serious drawback that the etchant may not penetrate into a long, shallow channel. This is especially true if the etchant is a liquid which produces bubbles during the etch. In this case, it may make more sense to use a vapor etchant for the sacrificial material. The details of this process are shown in Table 2-6.

Experiments. All three processing methods were evaluated. The silicon etch with anodic bonding was the most conventional approach, and most of the work was done using this process. The long channel lengths required patterning the full wafer directly from the original photographic plate (usual step and repeat reduction cannot be employed), and the smallest dimension (4 microns) was at the lower limit of UCI's capabilities. Both of these limitations affected the quality of the final results.

Original work was performed using a large design, involving a two mask process, the first requiring an etching of 100 microns followed by a 1 micron etch. The idea was to use large, deep leader channels (several millimeters width by 100 microns depth), which ended with the smaller, shallow channel of interest bridging a dam between the two. As a preliminary trial, a demonstration specimen with 5 μm x 50 μm channels was fabricated, as shown in Figure 2-9a-d (the figure includes four views of the sample at various orientations and magnifications). Several material systems were considered for the sample - the selected system was finally just a silicon channel etched with the desired pattern. Figure 2-9 shows a closeup of the channel, which is flanked by large Apool® areas which serve as manifolding for the channel.

A profilometer was used to measure the channel depth - as shown in Figure 2-10. Several surface texturing experiments were also performed to assess the controllability and uniformity of smooth and roughened surfaces, with results shown in Figures 2-11 and 2-11a. The roughness was varied by modifying the etch temperature, and the potassium hydroxide and isopropyl alcohol concentrations. As the results in Figure 18 show, one of the smoothest surfaces had an average roughness of approximately ± 5 nm, or $\pm 0.1\%$ of the minimum channel dimension. The roughness of the glass cover plate that forms the fourth wall of the channel was also of interest. Figure 2-12 shows the roughness profile of the glass plate, which had an average value of 0.25 nm.

This approach had several drawbacks to it. First, the two mask process was difficult to execute due to the fact that the 100 micron channels needed to be etched first. The deep channel depth caused problems when trying to spin on the thin film of photoresist needed to do the second mask. Second, the large surface area added by the leader channels made anodic bonding more difficult. Third, the channel lengths combined to make a total pattern, which was too large for the standard photolithography equipment at UCI. Finally, the forces associated with the large leader channels at 4000 psi are such that a special, high strength jig was needed to keep the assembly from breaking apart during measurement. Ultimately, this design was abandoned for a simpler method (described in Section 2.1.2.2).

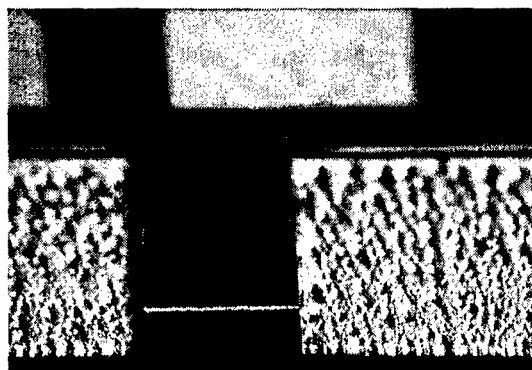
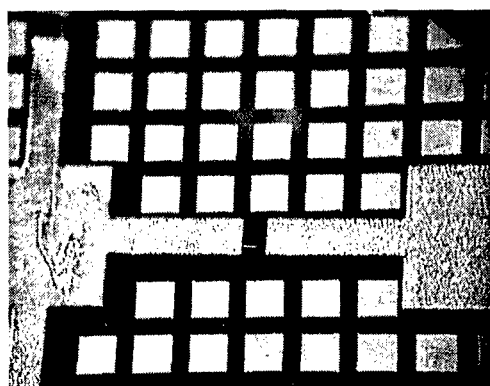
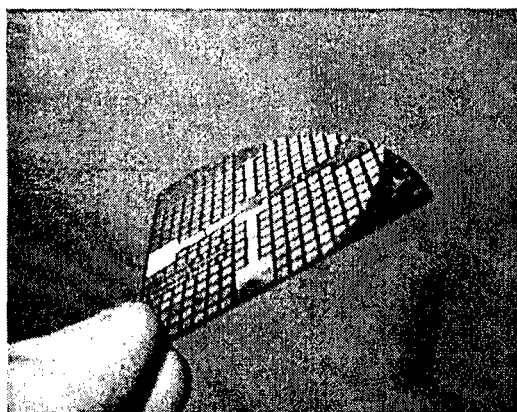
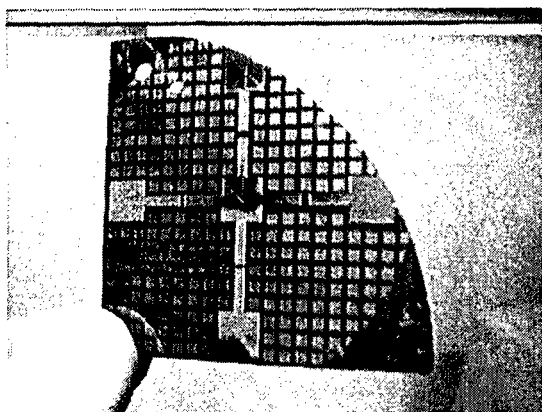
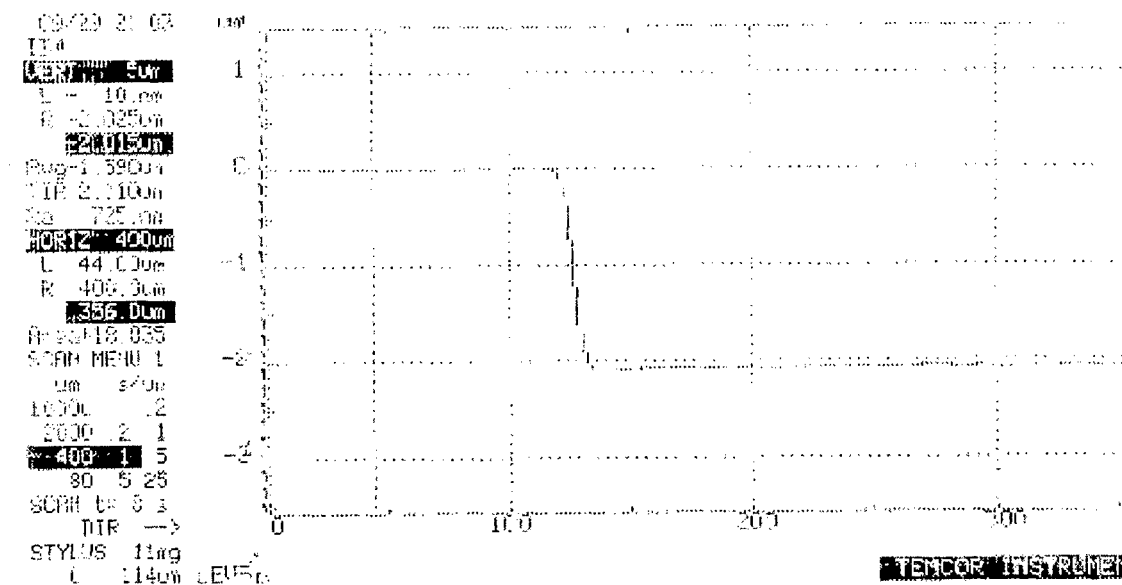


Figure 2-9c. Closeup of Etched Si Wafer

Figure 2-9d. Closeup of 5 μm x 50 μm Channel

Figure 2-10. Profile Scan of 20 μm Channel Plate. Scan was done on air traps adjacent to the channel (channel width was too small for profile scan). Depth is 2.3 μm . Profile was unable to determine roughness.



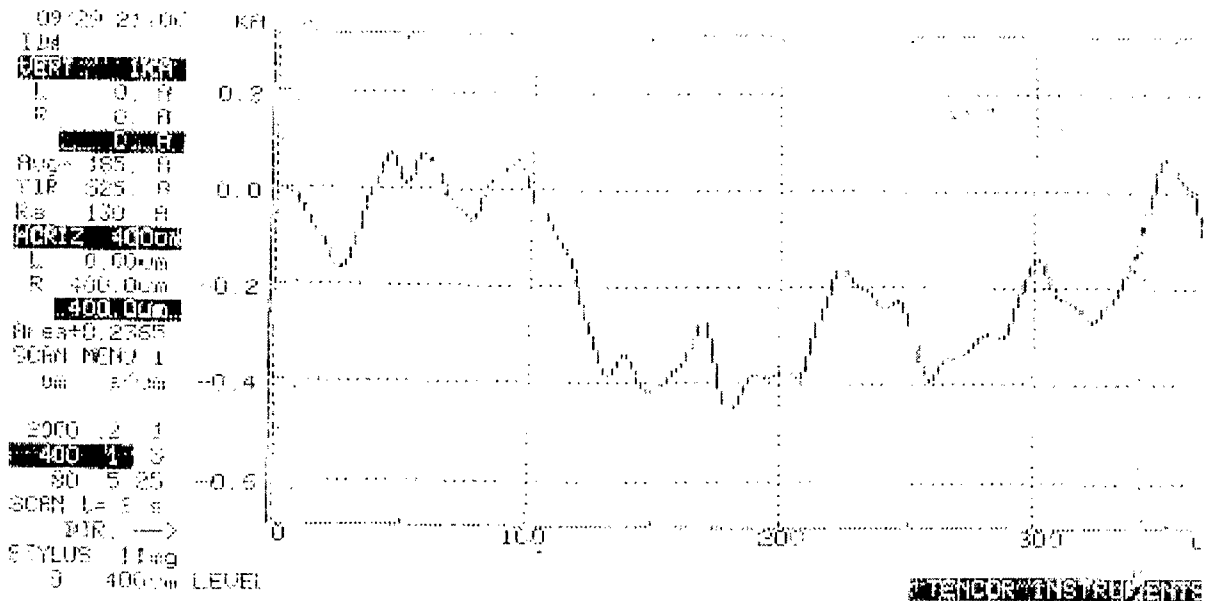


Figure 2-11. Ra of two 20 micron Channels: Upper Scan 130 A, Lower Scan 70 A

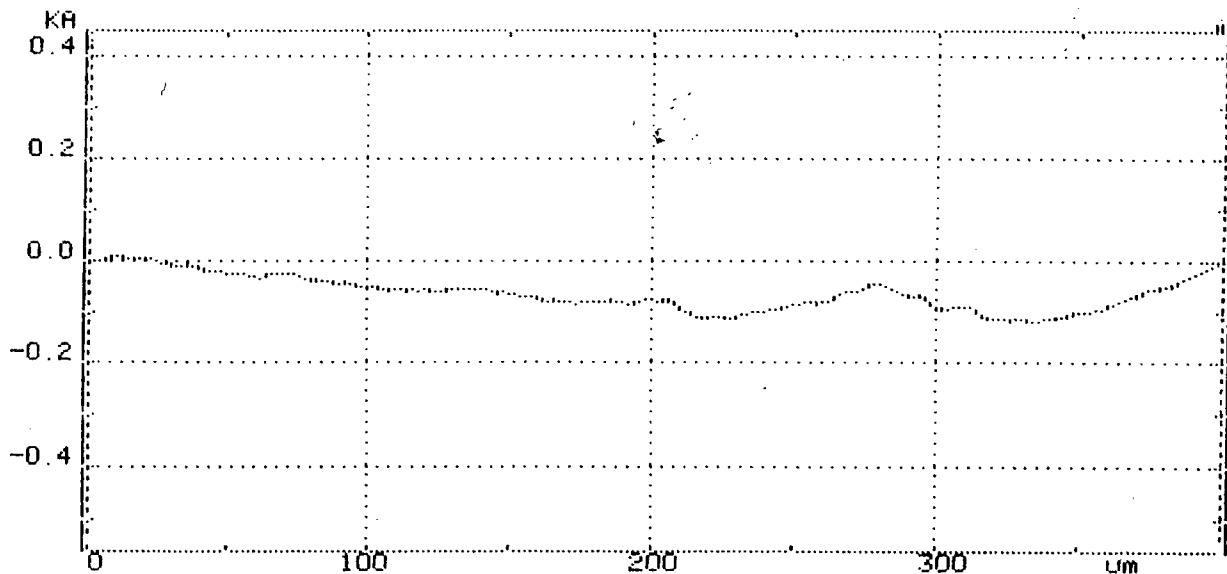


Figure 2-12. Roughness of Glass Slide: $R_a = 25 \text{ \AA}$

Alternate Approaches. The metallization processing technique may avoid some of the dust problems in two ways. First, since the metal is etched all the way through to the substrate, dust can be “undercut” by the etching, leaving no artifacts. Second, metal is more compliant than silicon, which allows the seal to conform slightly around any foreign particles, still forming a seal. The main problems were in finding a metal which can be easily deposited in thin films (through plating or evaporation), which have the necessary strength and temperature resistance, and which form anodic bonds with glass. One promising approach was to use gold with copper interdiffused within it.

Preliminary work was also performed on use of a sacrificial approach to creating channels. In this approach, patterned photoresist was coated with epoxy or metal. The ends were cut using a diamond saw, and then the piece was soaked in acetone. Unfortunately, the cutting caused damage to the end surface so that the channel apparently becomes clogged, and the acetone cannot get in to attack the photoresist. Sawing must be accompanied by polishing. While it was not explored further in the program due to these initial difficulties, the sacrificial approach has the potential to allow the fabrication of channels using a variety of materials besides silicon, metal, or glass.

Table 2-3. Silicon Etch With Anodic Bonding to Glass, KOH Method Process Outline

Grow Thermal Oxide	<ul style="list-style-type: none"> Starting with polished 100 silicon wafers, grow 1 micron hard oxide mask over the surface using 100°C steam ("wet ox")
Pattern Channels	<ul style="list-style-type: none"> Clean wafer surface using standard process Follow with dehydration bake at 90°C Spin on Shipley 1827 positive photoresist at 400 rpm for 30 seconds, followed by a soft at 90° C Pattern channels mask (negative mask), using UV exposure. Develop photoresist, hard bake at 90°C for 30 minutes
Etch Hard Mask	<ul style="list-style-type: none"> Etch oxide layer using reactive ion etching with $\text{CHF}_3 + \text{O}_2 + \text{SF}_4 + \text{O}_2$ Etch until silicon is exposed Clean off photoresist with acetone, thin dip in buffered HF solution for 30 seconds to remove any traces of oxide mask covering patterned areas
Etch Silicon	<ul style="list-style-type: none"> Prepare KOH solution and heat to 65°C Dip silicon in etchant for 1 minute, agitating solution vigorously. Check depth with profilometer Repeat every 30 seconds until desired etch depth is achieved. Characterize roughness using profilometer
Remove All Oxide	<ul style="list-style-type: none"> Soak part in buffered HF for 15 minutes to remove all traces of the oxide mask. Remaining part should be bare silicon
Cleave Silicon	<ul style="list-style-type: none"> Using special jig, cleave silicon to proper size. Channel should be exposed at both ends
Cut Glass	<ul style="list-style-type: none"> Using diamond saw, cut glass to proper size
Final Clean	<ul style="list-style-type: none"> Clean well, making sure to remove any and all particles, dust or residue from the silicon surface. Dip silicon in buffered HF for 10 minutes to remove any traces of native oxide. Air dry with nitrogen. Clean glass similarly, but do not dip in HF
Anodic Bond	<ul style="list-style-type: none"> Directly following cleaning, place glass on silicon surface Place combination in special anodic bonding jig Heat to 300°C Apply -800V across the glass for 5 minutes. Glass and silicon should form strong bond and seal
Final Mounting	<ul style="list-style-type: none"> Mount glass/silicon device in specially machined holder

Table 2-4. Silicon Etch W/Anodic Bonding to Glass, Isotropic Etch Method Process Outline

Grow Low Stress Nitride	<ul style="list-style-type: none"> Start with polished 100 silicon wafers, grow a dense, 0.5 micron low stress nitride using low pressure chemical vapor deposition (LPCVD)
Pattern Channels	<ul style="list-style-type: none"> Clean wafer surface using standard process Follow with dehydration bake at 90°C Spin on Shipley 1827 positive photoresist at 400 rpm for 30 seconds, followed by a soft at 90° C Pattern channels mask (negative mask), using UV exposure. Develop photoresist, hard bake at 90°C for 30 minutes
Etch Hard Mask	<ul style="list-style-type: none"> Etch oxide layer using reactive ion etching with $\text{CHF}_3 + \text{O}_2 + \text{SF}_4 + \text{O}_2$ Etch until silicon is exposed Clean off photoresist with acetone
Etch Silicon	<ul style="list-style-type: none"> Prepare solution of acetic acid, nitric acid and hydrofluoric acid Dip silicon in etchant for 1 minute, agitating vigorously. Check depth with profilometer Repeat every 30 seconds until desired depth is achieved Characterize depth with profilometer
Remove All Nitride	<ul style="list-style-type: none"> Soak part in buffered HF for 24 hours to remove all traces of the nitride mask Remaining part should be bare silicon
Cleave Silicon	<ul style="list-style-type: none"> Using special jig, cleave silicon to proper size. Channel should be exposed at both ends
Cut Glass	<ul style="list-style-type: none"> Using diamond saw, cut glass to proper size
Final Clean	<ul style="list-style-type: none"> Clean well, making sure to remove any and all particles, dust or residue from the silicon surface. Dip silicon in buffered HF for 10 minutes to remove any traces of native oxide. Air dry with nitrogen. Clean glass similarly, but do not dip in HF
Anodic Bond	<ul style="list-style-type: none"> Directly following cleaning, place glass on silicon surface Place combination in special anodic bonding jig Heat to 300°C Apply -800V across the glass for 5 minutes. Glass and silicon should form strong bond and seal
Final Mounting	<ul style="list-style-type: none"> Mount glass/silicon device in specially machined holder

Table 2-5. Metal Buildup With Anodic Bonding to Glass Process Outline

Clean Wafer	<ul style="list-style-type: none"> Starting with polished 100 silicon wafers (or glass substrate), clean to remove all organic residues and native oxides
Metallize Wafer Using Vacuum Deposition	<ul style="list-style-type: none"> Use the electron-beam evaporator to deposit 500 Å chrome, followed by a thin 1000Å layer of gold.
Continue Metallization Using Electroless Plating	<ul style="list-style-type: none"> Deposit Ni over gold using Electroless plating Plate until desired thickness is achieved (channel depth)
Pattern Channels	<ul style="list-style-type: none"> Clean wafer surface using standard process Follow with dehydration bake at 90°C Spin on Shipley 1827 positive photoresist at 400 rpm for 30 seconds, followed by a soft at 90° C Pattern channels mask (negative mask), using UV exposure. Develop photoresist, hard bake at 90°C for 30 minutes
Etch Metal	<ul style="list-style-type: none"> Etch metal using metal etchant which is selective to photoresist
Cleave Silicon	<ul style="list-style-type: none"> Using special jig, cleave silicon to proper size. Channel should be exposed at both ends
Cut Glass	<ul style="list-style-type: none"> Using diamond saw, cut glass to proper size
Final Clean	<ul style="list-style-type: none"> Clean well, making sure to remove any and all particles, dust or residue from the metal surface. Air dry with nitrogen. Clean glass similarly
Anodic Bond	<ul style="list-style-type: none"> Directly following cleaning, place glass on silicon surface Place combination in special anodic bonding jig Heat to 300°C Apply -800V across the glass for 5 minutes. Glass and silicon should form strong bond and seal
Final Mounting	<ul style="list-style-type: none"> Mount glass/silicon device in specially machined holder

Table 2-6 Sacrificial Etching Process Outline

Clean Wafer	<ul style="list-style-type: none"> Starting with polished 100 silicon wafers (or glass substrate), clean to remove all organic residues and native oxides
Pattern Channels	<ul style="list-style-type: none"> Clean wafer surface using standard process Follow with dehydration bake at 90°C Spin on Shipley 1827 positive photoresist at 400 rpm for 30 seconds, followed by a soft at 90° C. This gives 2.2 micron thickness. Pattern channels mask (positive mask), using UV exposure. Develop photoresist, hard bake at 90°C for 30 minutes
Deposit Structural Material	<ul style="list-style-type: none"> Deposit structural material using one of many possible approaches Metallization (using evaporation), oxide growth (using plasma enhanced chemical vapor deposition), or simple application of epoxy
Cleave or Cut Substrate	<ul style="list-style-type: none"> Using special jig, cleave substrate to proper size or cut with diamond saw. Sacrificial material, which forms the channels, should be exposed at ends. If channel is not exposed, ends should be polished to reveal the sacrificial material
Etch Sacrificial Material	<ul style="list-style-type: none"> Soak device in warm acetone overnight. If photoresist is not removed, try ultrasonic cleaner to aid removal
Final Mounting	<ul style="list-style-type: none"> Mount device in specially machined holder

2.1.2 MICROCHANNEL TEST ASSEMBLY

2.1.2.1 Metal Microchannel Test Assembly

A conceptual design of the flow performance test stand for the larger channels is shown in Figure 2-13. As the figure shows, the bonded flow specimen is clamped to the test fixture by the top mounting plate. Fluid enters through a central plenum, travels along the various channels, and exits through the fluid return lines. Not shown is the pressure transducer, which is mounted in the top mounting plate over the central plenum. The fluid return lines travel to their respective flow reservoirs, where they discharge the fluid at the same height as test article. Upon completion of the test the return lines are detached from the fixture and weighed together with their flow reservoir - ensuring that fluid residing within the lines is accounted for.

Figure 2-14 shows a schematic of the entire flow performance test system. The flow is supplied by an accumulator pressurized by a gas bottle. This prevents introduction of vibrations or flow pulsations into the system as might be experienced with a pump. The hand pump is used to refill the accumulator at the end of a test series. During testing, the flow travels toward the flow fixture, which is mounted on a vibration isolation stand. Avoiding introduction of vibrations into the flow system is desired so that early onset of transition is prevented. After passing through the microchannels, the liquids are collected as described above.

The test setup for the liquid flow tests consists of serological pipettes inserted above the outlets of each microchannel. A pressure gauge or transducer is placed upstream of the inlet manifold. The timing of the displacement of the water in the pipette determines the volumetric flowrate for that channel. Figure 2-15 shows eight microchannels simultaneously being tested in the water flow test setup.

The nitrogen testing approach consists of collecting nitrogen bubbles from a submerged sample underwater. The nitrogen is captured from a water-filled, inverted graduated cylinder. The timing of the displaced volume of nitrogen results in a volumetric flowrate.

Experimental Error. The test procedure is designed to provide low measurement errors. The flow rates for microchannels are very low, making flow collection advantageous over use of flow meters. The test times were designed to provide sufficient total flow (25 ml) such that measurement inaccuracies (~ 0.1 ml) and the potential for trapping of fluid in the system (~ 0.25 ml) were negligible ($\sim 1.4\%$ error). The pressure gauge had an accuracy of 2%, and was replaced in later tests by a No-Shok pressure transducer with 0.1% accuracy. The total RMS error was slightly above 2%. A type K thermocouple was placed on the test piece to measure the fluid temperature. This measurement was accurate to 0.5°C .

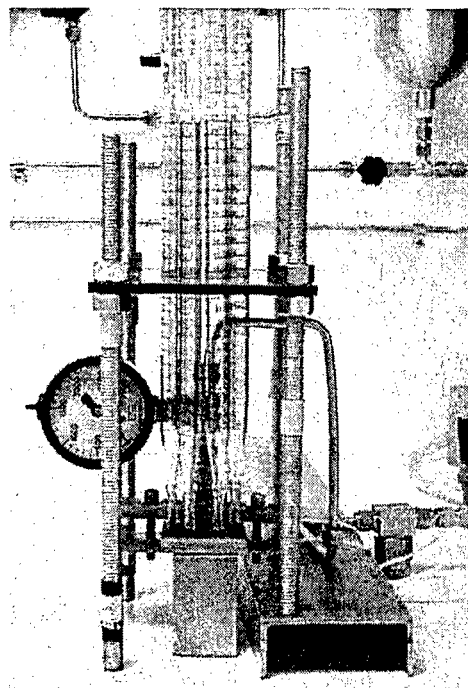


Figure 2-13. Flow Experiment

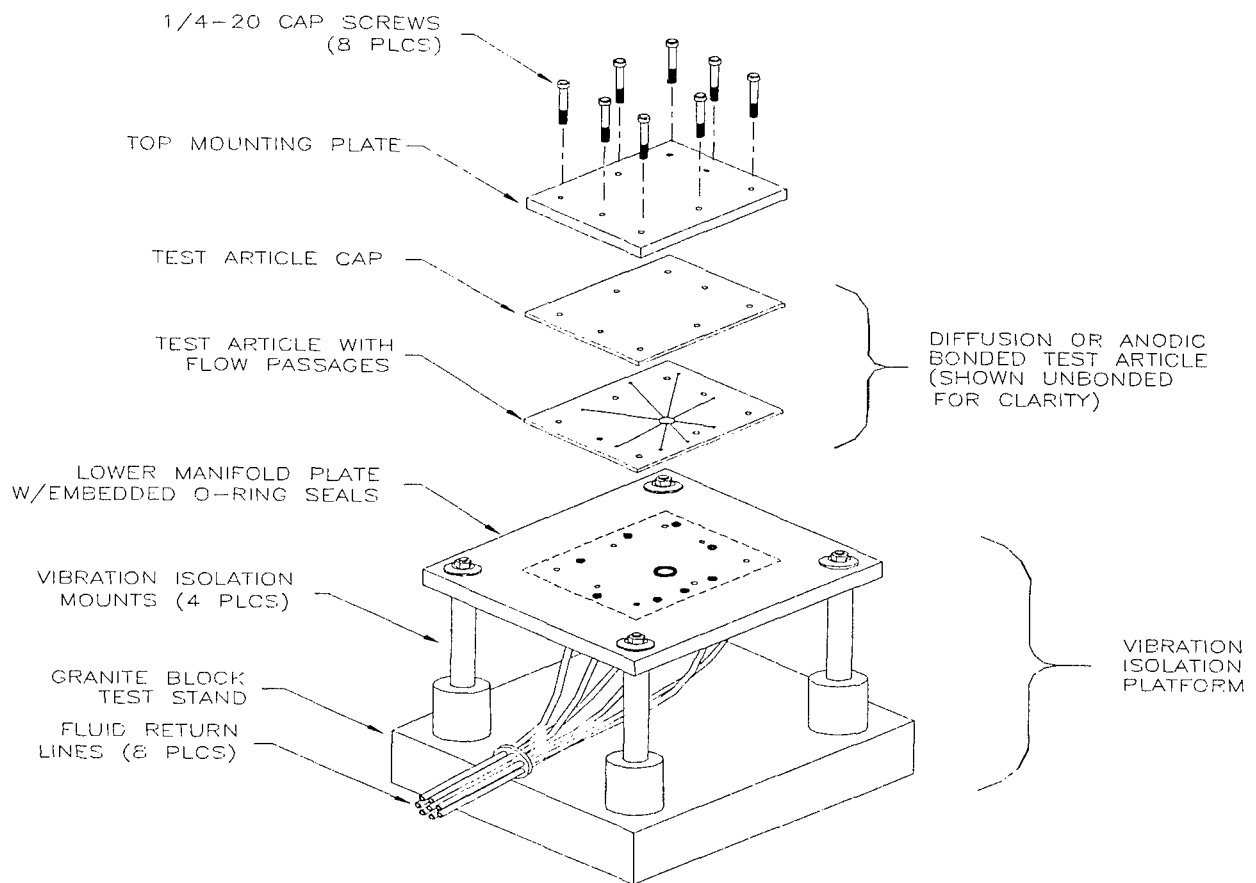


Figure 2-14. Flow Performance Test Stand Schematic

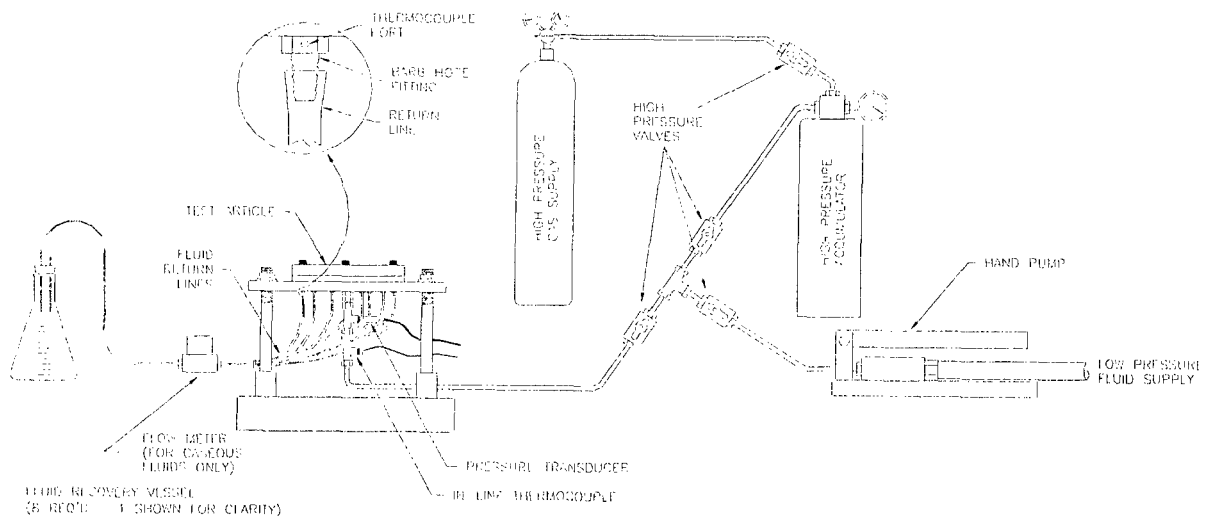


Figure 2-15. Schematic of Flow Testing Experiment

2.1.2.2 Silicon Microchannel Test Assembly

The first silicon microchannel received from UCI was mounted in a high-pressure fitting and attempts were made to perform flow tests. The mounted assembly was clogged. Destructive evaluation of the mounted assembly showed that the microchannel exit was clogged by epoxy, which had wicked, by capillary action, along corners of the assembly.

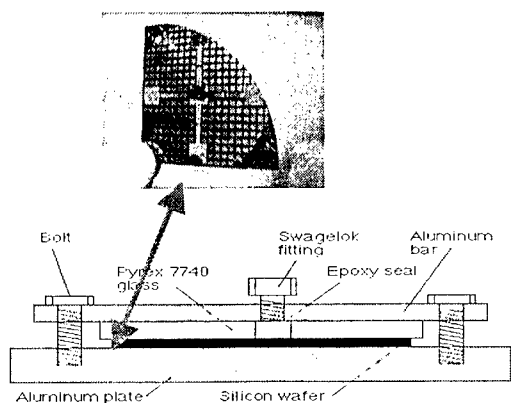
There were practical issues with the mount design as well. The test sample was sandwiched between two aluminum plates. Because a maximum load of 2000 psi was required during testing, the durability of the seal used at the inlet manifold was in question. Testing conditions required the fluid to be under pressure and heated to 150°C. After repeated testing of the silicon microchannel, the assembly and disassembly of the system proved too time consuming.

An improved design approach proposed by UCI mounted one end of the microchannel into a high pressure fitting with the exposed end of the microchannel subjected to high pressure and the exit of the microchannel inside the fitting as shown in figures 2-16 and 2-17. The new fixture design developed by UCI offered superior mechanical attachments and multiple test capability without disturbing operating conditions. This design kept the microchannel assembly itself under hydrostatic compression and eliminated simple shear stresses on the epoxy.

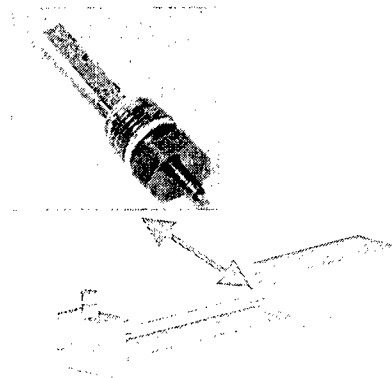
The new design built the channel into a 0.25 in wide silicon slot, with the ends of the channel exposed, as shown in Figures 2-17. The ends were cleaved to the desired length, as shown in Figure 2-18. The small size of the device required that a special jig be built for the anodic bonding station to hold it in place. This design simplified the mask and jig design, but required that the channel to be mounted (glued) in place within the special jig holder. The bond was required to withstand 200°C at 3000 psi. The UCI group recommended using two sealants. The first was a high viscosity, high strength adhesive that can be used over a large temperature range. A candidate for this would be Loctite urethane adhesive 2214HP. The second was a high temperature anaerobic thread sealant, such as Loctite sealant 592, which can be used to seal any small cracks between the epoxy and the channel plate.

By far, the greatest obstacle to success in this approach was the problem of stray dust, particles, or residue left on the channel or sealing path during processing. Dust in the channel path affects the etching and often leaves etching artifacts in the channel. This is particularly troublesome for the KOH process, which can leave large pyramid structures around dirt particles. Furthermore, particles on the sealing path prevent complete sealing of the channel. Despite these problems two prototypes were produced which were intended to serve as test vehicles for the flow measurement system.

In the test fixture for the new mounting design, the silicon microchannel was inserted into an aluminum housing (Figure 2-18) with the fitting exposed. The volumetric flowrate is then taken from the displacement of the fluid within a capillary that is inserted within the fitting. The capillary was enclosed in a vacuum-sealed Pyrex tubing to maintain the necessary equilibrium vapor pressure of the FC-72 3M Fluorinert during testing. The displaced fluid is reset in the capillary by pulling or pushing the capillary in place. The silicon microchannel test fixture as fabricated is shown in Figure 2-19.



(a) Old Fixture Design



(b) New Fixture Design

Figure 2-16. Silicon Wafer Microchannel Fabrication and Test Fixture Design Update.

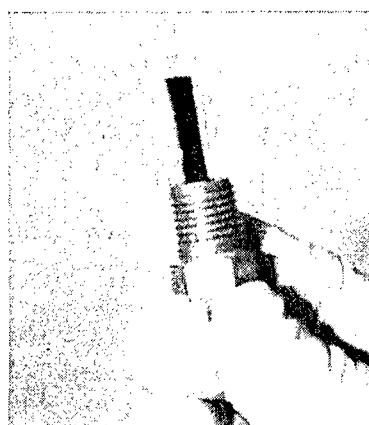
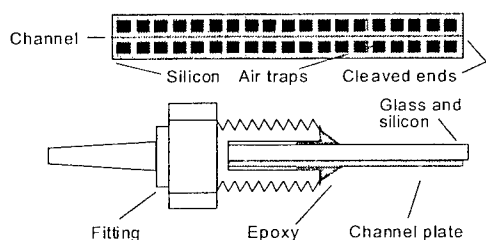


Figure 2-17. Diagram showing second channel design and jig assembly for holding the assembly during testing. Air traps are to aid in anodic bonding. Fitting is a standard high pressure fitting.

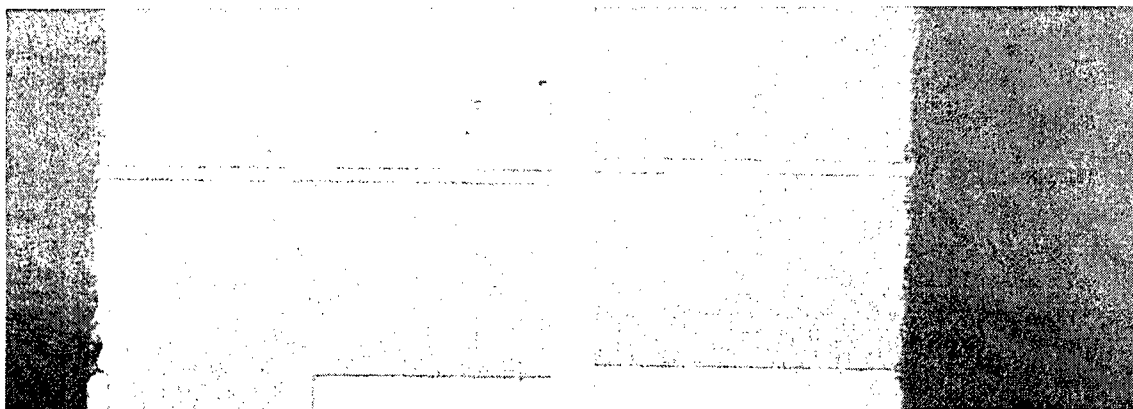


Figure 2-18. Photos of 20 micron channel, 2 micron depth, showing cleaved ends.

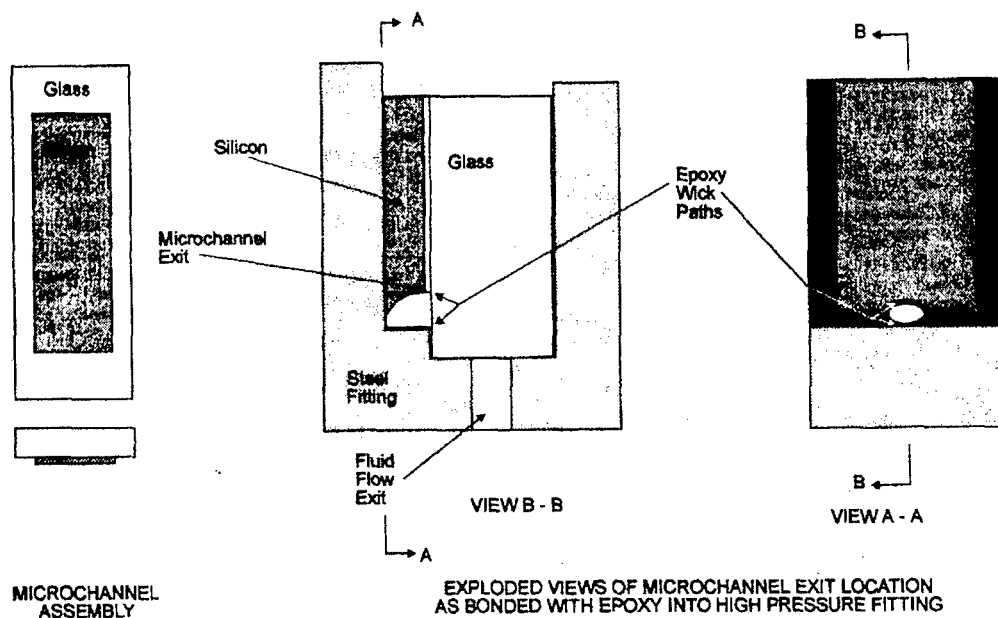


Figure 2-19. Silicon Microchannel Schematic.

FABRICATION OF THE MICROCHANNEL TEST ASSEMBLY

Implementation of the new mounting approach was not trivial due to the small size of the parts, the proposed temperature of operation (150°C), and the fact that the microchannel/glass assembly exterior dimensions were not fabricated to tight tolerances. One of the primary issues was that the end of the silicon piece was not a square cleavage nor was the end of the silicon piece parallel to the end of the glass piece.

Although the new approach offered significant flow and testing benefits, clogging remained a serious concern. The microchannel had to be epoxied into Swagelock fitting. The testing of the 2µm depth channel resulted in a clogged microchannel caused by the epoxy.

The first mounting design approach is illustrated in Figure 2-19. The basic microchannel assembly is shown at the left of the figure with the silicon chip anodically bonded to a piece of glass with the actual microchannel at the interface between the silicon and the glass. In the middle of Figure 2-19 is an exploded view of the microchannel assembled into the high-pressure stainless steel fitting. A slot was machined into the fitting such that the glass piece would bottom out on the steel fitting and the end of the silicon wafer would be close to a step in the steel fitting. This approach assured that the glass would absorb the compressive load from the external gas pressure and that there would be no shear loads applied to the epoxy bond or to the silicon/glass interface.

The actual microchannel test assembly was bonded together using Emerson and Cumming Stycast 2662, a high temperature epoxy that will not only withstand the operation temperature but also retain high strength. The bonding operation was performed in three steps. The first step involved application of small spots of epoxy at the bottom corners of the silicon chip and the bottom corners of the glass. Especially for the silicon chip, the amount of epoxy was selected to be less than what would be necessary to fill the gap between the microchannel and the step in the steel fitting. The epoxy was cured. Next, a second application of small amounts of epoxy was used to make sure that the area near the microchannel exit would be sealed from the exterior. The epoxy was again cured. Finally, all remaining large gaps were potted completely with epoxy to assure that the assembly would withstand high pressures.

TESTING AND POST-TEST ANALYSIS OF THE MICROCHANNEL ASSEMBLY

Pressure testing of the microchannel assembly with nitrogen up to 3.4 MPa (500 psi) showed that there was no flow. Destructive evaluation of the assembly was used to determine whether epoxy had clogged the microchannel or whether there was some other cause. The steel fitting was machined away to reveal the view marked A-A in Figure 2-19. This view is illustrated in the right side of Figure 2-19 and is also shown in the macrophotograph of Figure 2-20. It was necessary to manually break away the curled edge of the silicon chip to be able to see the location of the exit of the microchannel.

The photograph indicates that epoxy had wicked by capillary action across the two corner interfaces at the top and the bottom of the exit cavity under the microchannel. The assembly procedure was successful in the sense that epoxy did not actually run as a liquid and fill the cavity under the microchannel. However, what was not anticipated was that the epoxy itself would separate from its filler and wick as a lower viscosity fluid across the two corner interfaces to clog both the microchannel exit and the exit passageway to the fitting.

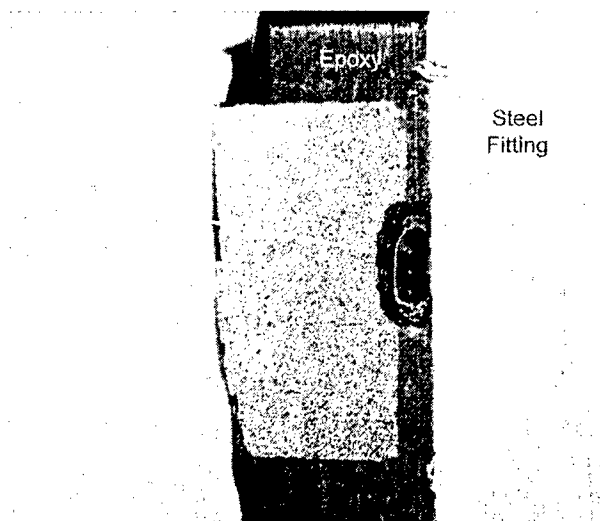


Figure 2-20. Photograph of cross-section of 2 μ m depth silicon microchannel

2.2 Results of Experiments

Flow experiments using air, water, and FC-72 were conducted on each of the test samples. Photographs and descriptions of the test samples and the raw data collected during the testing are all included in Appendix A of this report. The sections below address the data treatment, experimental accuracies, and conclusions of the testing.

2.2.1 Laminar Friction Factor Coefficient Results

From classical theory (Shah & London, 1978), the pressure drop through a passage in laminar flow can be modeled on an engineering basis as the dynamic pressure multiplied by the combination of frictional losses and minor losses:

$$\Delta p = \frac{l}{2} \rho V^2 \left(\frac{f^* L}{D} + K \right)$$

where Δp is the pressure drop, ρ is the density, V is the velocity, f is the friction factor, L is the passage length, D is the hydraulic diameter of the passage, and K is the sum of the minor loss coefficients associated with entrance (including flow development) and exit effects.

The laminar friction factor is generally defined as: $f = \frac{C}{Re}$

where C is 64 for a circular passage, and varies as a function of aspect ratio (α) from 54 to 96 for rectangular passages. Investigations of microchannel flow performance generally concentrate on assessing the value of C , and determining whether it deviates from the theory for macro-channels. For rectangular channels, the value of C in fully developed laminar flows can be calculated as (Shah and London, 1978):

$$C = 96(1 - 1.3553\alpha + 1.9467\alpha^2 - 1.7012\alpha^3 + 0.9564\alpha^4 - 0.2537\alpha^5)$$

This value was used as C_{pred} in the data presentations. The value of C derived from the experiments is denoted as C_{meas} . This value was obtained by selecting the portion of each flow rate-pressure drop data set that was clearly linear, as would be expected for the laminar flow regime. The data reduction neglected entrance and exit loss effects, which are small when the data is linear. C_{meas} was then obtained by calculating a linear fit through the selected data.

The measurement of the channel width is the most critical parameter in the experiments. Figure 2-21 shows the sensitivity of the pressure drop to a 2.5 μm error and a 1.25 μm error in measuring the channel width. As shown, the error never drops below 5% even for the largest channels. The error is also asymmetric, with an error on the low side of the channel width yields a much larger increase in the predicted pressure drop than an error on the high side. The accuracy of channel width measurements in this program ranged between 1.25 and 2.5 μm . This was a key reason that the straight smooth channels were used as a reference for the other experiments, and why care was taken to place the roughened channels on the same test piece as the smooth channels (to ensure that they had the same channel width (= the foil thickness)).

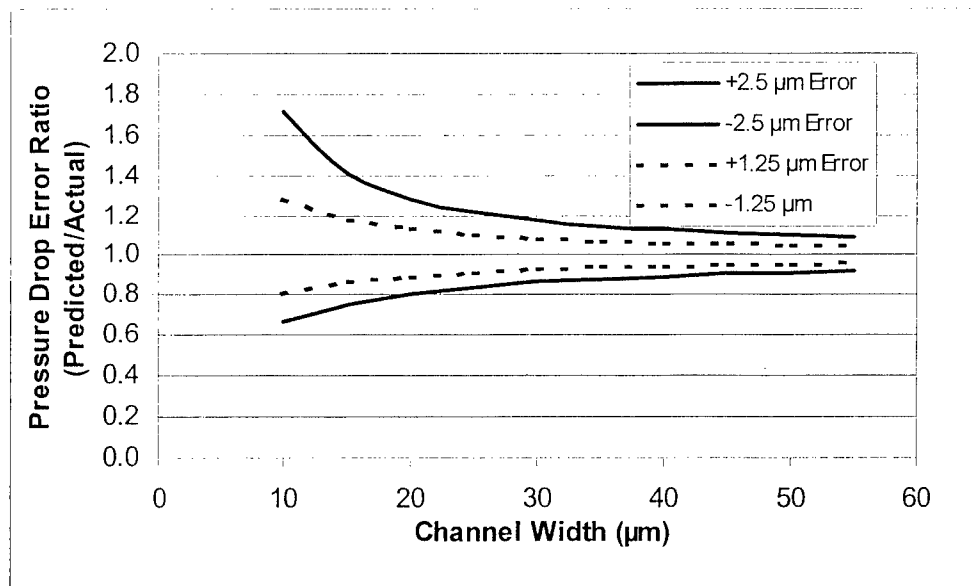


Figure 2-21. Sensitivity of Results to Errors in Channel Width Measurement

Nitrogen Data Reduction. Due to the compressibility of nitrogen at Mach numbers greater than about 0.3, the model used previously for computing the theoretical pressure drop for a given inlet Reynolds number cannot be used. A compressible flow model was developed and used to compute the theoretical pressure drop for comparison with experimental data.

The flow quantities are computed as a function of streamwise distance by integrating the differential conservation equations for mass, axial momentum, and energy. These equations, coupled with the equation of state, allow the pressure drop across a channel to be computed given an inlet Reynolds number and an inlet static pressure. The inlet static pressure was iterated on to give a channel where the pressure is expanded to atmospheric pressure at the inlet (as was the case in the experimental setup). All channels were found to choke for high enough Reynolds number. The model captured this by predicting a Mach number of 1 at the channel exit before atmospheric pressure was reached. Reynolds number was based on hydraulic diameter, and the friction coefficient in the axial momentum equation was determined using the correlation with aspect ratio developed by Shah and London.

Experimental Results. Figure 2-22 shows typical raw data collected for a 12.5 μm x 177.8 μm microchannel (raw data for all of the experiments is included in Appendix A). The figure shows the differing results obtained with the three fluids, as well as the predicted pressure drop for each fluid. This type of data was used in the data reduction approaches described above to derive a friction factor for each fluid in each channel. The results are summarized in Table 2-7, which shows the predicted and measured values of C , as well as the ratio of values f^* . As the results in the table indicate, most of the experiments resulted in a friction factor within 10% of the predicted value.

12.7 μ m, 177.8 μ m, 2.48 cm

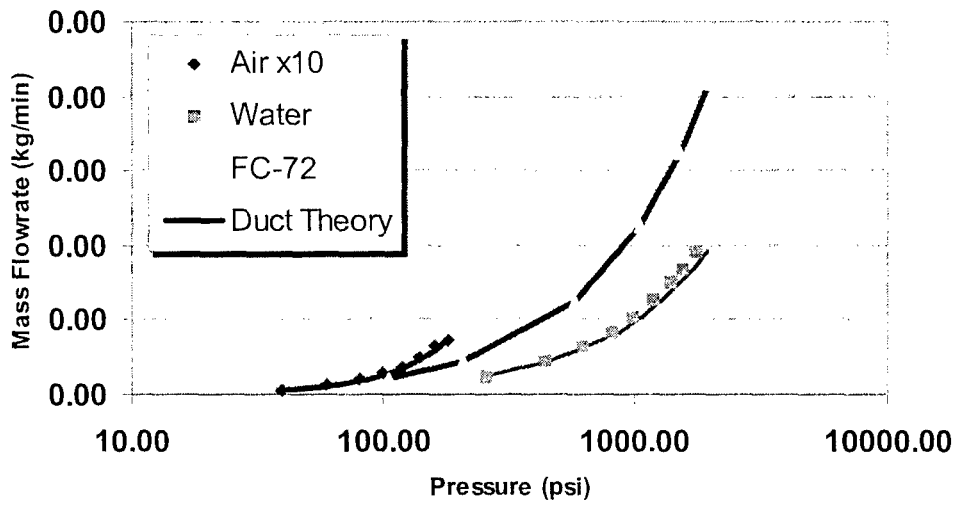


Figure 2-22. Typical Flow Data for 12.5 μ m

Table 2-7. Results of Smooth Channel Friction Factor Measurements

Channel	Fluid	C_{pred}	C_{meas}	f^*	Re_{Trans}
12.7 μ m x 95.32 μ m	Water	81.6	74.7	0.91	> 200
	FC-72		78.3	0.94	> 530
	Air		90.9	1.11	>450
12.5 μ m x 125 μ m	Water	87.6	95.7	1.09	> 140
	FC-72		97.8	1.12	> 500
	Air		91.2	1.04	>350
25.4 μ m x 139.7 μ m	Water	77.6	74.8	0.96	> 1930
	FC-72		56.5	0.73	~ 2300
	Air		77.0	0.99	>700
21.6 μ m x 270.5 μ m	Water	86.7	89.1	1.03	> 1200
	FC-72		85.8	0.99	> 2050
	Air		83.4	0.96	> 800
50 μ m x 250 μ m	Water	75.2	60.3	0.80	> 2500
	FC-72		Trans.	Trans.	Trans.
	Air		54.1	0.72	>1700
50 μ m x 500 μ m	Water	85.7	77.7	0.91	> 2160
	FC-72		Trans.	Trans.	Trans.
	Air		82.5	0.96	>2200

2.2.2 Transition Measurements

The transition Reynolds number was measured for all of the channels. The objective of these experiments was to determine if there were indications of laminar-turbulent transition occurring at Reynolds numbers below 1000 in microchannels, as has been reported elsewhere (Peng 1994a, 1994b). The friction factor is expected to decrease with Reynolds number during laminar flow, and then to rapidly increase as transition is encountered. Plots of the friction factor versus the Reynolds number, such as the typical plot shown in Figure 2-23, were derived by backing out the friction factor as described in Section 2.2.1, and finding the inflection point of the curve. The inflection point was then identified as the approximate point of transition. In the curve in Figure 2-23, the transition point would then be approximately $Re = 2300$.

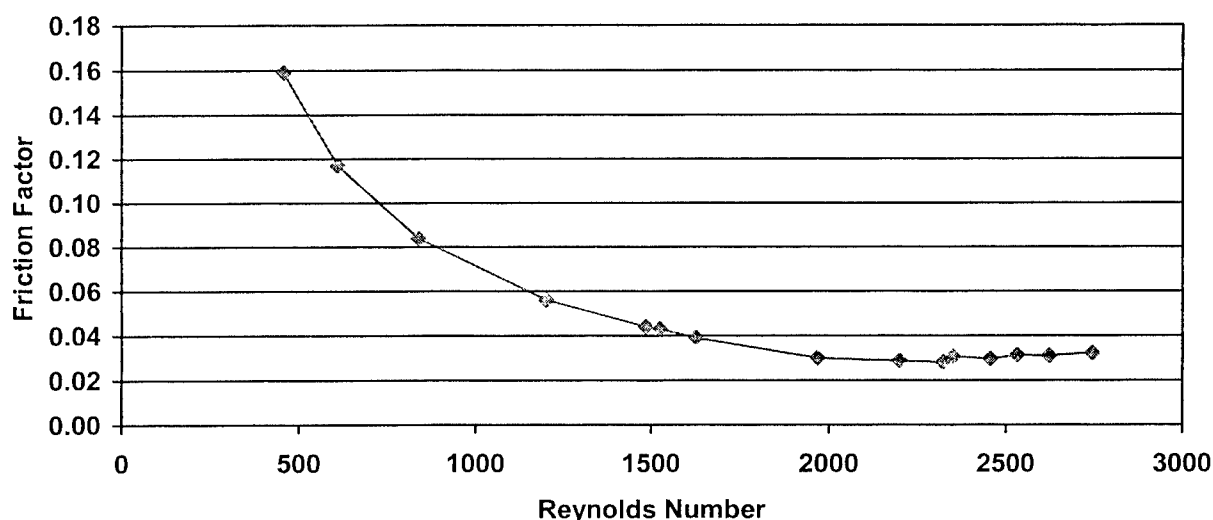
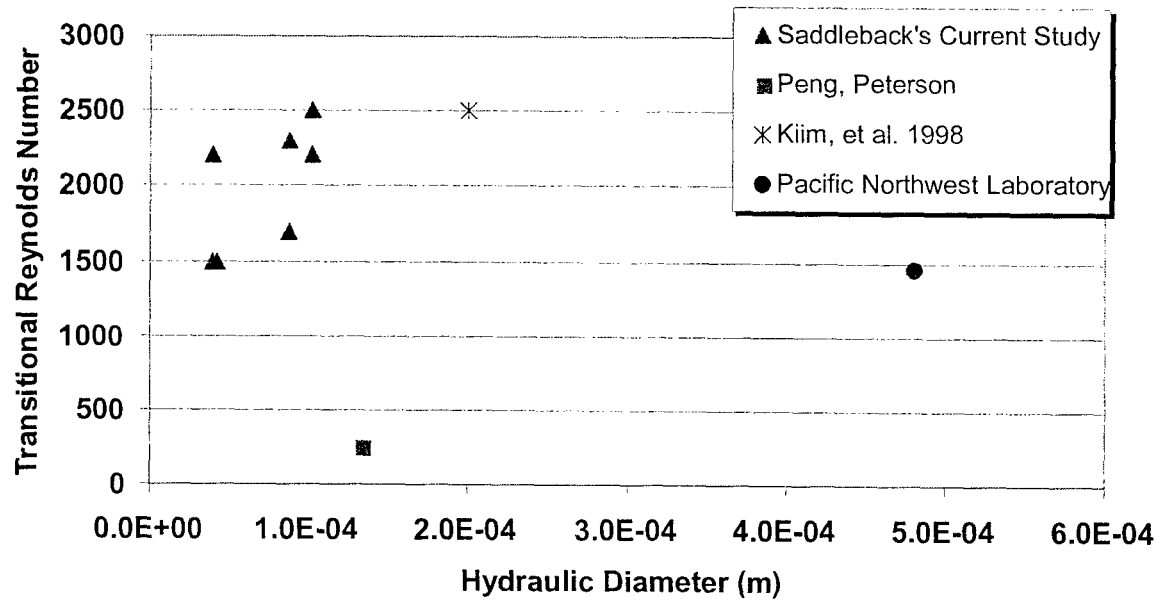


Figure 2-23. Typical Results of Data Reduction

The data reduced in this fashion is summarized in Figure 2-24. All of this data was derived from water and FC-72 experiments, since the N_2 experiments resulted in choking of the flow before the transition Reynolds number was reached. As the data show, all of the data ranged between transition Reynolds numbers of 1500 and 2500. The normal range for macroscopic ducts is typically considered to be 1800 – 2200, although the transition Reynolds number can be much higher if care is taken to reduce flow excitations.

From the appearance of the data in Figure 2-24, it is clear that there is no indication that transition occurs at unexpectedly low Reynolds numbers. As noted in the preceding paragraph, the center of the span of the measured transition Reynolds numbers is coincident with the center of the macroscopic Reynolds number band. The conclusion of the experiment was that there was insufficient justification to propose a new transition criterion for microchannel systems.

Figure 2-24. Summary of Transition



2.2.3 Roughness Measurements

The roughness experiments were designed to measure the effect of increasing roughness levels on the friction factor and transition Reynolds number of microchannels. In macro-ducts, roughness has been shown to have negligible influence on laminar flows. As mentioned in Section 1.2, however, Pfund et al. (1998) observed a significant increase in the laminar friction factor in roughened microchannels. If roughness effects were found to be significant in laminar flows at micro-scales, it

In fluid mechanics, roughness is based on a physical model of grains of sand glued to the inside of a smooth pipe. The diameter of the grains, ϵ , is divided by the hydraulic diameter of the smooth passage to produce the roughness ratio ϵ/D_H . Historical evidence has shown that the effect of moderate levels of roughness on laminar flow is simply to reduce the effective hydraulic diameter. Wu and Little (1984), however, found extremely large levels of roughness (20% - 30%) in microchannels could increase the friction factor by 30%. Further, recent experiments conducted at Pacific Northwest National Laboratory (Pfund et al., 1998) showed a 30 - 50% increase in laminar friction factor for a roughness ratio of 0.001 for high aspect ratio ducts with 508 μm widths.

A typical roughness level for a MEMS wafer might range from 0.1 - 2%. In an effort to provide a preliminary indication of whether roughness might be important, it was decided to fabricate specimens with nominal roughnesses of 1% and 10%. If no effect was observed, then it was felt that evaluations of smaller degrees of roughness would not be necessary. The roughened ducts were included in the same samples as the equivalent smooth ducts, so that direct comparisons could be made among the three ducts. It should be noted that the Asmooth@ ducts in the current investigation actually had roughnesses of 0.001 - 0.002.

Eight roughened specimens (corresponding to the 4 smooth channels described above) were fabricated, tested, and compared to the flow data for the smooth ducts. During the fabrication process the roughness was measured using a Tencor profilometer. Each of the samples contained a Asmooth@ duct and ducts of two roughnesses; all three were tested simultaneously in the test runs. The samples were tested with air, water and FC-72 (a low viscosity fluorocarbon fluid). The data for all of these tests is shown in Appendix A, which show the pressure drop vs. Reynolds number for each test. The 50 μm 4X data is missing for FC-72 and air since the channel became irreparably clogged after the water test.

Typical raw data for the 12.5 μm 10X channels tested with water is shown in Figure 2-25. Figure 2-26 shows the inferred normalized friction factors ($f_{\text{meas}}/f_{\text{pred}}$) for the three channels; the friction factor is seen to increase dramatically with increasing roughness, even at low Reynolds numbers. A comparison of the data for water and nitrogen is shown in Figure 2-26: both fluids show similar trends. Friction factor data for microchannels obtained from the literature is shown in Figure 2-28, and Phillips (1987) observed a similar increase in friction factor with roughness.

Figure 2-27 shows typical raw data where transition was observed. Figure 2-29 shows a summary of transition Reynolds numbers for all channels. As shown, the transition Reynolds number decreases with roughness. The flow is observed to begin transition at Reynolds numbers as low as 1000 for ducts with the highest roughness levels.

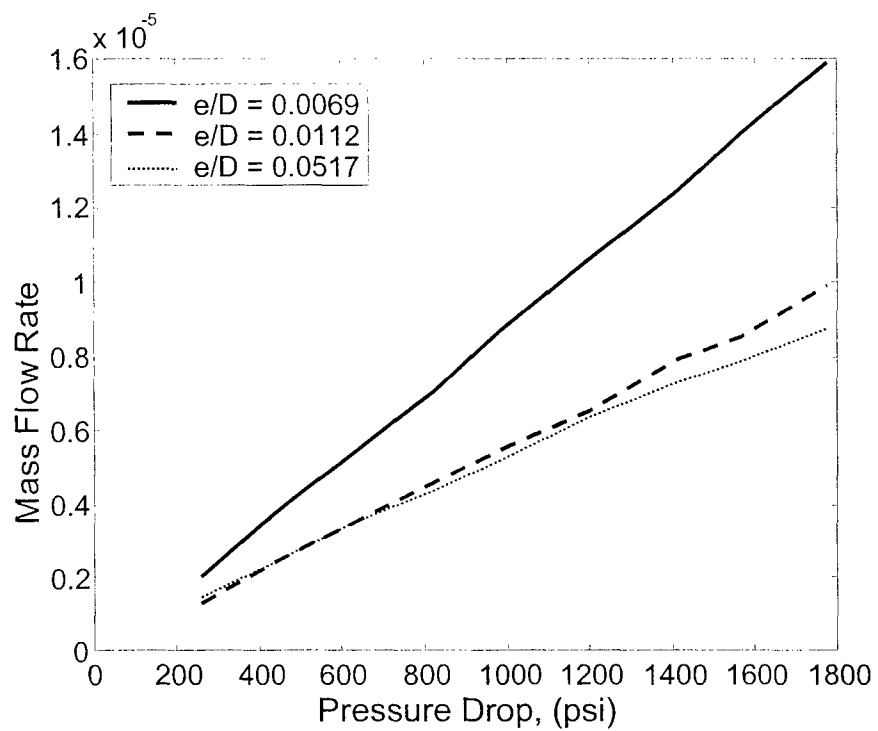


Figure 2-25 12.5 μm 10X channels tested with water

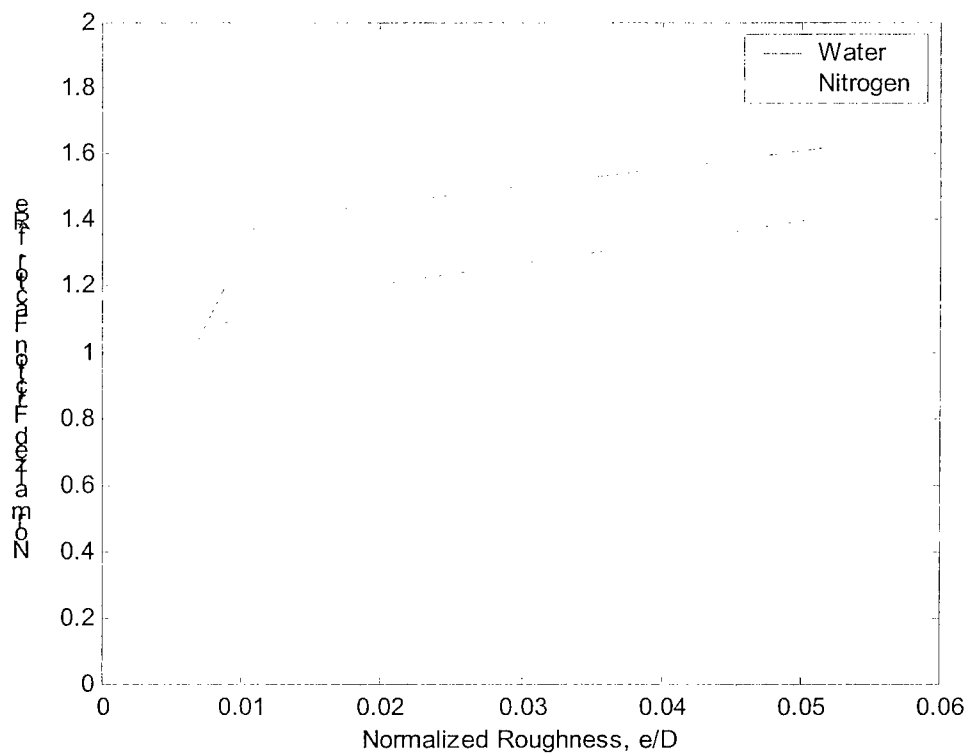


Figure 2-26. Roughness Effect on Friction Factor for Nitrogen and Water

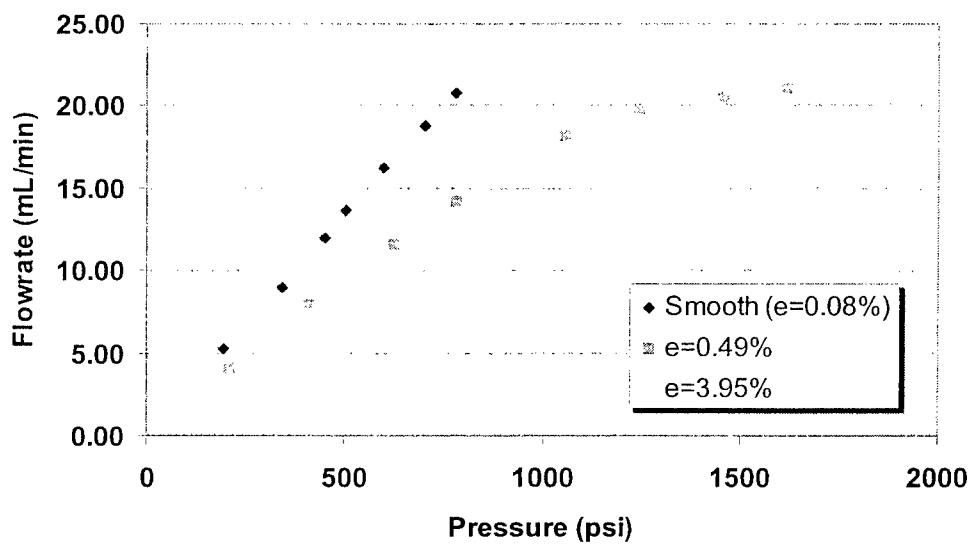


Figure2-27. Raw Data Showing Transition (50 μ m, 4X, Water)

Figure 2-28. Other Investigators Measurements of the Dependence of Friction Factor on Roughness

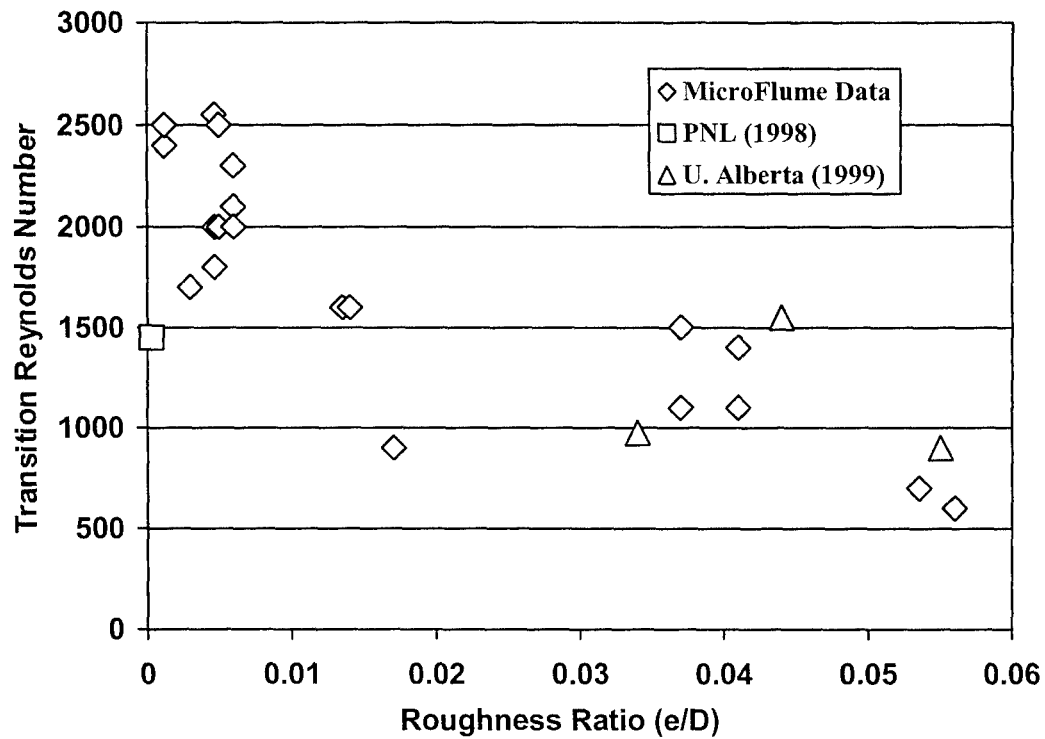
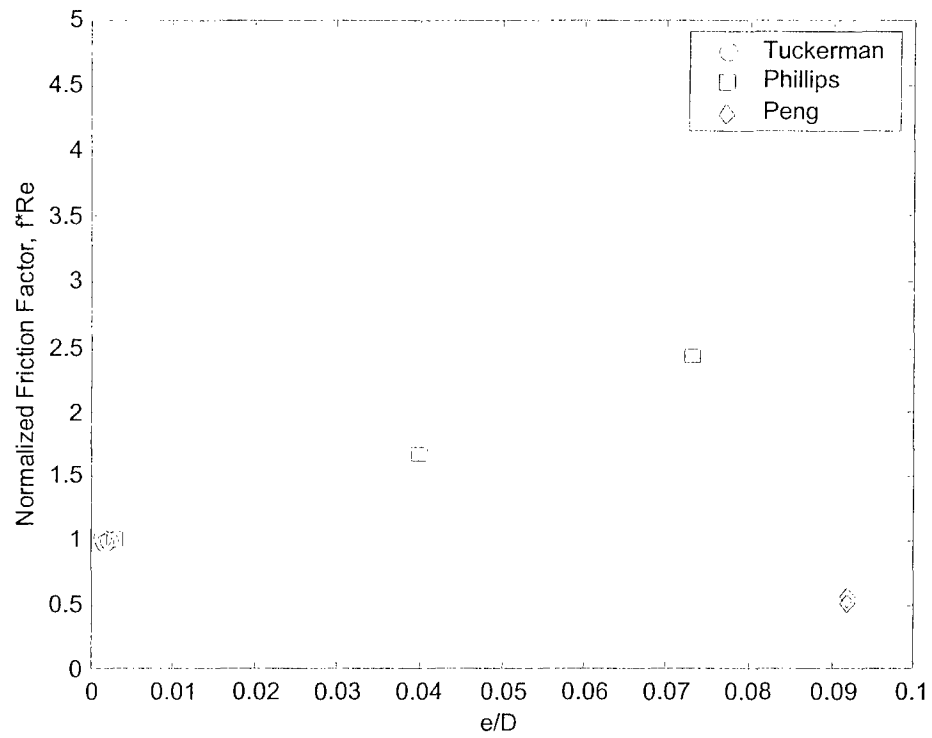


Figure 2-29 Summary of Transition Data



3.0 STRAIGHT MICROCHANNEL HEAT TRANSFER STUDIES

The sections below provide an overview of the experimental approach, a description of the heat exchange test sample fabrication, a description of the experimental setup, and a discussion of the results of the experiments.

3.1 Overview of the Experiment

The measurement of heat transfer coefficients for micro-fluidic systems is complicated by both the small scales and the very high heat transfer coefficients of the passages. The latter factor is problematic because it means that the temperature difference between channel walls and the bulk fluid is small, so that the effect of inaccuracy in temperature measurements is magnified. Microchannel coolers, for instance, can have as little as a 2 °C temperature difference between the heated surface and the inlet temperature at a heat flux of 100 W/cm². In addition, attempting to make a direct measurement of the wall temperature can distort the temperature field in the vicinity of the measurement device.

The “μHeat Exchange” test concept evolved in an effort to resolve the testing difficulties described above in an inexpensive way. In this test method, two channels are fabricated with what would be their heated surface joined together. In this configuration, heated fluid flows through one channel, while room temperature or refrigerated fluid flows through the opposing channel. In effect the pair of channels is operating in the fashion of a counterflow or parallel flow heat exchanger.

The parallel flow mode approximates a constant temperature boundary condition for the facing wall of each channel, while the counterflow mode gives a constant heat flux boundary condition. Figures 3-1 and 3-2 show temperature fields in a typical interface region between two microchannel passages. Figure 3-1 is a counterflow case, with hot fluid entering at the left above the displayed region and cold fluid entering at the lower right; the uniformly spaced isotherms are indicative of a constant heat flux along the interface. When the fluids are introduced to the passages on the same side, as in Figure 3-2, there is a horizontal isotherm across the middle of the interface region, indicating a constant temperature boundary condition.

The heat transfer effectiveness can be derived for this simple heat exchanger configuration from measurements of the fluid inlet and outlet temperatures and the fluid mass flow rates for both channels. The effectiveness can then be used to derive a Nusselt number or heat transfer coefficient for the internal passages. In cases where the fluid/wall temperature differences are large, some accommodation must be made for the affect on fluid properties and their subsequent affect on velocity profiles in the two channels.

Removing the necessity for making temperature measurements in the “faceplate” region (i.e., the region between the heat source and the channel itself) allows measurements of heat transfer properties without perturbing the temperature field in the walls around the channel. To improve the data, many channel pairs can be stacked so that the effects of conduction into the test fixture (edge effects) can be minimized. Finally, the peak heat flux is limited only by the heat transfer capabilities of the opposing channels.

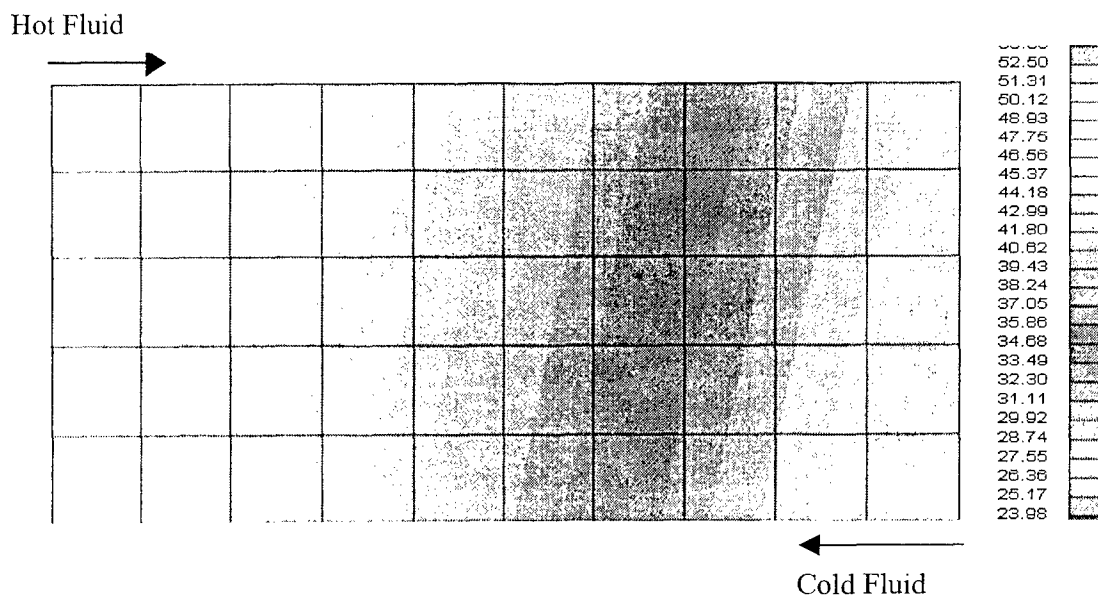


Figure 3-1. Counterflow Provides Constant Heat Flux Boundary Condition

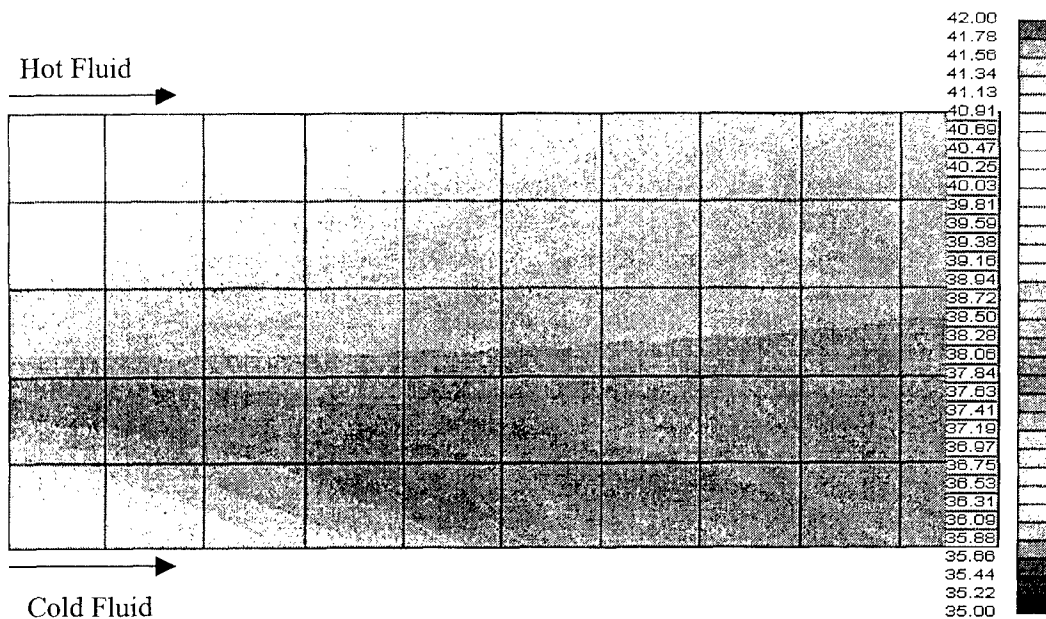


Figure 3-2. Parallel Flow Provides Constant Temperature Boundary Condition

3.2 μ Heat Exchange Test Samples

The heat transfer specimens involved two configurations, shown in Figures 3-3 and 3-4, a parallel orientation and a perpendicular orientation. The two configurations differ mainly in the aspect ratio – the parallel orientation has the long dimension of the microchannels oriented parallel to the heat flux vector, while the perpendicular orientation has the short dimension of the microchannels oriented parallel to the heat flux vector. Using the combination of the two orientations allows measurement of laminar Nusselt numbers over an aspect ratio range of 0.1 to 10.

Four samples of each orientation were fabricated: 25 μ m ducts of 4X and 10X aspect ratios, and 50 μ m ducts of 4X and 10X aspect ratios. The samples consisted of arrays of channels, so that the differences among channels can be averaged out. In the case of the parallel orientation samples, the samples ranged from 3 – 4 mm thick, resulting in more than 30 channels for the 50 μ m ducts, and more than 300 channels for the 25 μ m ducts. The perpendicular orientation samples had between 50 and 200 channels, depending upon the channel height (which lies in the plane of the foil).

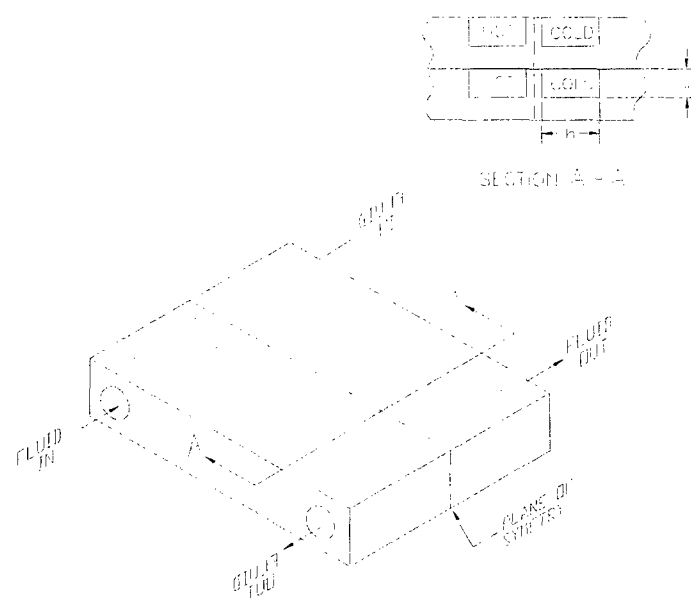
Photos of the samples during fabrication are provided in Figures 3-5 – 3-7; the photos are roughly actual size. The foils are actually composed of Glidcop, a dispersion-strengthened copper alloy, but have been plated with nickel prior to diffusion bonding. This gives the pre-bond foils a steel-like appearance. Figure 3-5 shows an etched parallel foil, while Figure 3-6 shows an etched perpendicular channel foil. Each foil contains duct patterns etched halfway through the thickness. As shown in Figure 3-5, which happens to be a 25 μ m x 250 μ m test sample, there are eight heat exchanger layers in a single foil, with each one containing five pairs of channels. The 50 μ m wide parallel specimens had a single, uninterrupted pairs of channels, since the pressure drop for a given flow rate was lower in the larger channels.

Figure 3-7 shows a set of the perpendicular 25 μ m foils being stacked prior to diffusion bonding. The foils are aligned to within 25 μ m by the steel alignment pins at the left and right of the piece. Eight heat exchange samples were manufactured simultaneously during this process; the pieces were subsequently cut apart and mounted with quarter-inch inlet and outlet supply tubes. A completed test sample is shown at roughly actual size in Figure 3-8.

Figure 3-9 shows a perpendicular test specimen (actual size) with 50 μ m x 500 μ m channels after diffusion bonding and sectioning. In both Figure 3-8 and Figure 3-9 one can see that the diffusion of the nickel into the Glidcop during the bond run has restored the original copper color of the part. The perpendicular specimens were designed to be mounted to Delrin manifolds, so no tubes are attached to the specimen.

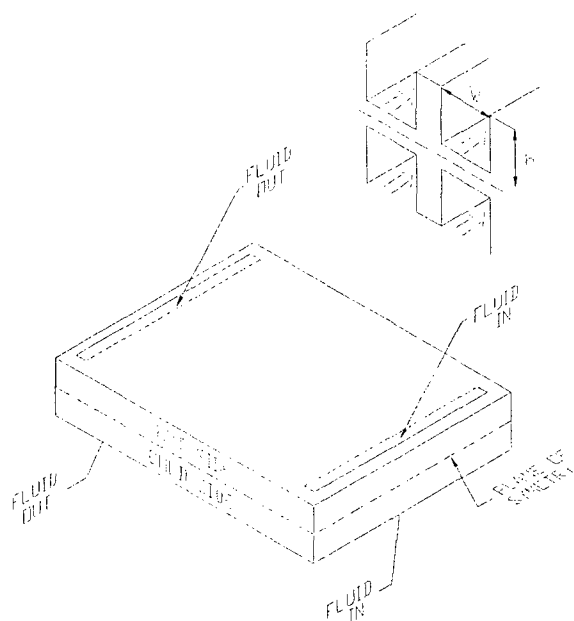
The diffusion bonding process encountered problems, resulting in cross-talk between the cold and hot passages in the parallel specimens and leakage at the periphery in the perpendicular specimens. After some effort it was discovered that the boron nitride release coating (visible on the bonding fixtures in Figure 3-7) was releasing organics during the bonding cycle. The unique design of the test specimens, which had several open ports, allowed the organics to enter the parts and coat the bonding surfaces between foils. This proved to effectively inhibit diffusion bonding

on a somewhat random basis in the parts. The test samples were still considered usable, however, and so they were submitted for testing.



HEAD-TO-HEAD STRAIGHT MICROCHANNEL TEST ARTICLES			
ROUGHNESS	DIMENSIONS (μm)		
	WIDTH	HEIGHT	LENGTH
AS ETCHED	25	100	1 cm
	25	250	1 cm
	50	200	5 cm
	50	500	5 cm
AS ROLLED	25	100	1 cm
	25	250	1 cm
	50	200	5 cm
	50	500	5 cm

Figure 3-3. Parallel Orientation μ Heat Exchange Schematic and Candidate Dimensions



HEAD-TO-HEAD STRAIGHT MICROCHANNEL TEST ARTICLES			
ROUGHNESS	DIMENSIONS (μm)		
	WIDTH	HEIGHT	LENGTH
AS ETCHED	100	25	1 cm
	250	25	1 cm
	200	50	5 cm
	500	50	5 cm
AS ROLLED	100	25	1 cm
	250	25	1 cm
	200	50	5 cm
	500	50	5 cm

Figure 3-4. Perpendicular Orientation μ Heat Exchange Schematic and Candidate Dimensions

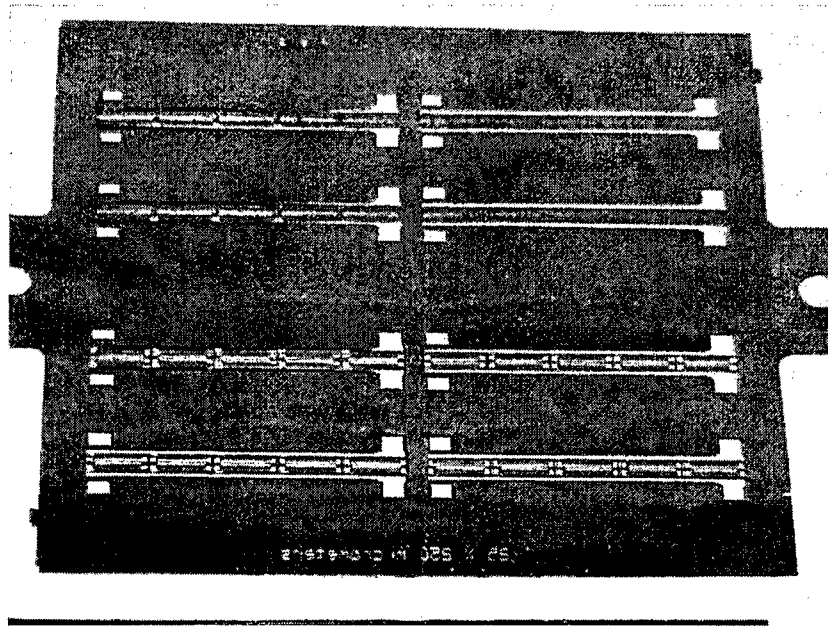


Figure 3-5. Typical Foil Used in Fabrication of Perpendicular μ Heat Exchange Test Specimens

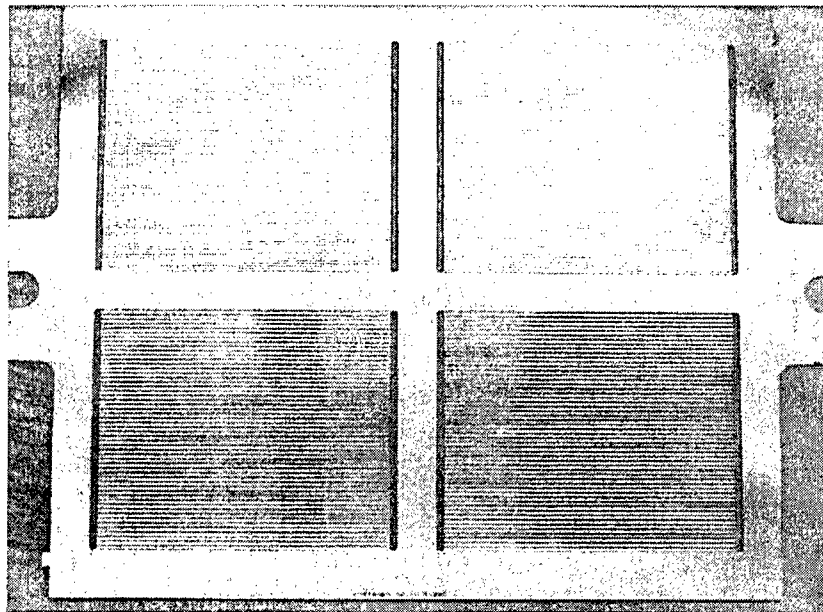


Figure 3-6. Typical Foil Used in Fabrication of Parallel μ Heat Exchange Specimens

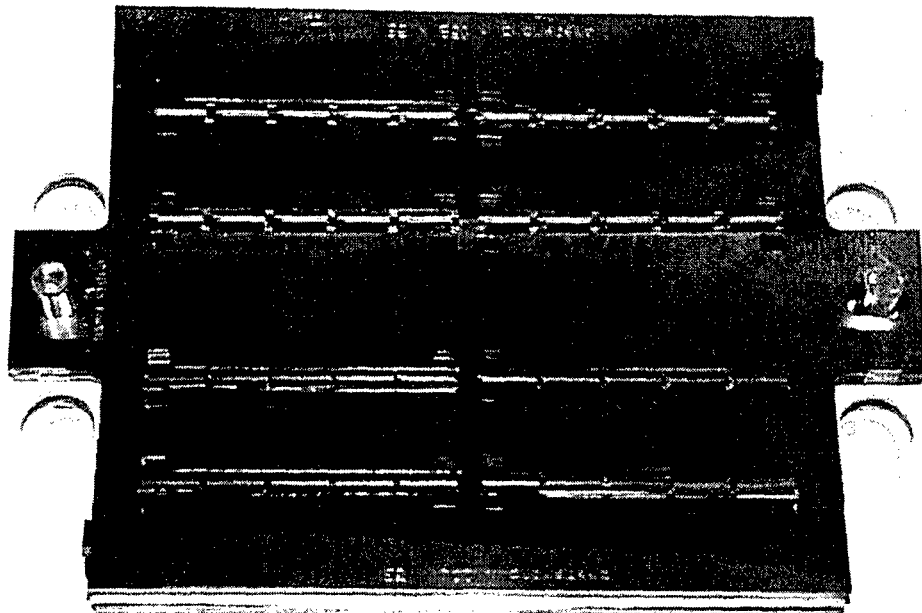


Figure 3-7. Perpendicular μ Heat Exchange Specimens During Stacking

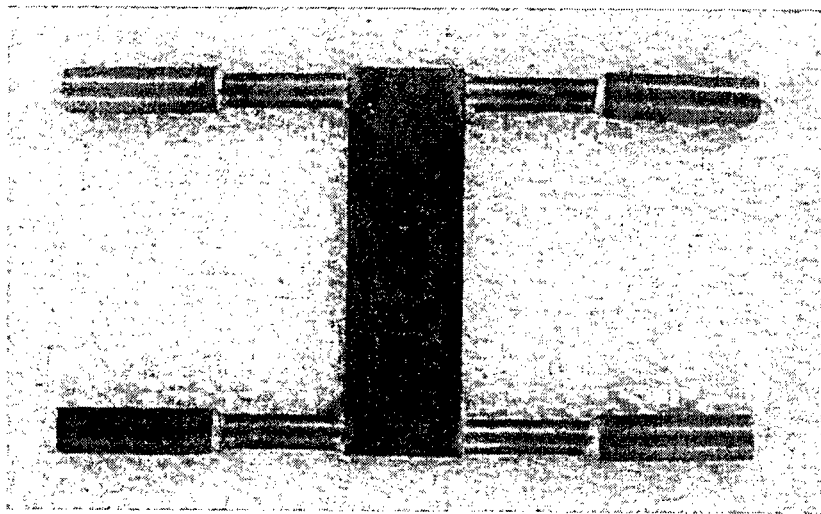


Figure 3-8. Perpendicular μ Heat Exchange Specimen After Diffusion Bonding, Machining, and Mounting of Inlet and Outlet Tubes

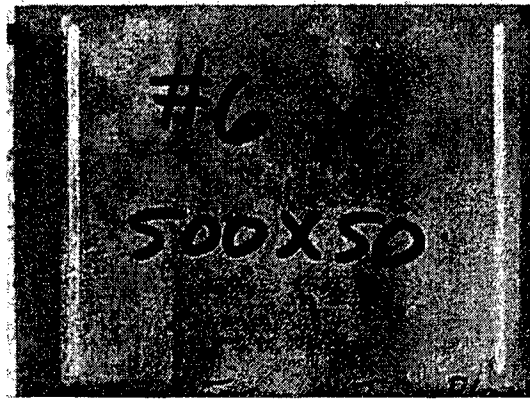


Figure 3-9. Parallel μ Heat Exchange Specimen After Diffusion Bonding and Machining

3.2 Description of the Experiment

The test setup for the experiment included 2 flow meters, 2 pressure gauges, and 4 thermocouples. Photographs of the test are presented in Figures 3-10 and 3-11. As shown in the photographs, each inlet line has a needle valve, a 7 μ m filter, a flow meter, and a pressure transducer. The needle valves were used to balance the flow rate between the hot and cold sides. Thermocouples are placed upstream and downstream on both lines.

The accuracy of the heat transfer tests is dependent upon the flow rate and thermocouple measurement accuracies. The differential thermocouple measurements have accuracies of 0.1 °C over a range of typically 10 - 20 °C. The flow meters were 0 – 2 L/min 101-7T Flo-Sen models from McMillan Company (Georgetown, TX), and the pressure transducers were 0 – 60 psig (PX181-060G5V models from OMEGA). The flow meters were documented as having accuracies of 3%, but variations of 20% were found over the course of months of testing. For this reason the flow meters were calibrated during each test, with the expectation that the slowly varying error in the meter would remain constant during a test. An RMS total of all of the error sources gives a little less than 5% error in evaluation of the thermal resistance of the sample.

The fluid supplies for the water and PAO were provided by conventional 10 gallon water heaters. The water heaters were able to heat the fluids up to 65°C, and were able to operate at pressures up to 150 psi. For the PAO two additional tanks were used to collect the outlet flow from each fluid circuit. This aided in keeping the PAO contained during the experiments. The water was simply collected in jugs and the heaters were refilled as necessary. The air tests used nitrogen gas bottles as fluid supplies. The hot side was run through a copper coil in a small oven to elevate the temperature. After passing through the test sample, the nitrogen was vented to atmosphere.

Tests were conducted by first establishing the cold-side flow, and then bringing the hot-side flow up to the same flow rate as the cold-side. Data was collected by a data acquisition board and viewed in real time using LabView. The test operator would wait for the temperatures to steady out at a given test condition, and then would increase the flow rates to obtain the next desired condition.

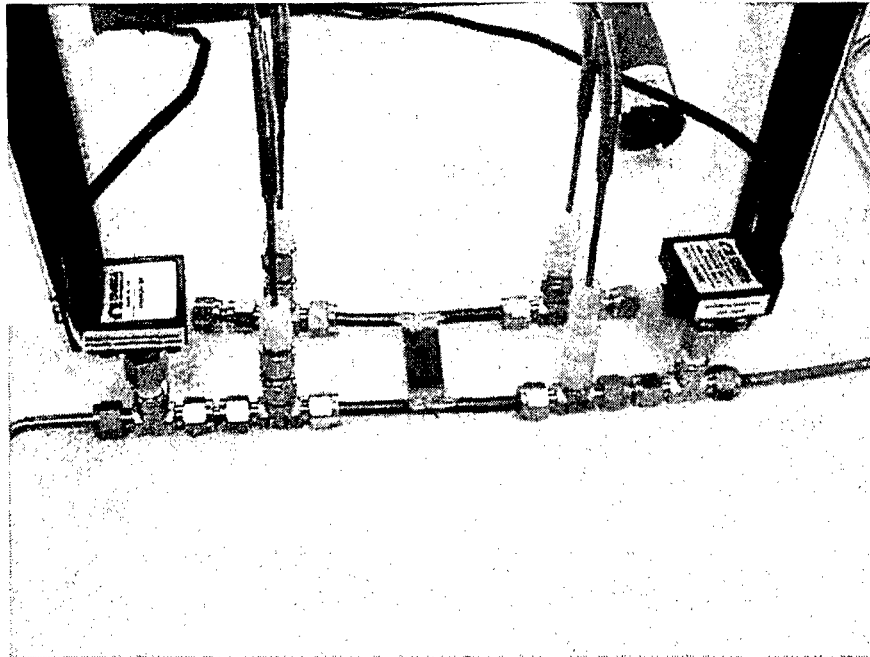


Figure 3-10. Oblique View of μ Heat Exchange Test

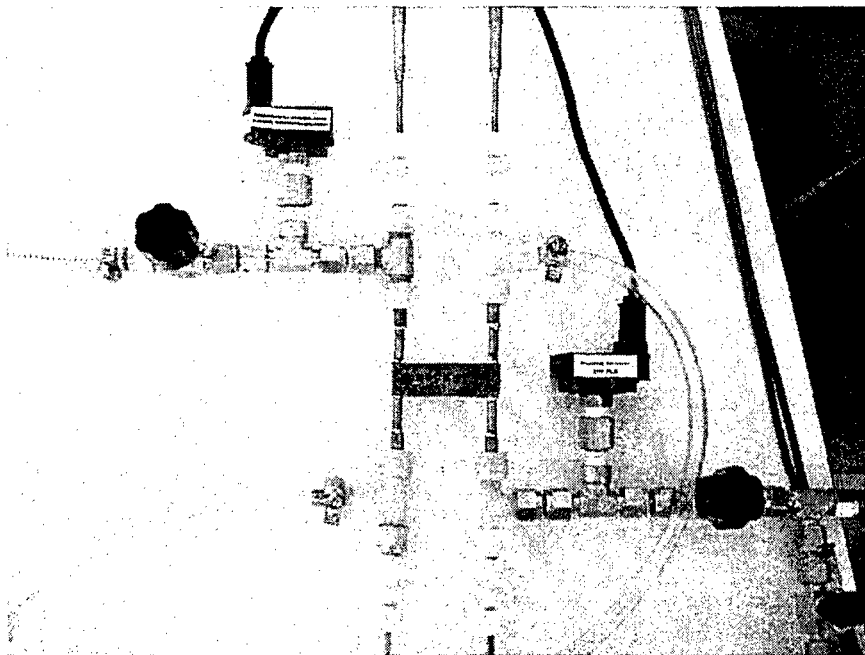


Figure 3-11. Top View of μ Heat Exchange Test

3.4 Experimental Results

A heat transfer test series was conducted on four perpendicular μ Heat Exchange specimens. The specimens were tested with water and air in both the parallel flow and counterflow configurations. The counterflow tests encountered problems due to cross-talk, so parallel data is considered more reliable. This is because the pressure gradient across the interface between the hot and cold channels is likely to be small. Due to re-scoping of the program, the PAO tests were not conducted on the perpendicular specimens, and none of the parallel specimens were tested.

Typical temperature data from a water test is shown in Figure 3-12. As shown, even when the temperatures are still increasing, the system appears to be operating in a quasi-steady state mode. Energy balances and measured effectivenesses for the data are shown in Figure 3-13. The effectiveness is defined as the temperature rise of the cold fluid divided by the difference in temperature between the two inlets. The cold side was selected because it is less susceptible to heat losses to the environment, and so generally provides a more realistic measure of thermal performance than the hot side data. Similar data is shown in Figures 3-14 and 3-15 for a nitrogen test. Both the nitrogen and water tests show reasonable energy balances and effectivenesses close to 0.5 (the effectiveness limit for parallel flow configurations).

The results of the counterflow tests are summarized in Figure 3-16, which shows the ratio of the measured to predicted cold side coolant temperature rise versus the average Reynolds number of the hot and cold sides. As shown, the test data were all within 35% of the predicted values, and in some cases were extremely close to the predicted values. Two sources of concern were the lower values for the 25 μ m channels, and the increasing trend with Reynolds number for the 25 μ m specimens in the counterflow configuration. This might be symptomatic of an increasing leakage problem as the inlet pressures increase.

Figure 3-17 shows a summary of the data collected for the parallel flow tests. As expected, the data are better behaved, even for the 25 μ m specimens. The 50 μ m data is within 5% of prediction, while the 25 μ m data is about 25% lower than predicted. The increasing trend with Reynolds number, however, is no longer observed in the 25 μ m data, supporting the notion that the counterflow results were affected by cross-talk between the passages.

These preliminary experiments demonstrated that a large amount of data could be accumulated at a relatively low cost, and suggested that if the sample fabrication difficulties were overcome, the test results could be reliable and accurate. The diffusion bonding issues which arose during the sample fabrication have since been resolved, making further heat transfer studies possible.

Figure 3-12. Typical Raw Temperature Data for Water (50 μm x 500 μm , Parallel Flow)

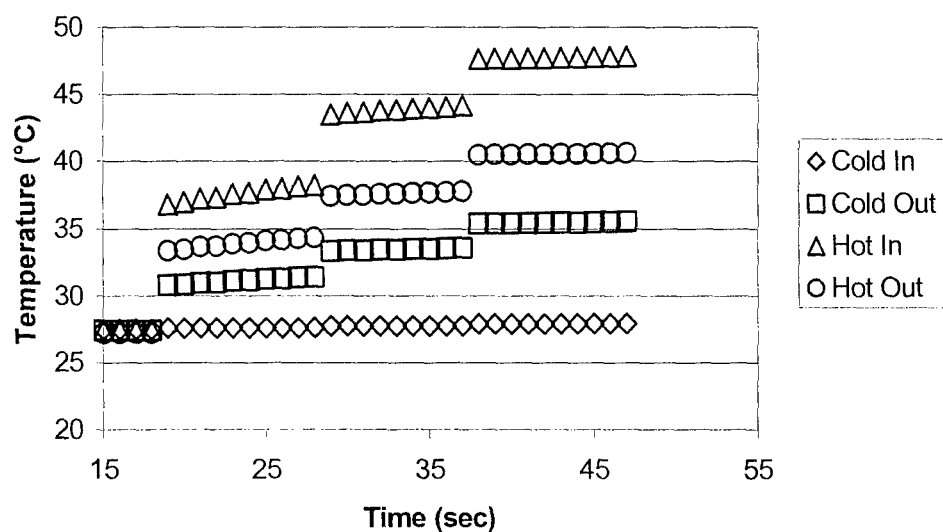


Figure 3-13. Energy Balance and Effectiveness for Water (50 μm x 500 μm , Parallel Flow)

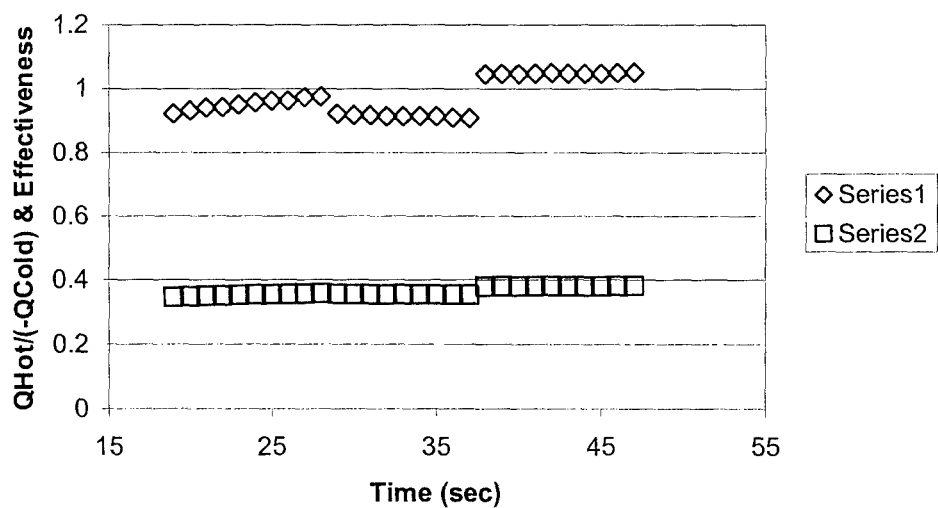


Figure 3-14. Raw Temperature Data for Air (50 μm x 500 μm Parallel Flow)

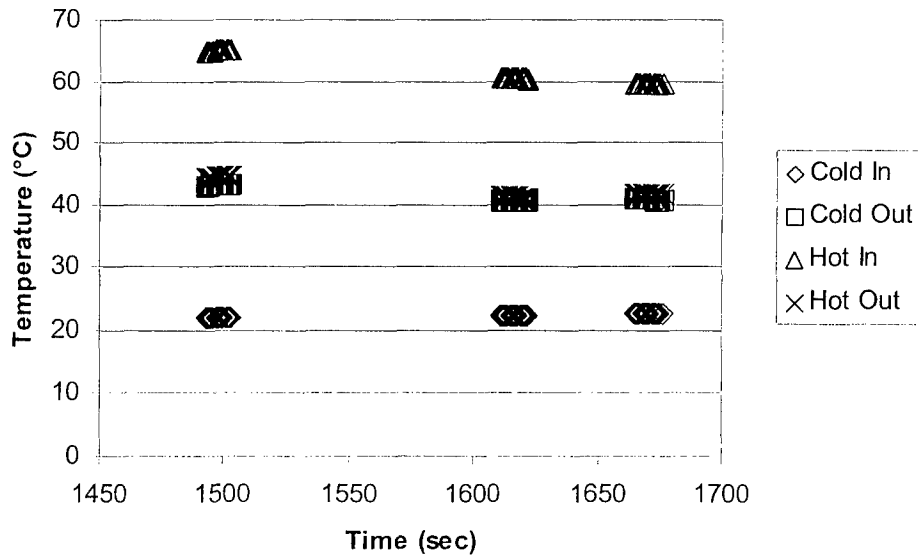
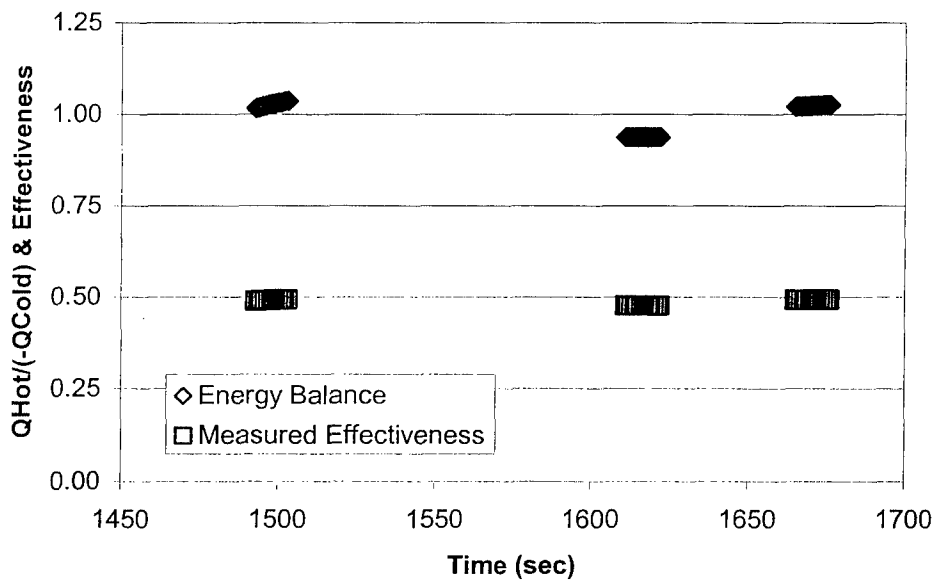


Figure 3-15 Energy Balance and Measured Effectiveness for Air (50 μm x 500 μm Parallel Flow)



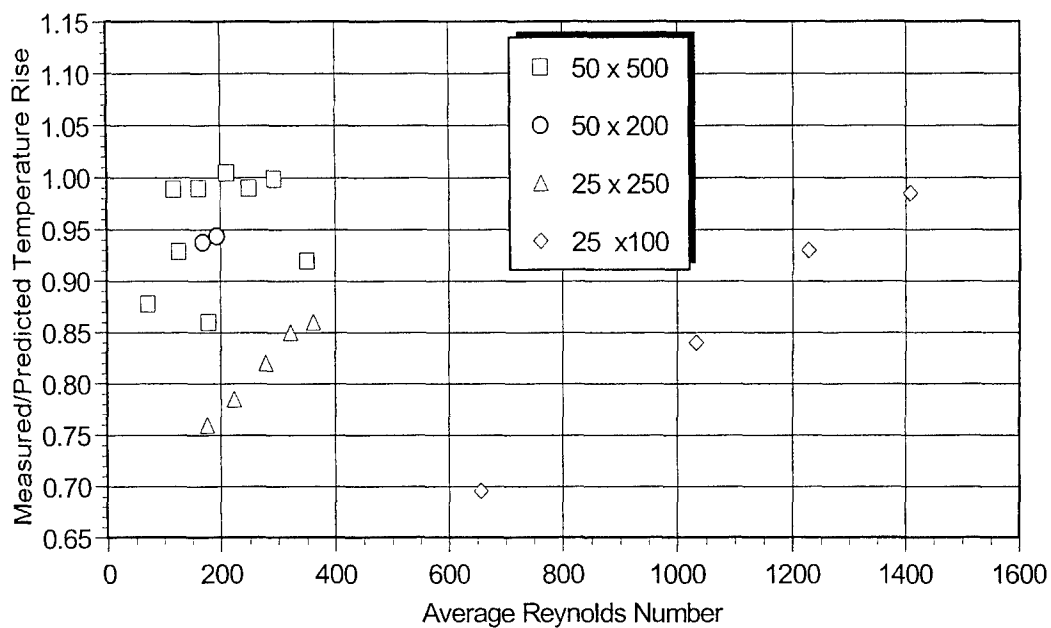


Figure 3-16. Results of Counterflow μ Heat Exchange Experiments

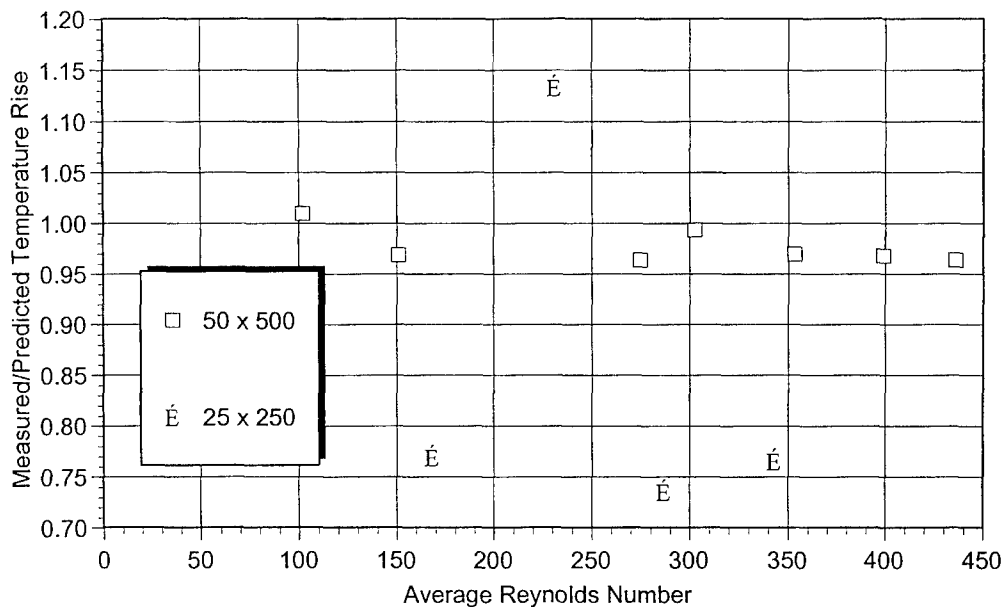


Figure 3-17. Results of Parallel Flow μ Heat Exchange Experiments

4.0 Minor Loss Coefficient Measurements

4.1 Minor Loss Coefficients of Bends

Bends are a common feature of macro- and micro- flow systems, and so the characterization of their flow behavior is important to MEMS-class fluid designs. The behavior is typically characterized in terms of an excess pressure drop - that is, the pressure drop contribution for the bend is specified as that exceeding the pressure drop for a straight channel of equivalent length. This contribution is divided by the dynamic pressure in the channel, yielding a minor loss coefficient, K_{Bend} .

The equation for the total pressure drop of an incompressible flow in a constant area duct with a bend is commonly written in the form:

$$\Delta P = 0.5 \rho V^2 \left(\frac{f L}{D} + K_{Inlet} + K_{Outlet} + K_{Bend} \right)$$

where f is the friction factor, L is the length of the channel (along the centerline, including the bend), D is the hydraulic diameter, and the minor loss coefficients of the inlet and exit of the channel are represented as K_{Inlet} and K_{Outlet} , respectively. The inlet loss coefficient can be considered to be comprised of two parts: an excess pressure drop due to flow development in the inlet region, and any irreversible flow losses due to the manifold-entrance flow geometry.

Bends in rectangular ducts are characterized by the establishment vortex pairs in the flowfield and separation regions at the outer radius of the bend and along the inside wall just after the bend. The influence of these separation regions on the flow is a function of the bend angle, Reynolds number, aspect ratio of the duct, and the sharpness of the bend. The sharpness is defined as R/b , where R is the radius of the bend, and b is the width of the channel in the bending plane.

In order to assess the influence of all four of the relevant parameters, channels of 4X, 6X, and 8X aspect ratios, 45° and 90° bend angles, and sharpness ratios of 1, 3, 5 and 10 were fabricated and tested over a Reynolds range from 50 to > 1000. The tests were conducted using the same methodology as for the straight channels, with the exception that NoShok gauges were substituted for the OMEGA gauges. A NoShok 640.500.2.12.8.10 with a range of 0 – 500 psi and an accuracy of 0.05% was used for data below 500 psi, and a NoShok 640.3000.2.12.8.10 with a range of 0 – 3000 psi and an accuracy of 0.025% was used for data above 500 psi.

The raw data collected during the testing is included in the Appendix. The developing and fully developed flow pressure losses predicted using standard straight rectangular channel correlations were calculated and subtracted from the measured data. The remainder was divided by the dynamic pressure to yield the minor loss coefficient for the

bend. The results of this data reduction process are shown in Figures 4-1 through 4-18. To obtain the minor loss coefficient from the reduced data, the minor loss coefficients associated with irreversible pressure losses at the entrance and exit must be subtracted from the aggregate minor loss coefficient shown.

As the figures show, the minor loss coefficient typically descends rapidly from a very high value at low Reynolds number, stabilizing at relatively constant values by $Re = 900$. This is qualitatively consistent with expectations - Blevins (1984), for example, shows the minor loss coefficients for both 45° and 90° bend dropping from about 350 at $Re = 10$ to about 1 - 2 at $Re = 500$, where it levels out.

Figures 4-19 and 4-20 show the sensitivity of the average laminar minor loss coefficient to the sharpness of the bend in the duct. In this case the data between $Re = 500$ and $Re = 1000$ were averaged to give an average K_{Bend} . As the data shows, the bend sharpness does not provide a strong influence on the pressure losses in this Reynolds number range. A comparison of the minor loss coefficients for 45° and 90° bends is provided in Figures 4-21 and 4-22. As the figures show, the 90° Bends tend to have a higher loss than the 45° bends. Figures 4-23 and 4-24 show that the duct aspect ratio has little influence on the minor loss coefficient.

Figure 4-1. 45° Bend Data for 25 μm x 128 μm Channel: Water

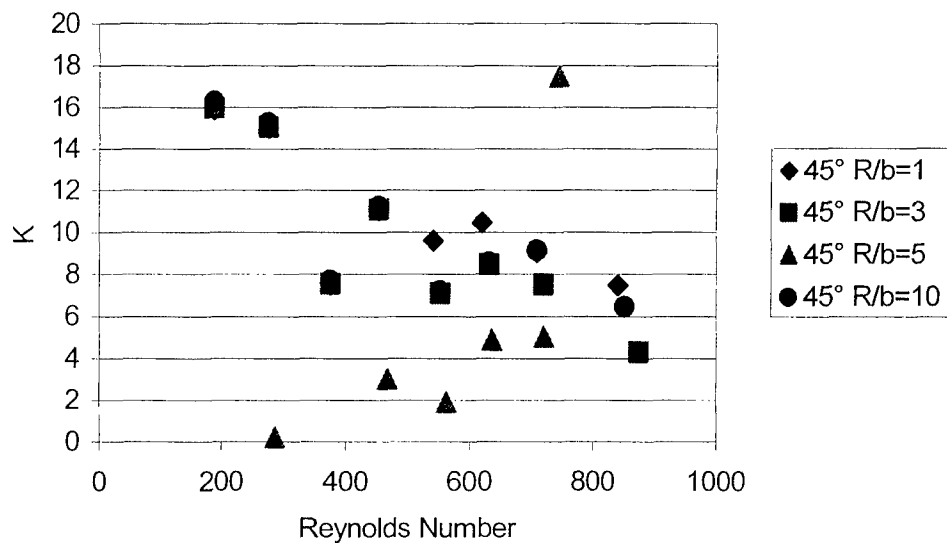


Figure 4-2. 90° Bend Data for 25 μm x 128 μm Channel: Water

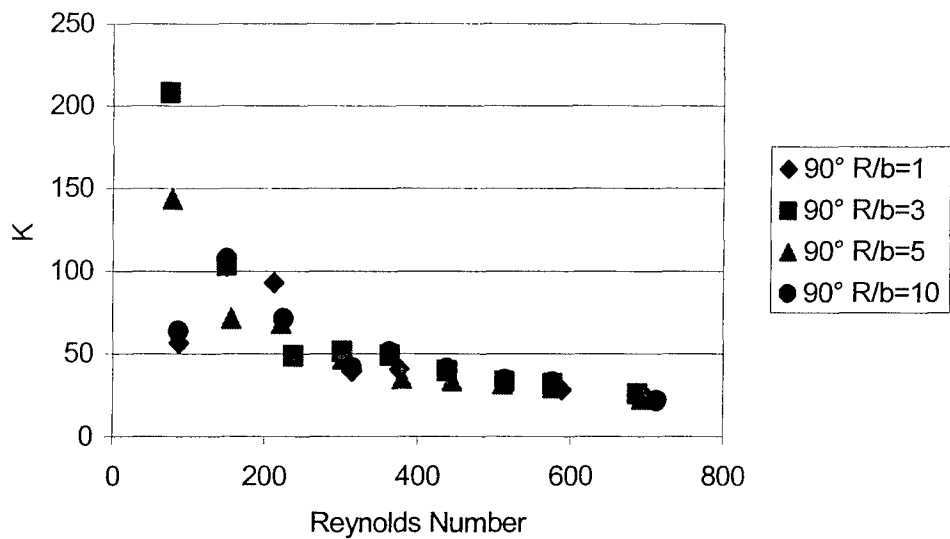


Figure 4-3. 45° Bend Data for 25 μm x 149 μm Channel:
Comparison of FC-72 and Water Data

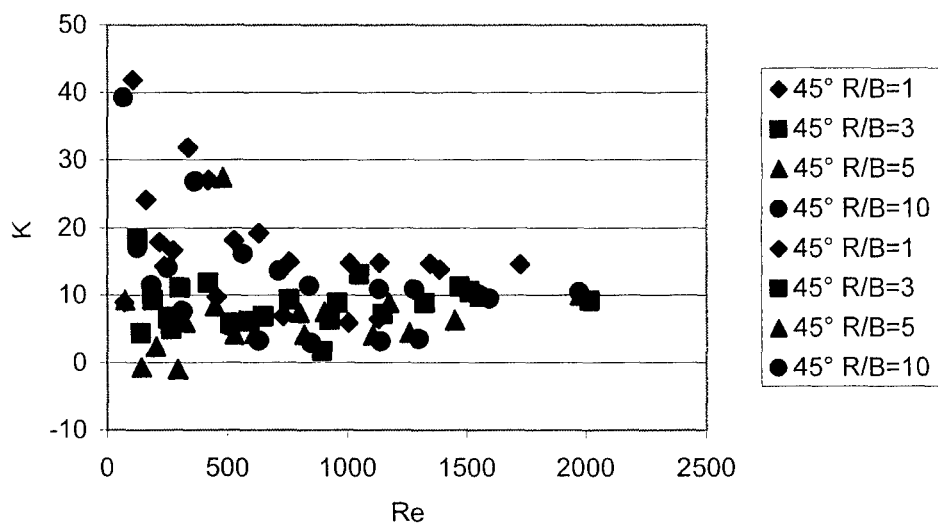


Figure 4-4. 90° Bend Data for 25 μm x 149 μm Channel:
Comparison of FC-72 and Water Data

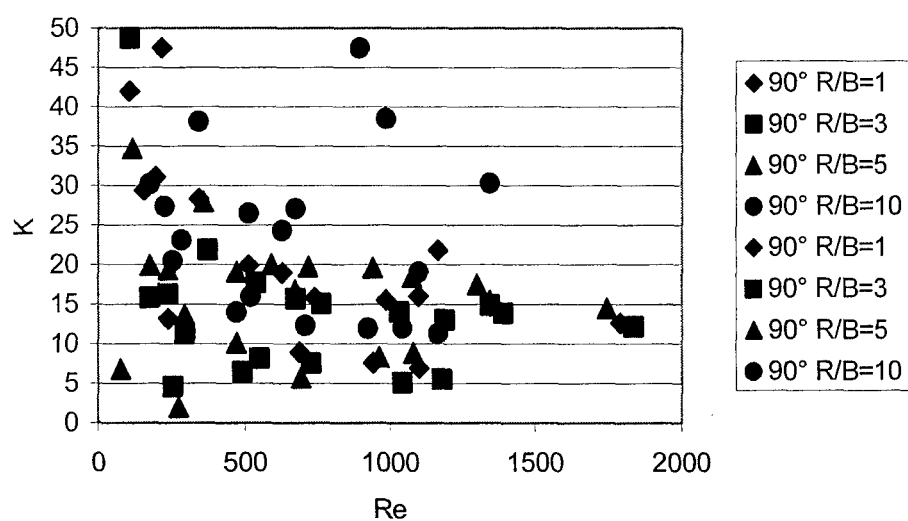


Figure 4-5. 45°Bend Data for 23 μm x 178 μm Channel: Water

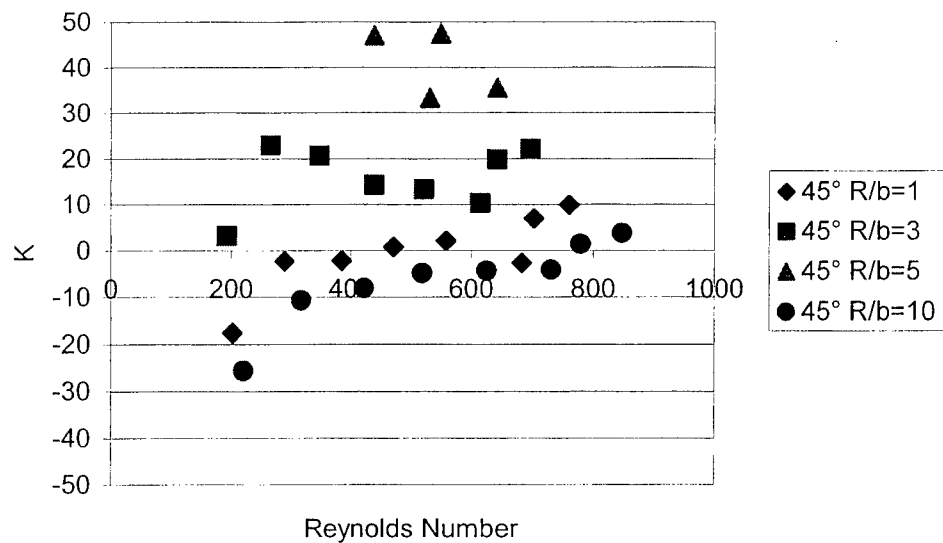


Figure 4-X. 90°Bend Data for 23 μm x 178 μm Channel: Water

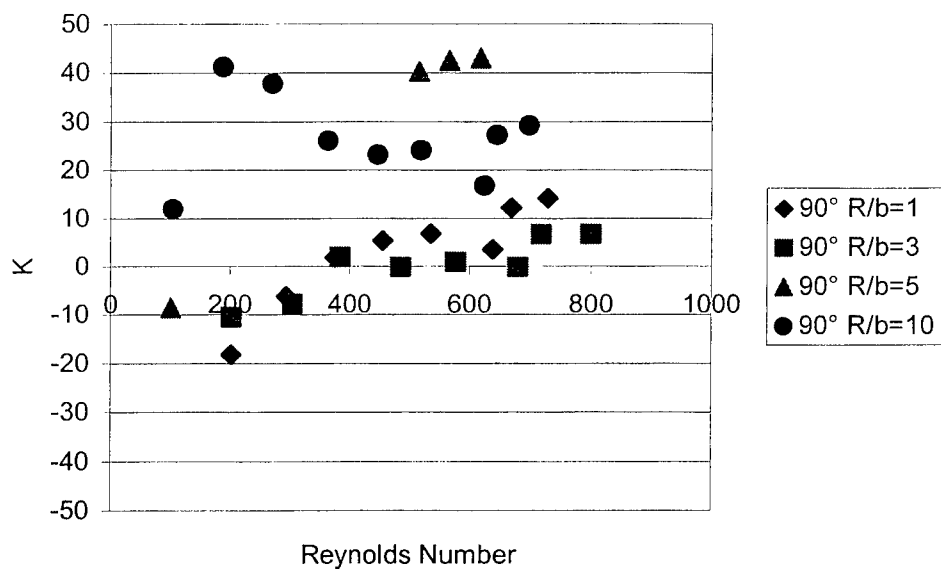


Figure 4-7. 45° Bend Data, 23 μm x 172 μm Channels, Water
Versus FC-72

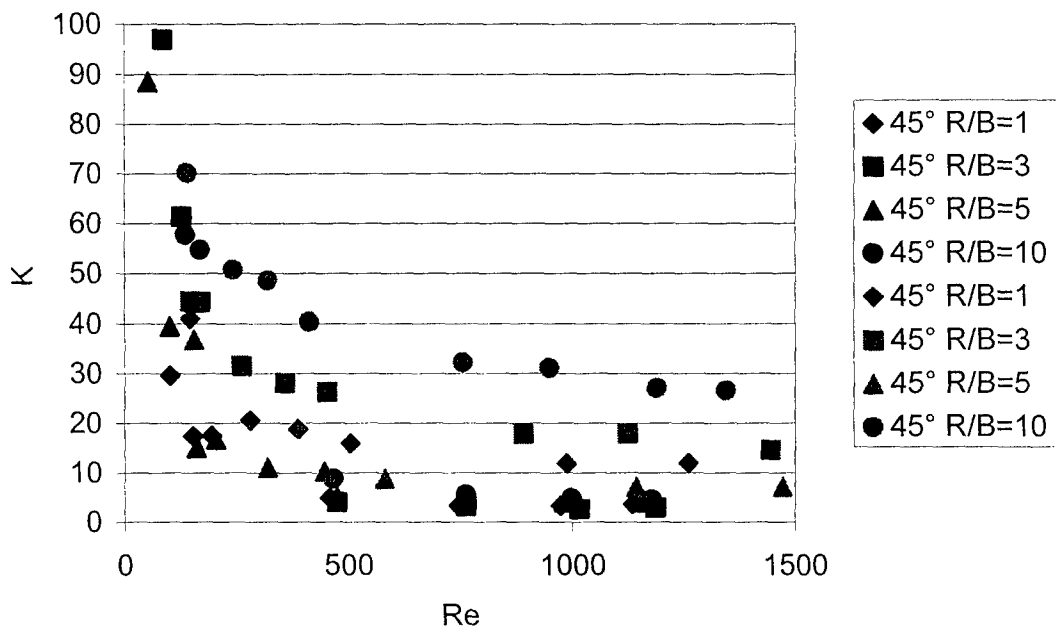


Figure 4-8. 90° Bend Data, 23 μm x 172 μm Channels,, Water
Versus FC-72

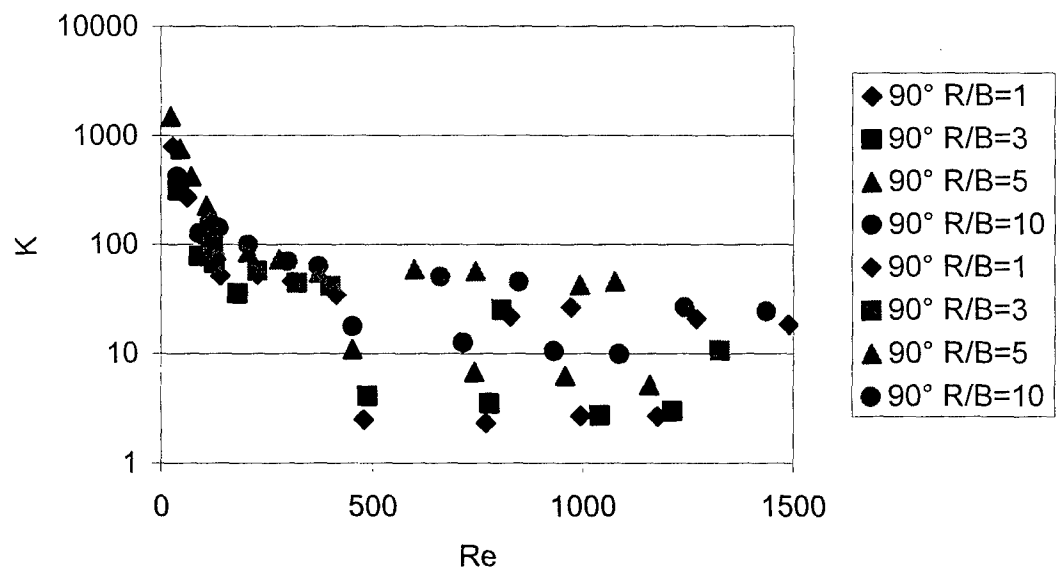


Figure 4-9. 45°Bend Data for 27 μm x 185 μm Channel: Water

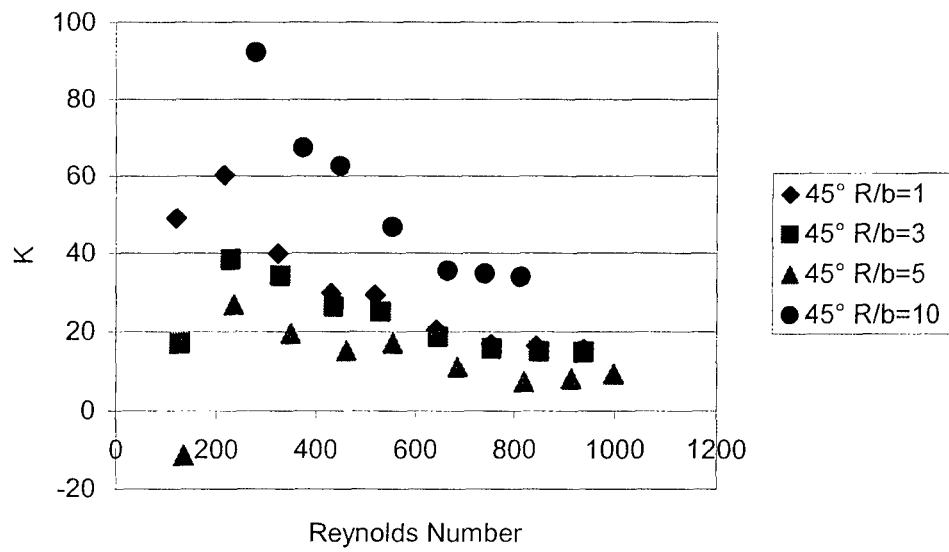


Figure 4-10. 90°Bend Data for 27 μm x 185 μm Channel: Water

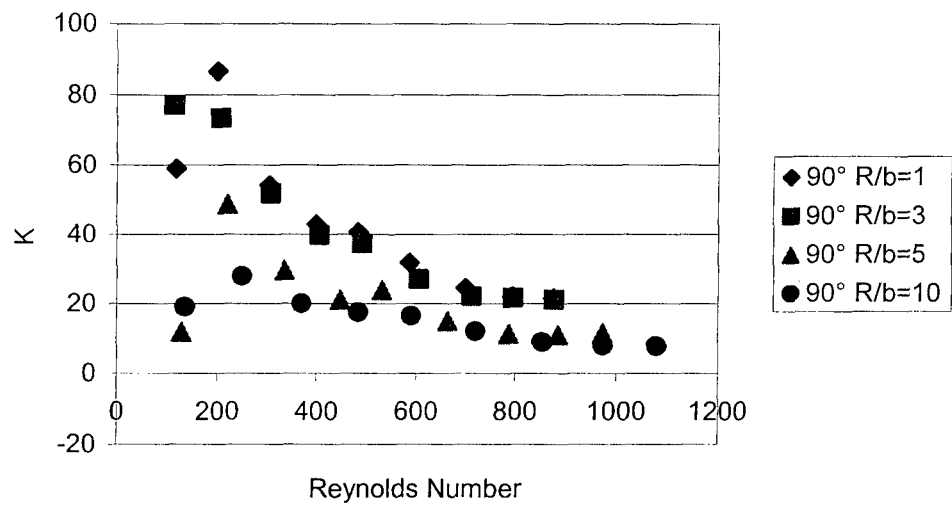


Figure 4-11. 45°Bend Data for 26 μm x 185 μm Channel: Water

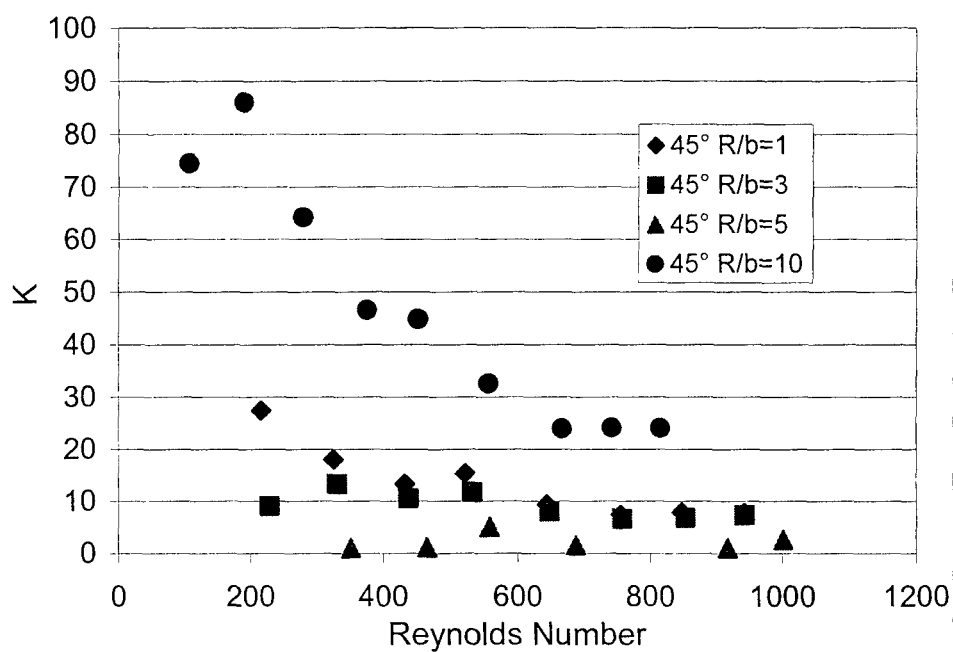


Figure 4-12. 90°Bend Data for 26 μm x 185 μm Channel:
Water

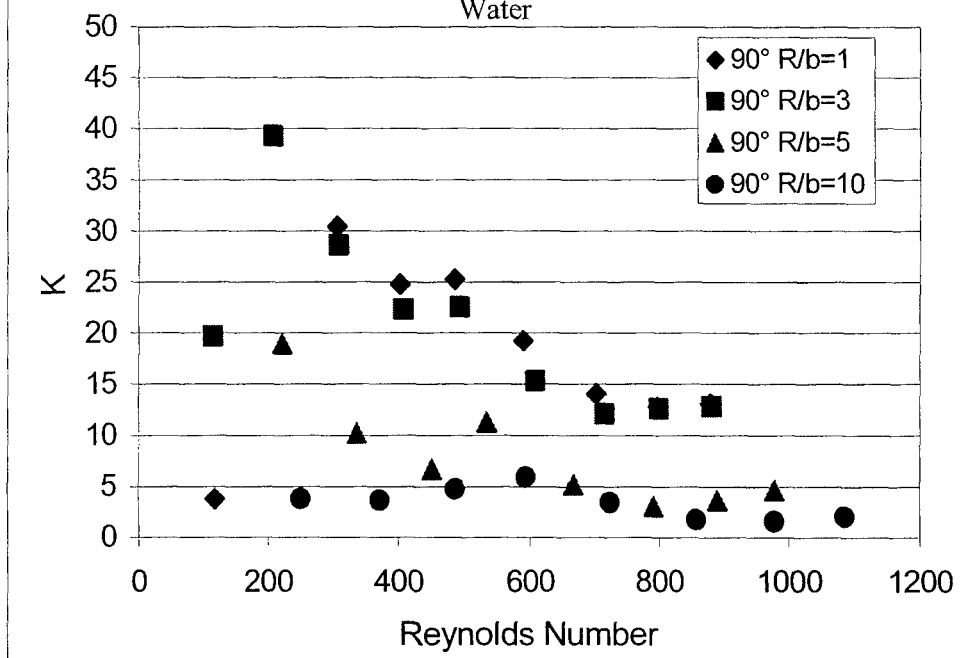


Figure 4-13. 45° Bend Data for 53 μm x 243 μm Channel: Comparison of FC-72 and Water Data

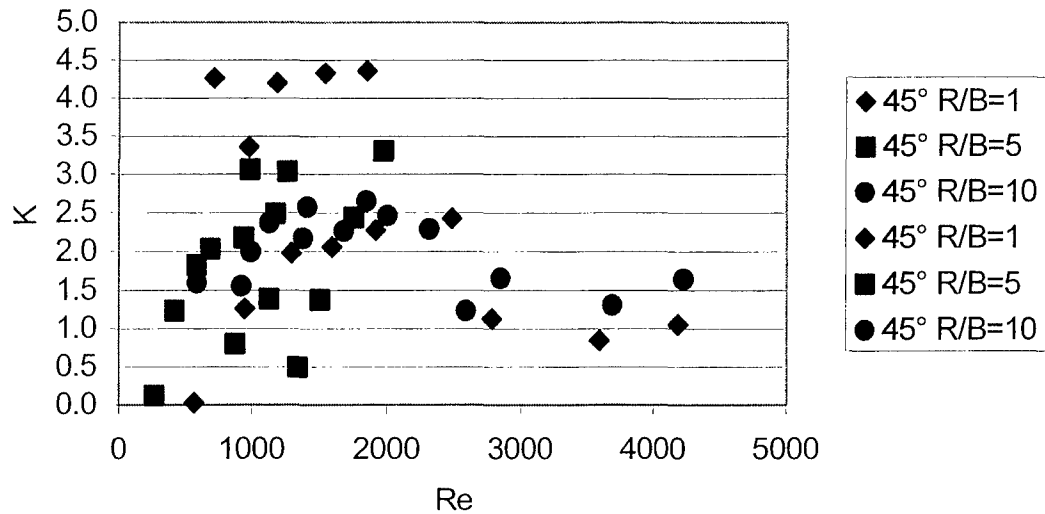


Figure 4-14. 90° Bend Data for 53 μm x 243 μm Channel: Comparison of FC-72 and Water Data

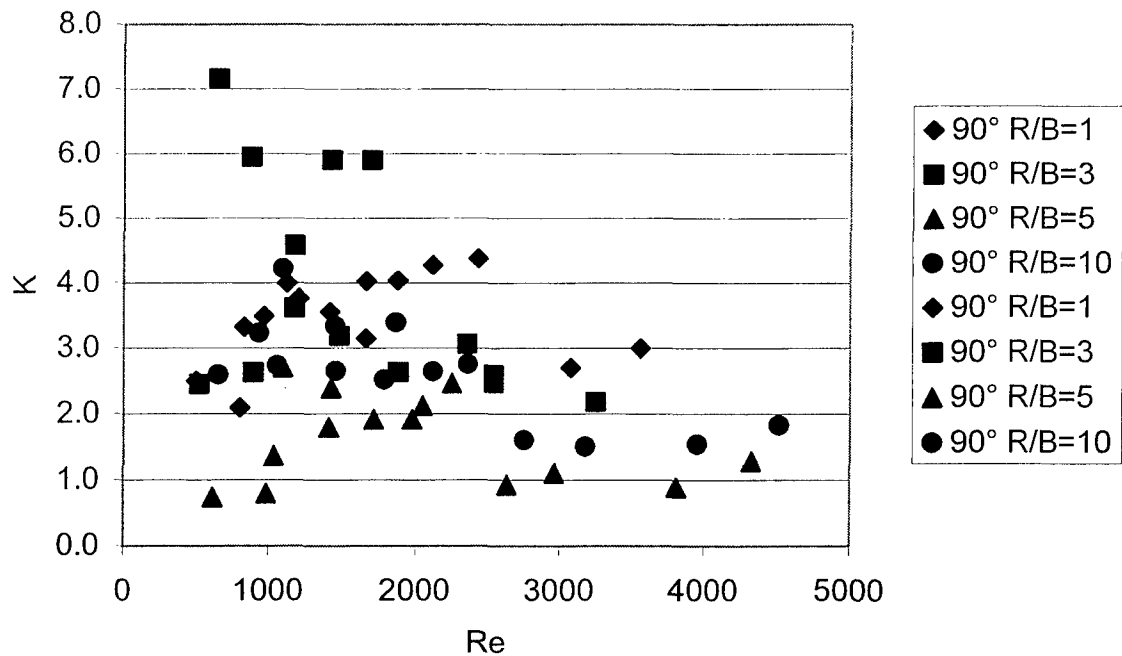


Figure 4-15. 45° Bend Data for 55 μm x 344 μm Channel:
Water

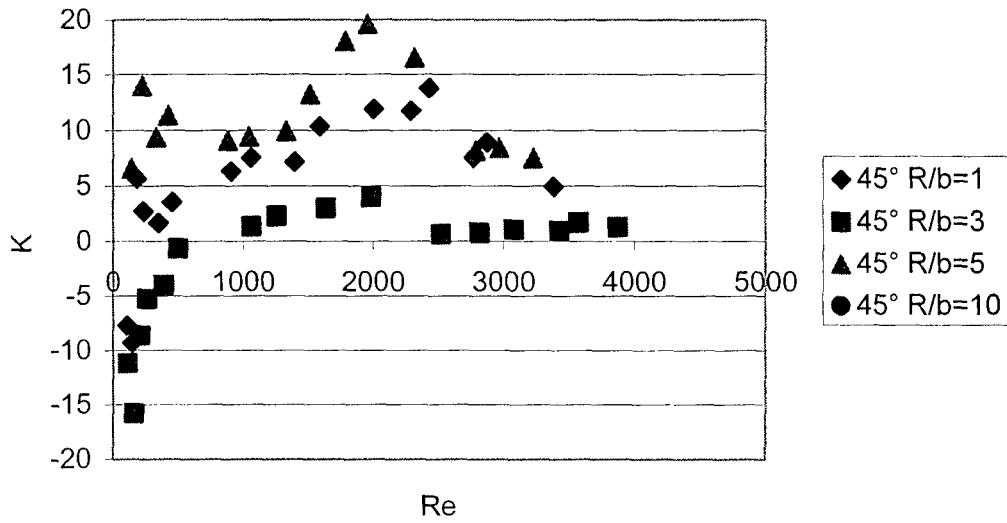


Figure 4-16. 90° Bend Data for 55 μm x 344 μm Channel:
Water

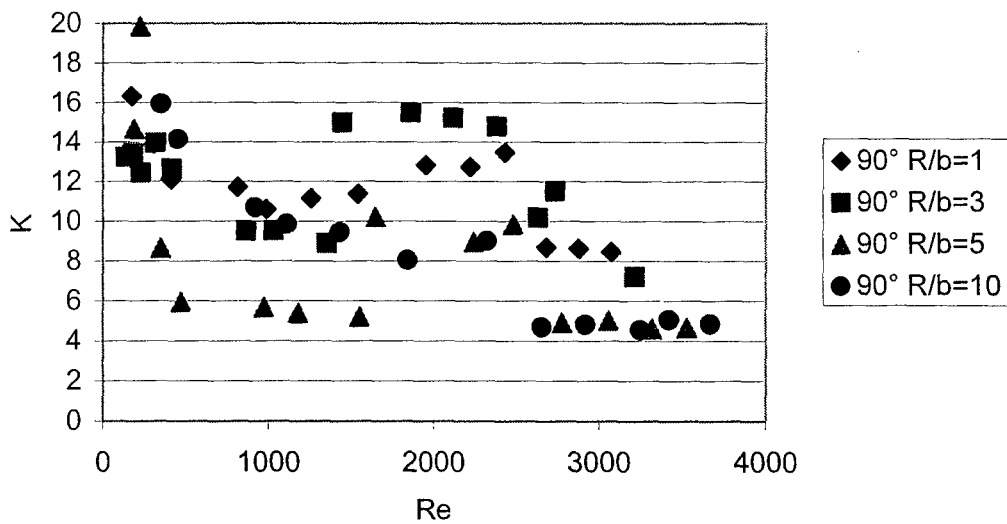


Figure 4-17. 45° Bend Data for 55 μ m x 356 μ m Channels:
Comparison of FC-72 and Water Results

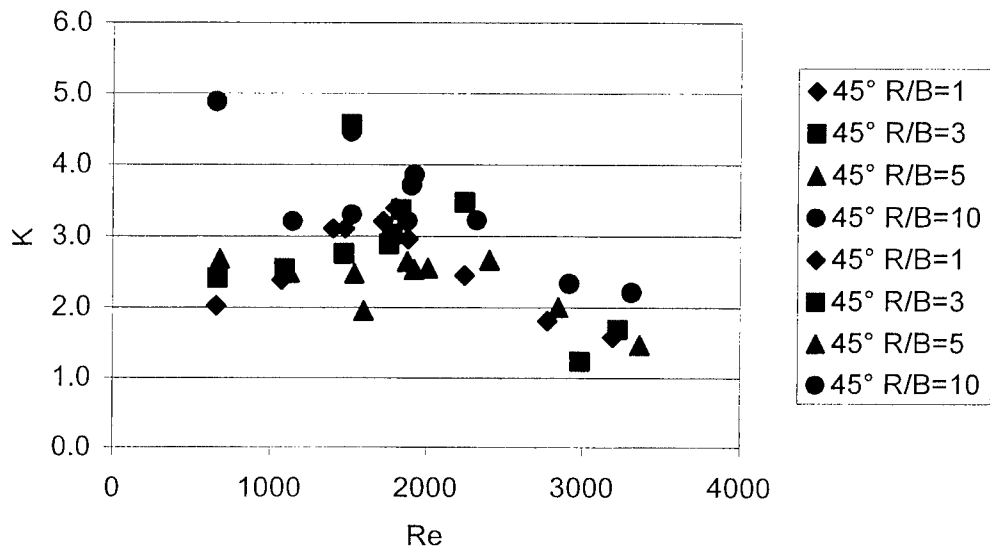


Figure 4-18. 90° Bend Data for 55 μ m x 356 μ m Channels:
Comparison of FC-72 and Water Results

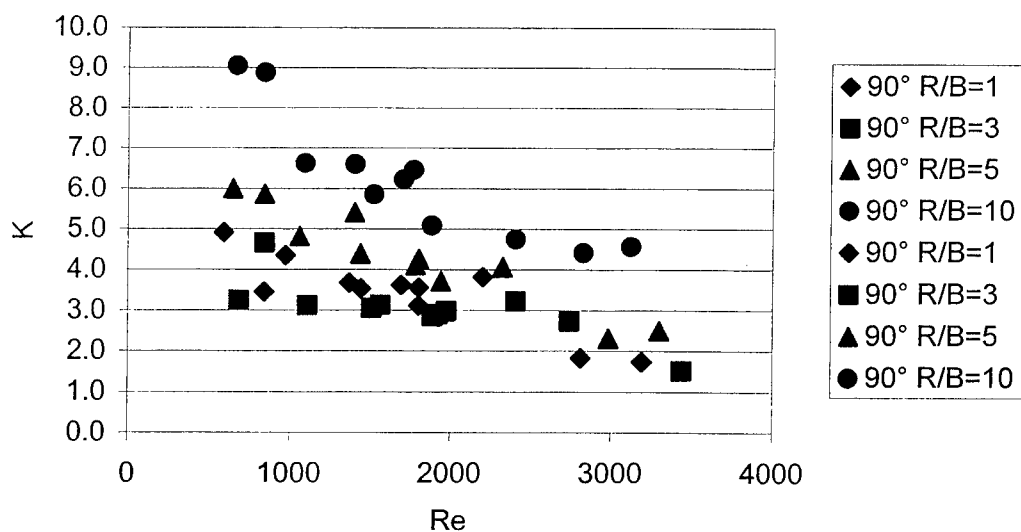


Figure 4-19. 45° Bends: Bend Sharpness Dependency

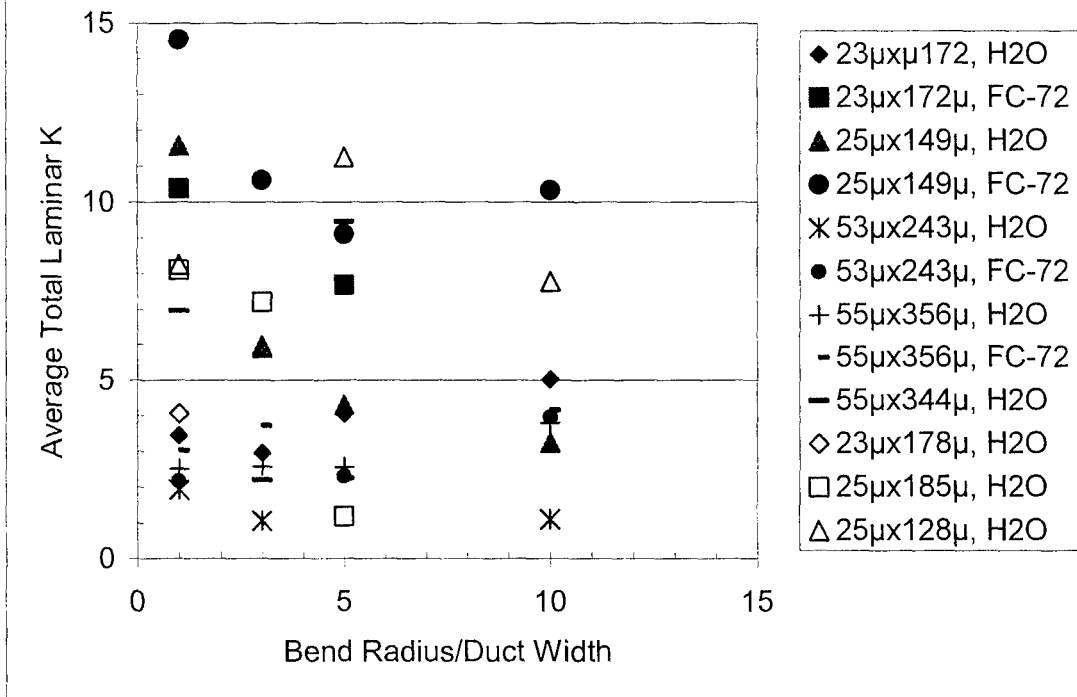


Figure 4-20. 90° Bends: Bend Sharpness Dependency

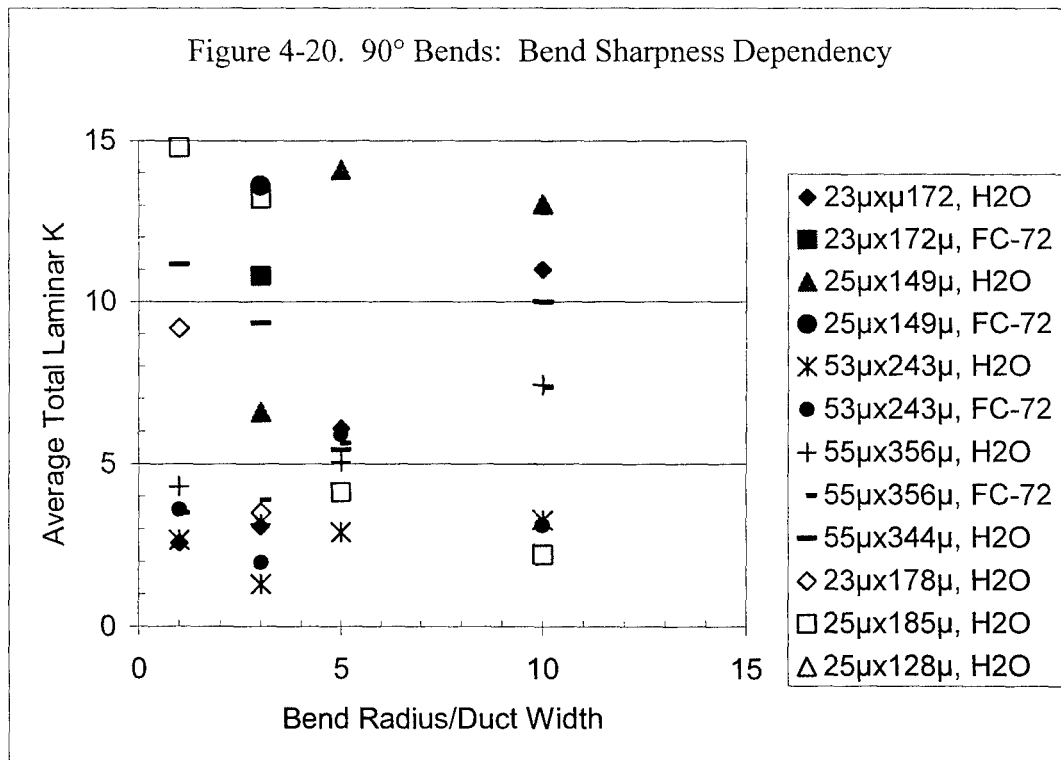


Figure 4-21. Sensitivity to Bend Angle for 25 μ m Channels

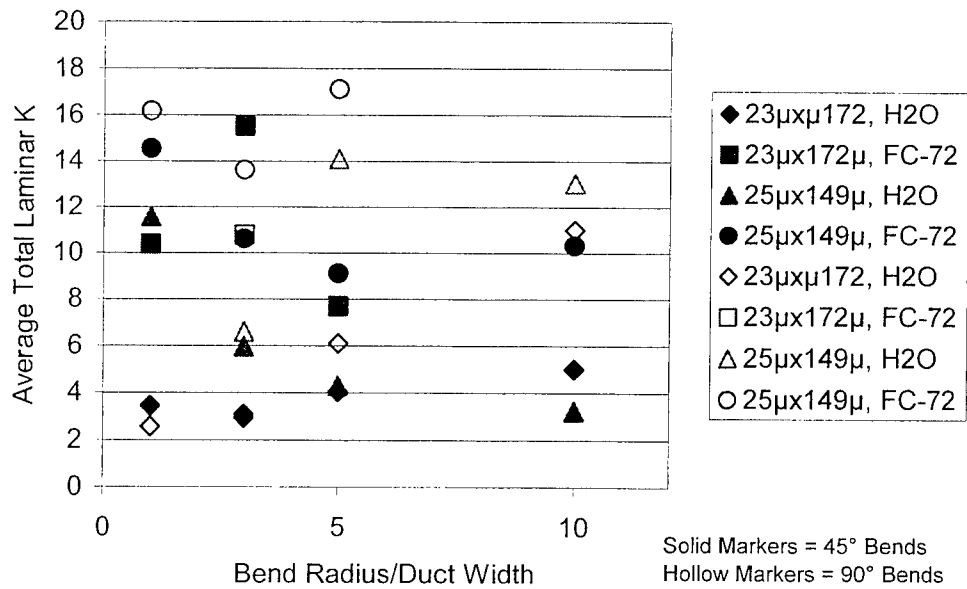


Figure 4-22. Sensitivity to Bend Angle for 50 μ m Channels

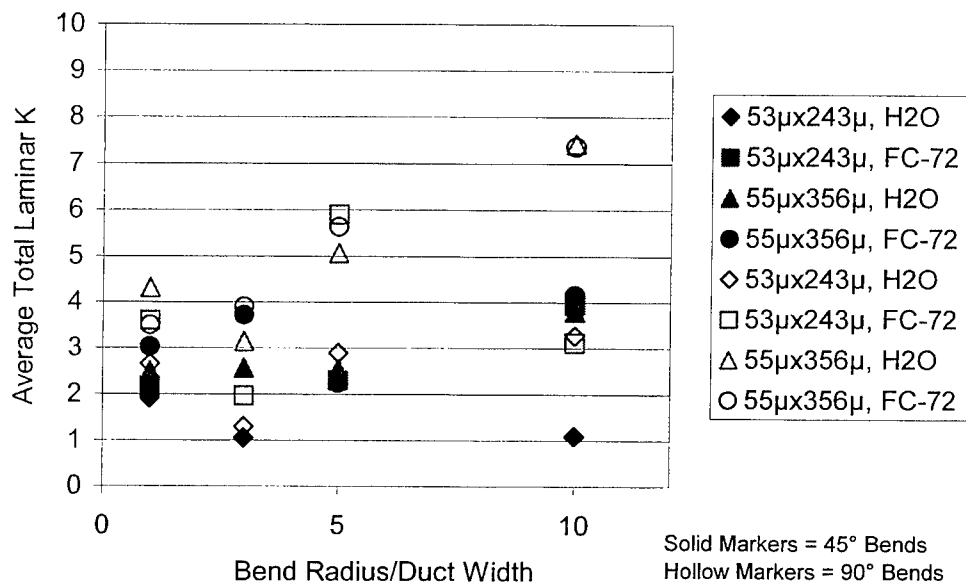


Figure 4-23. 45° Bends: Duct Aspect Ratio Dependence

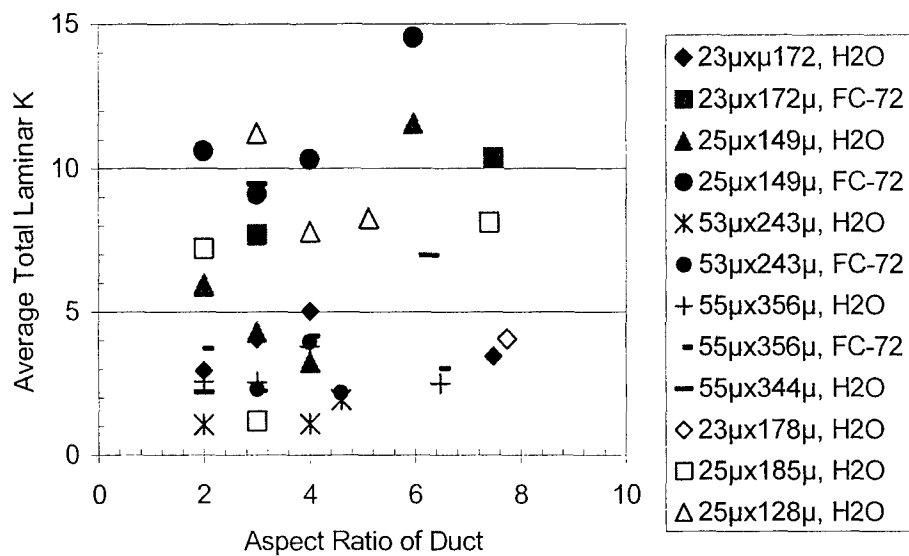
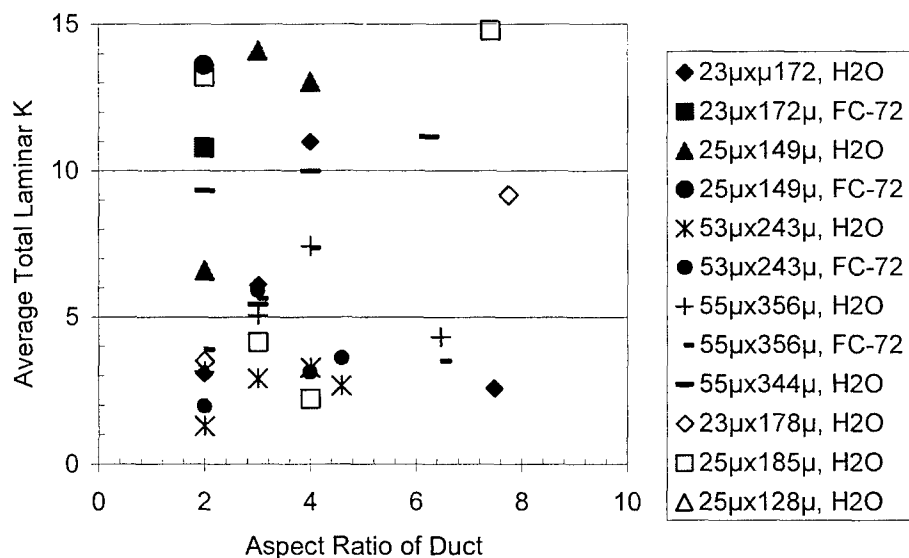


Figure 4-24. 90° Bends: Duct Aspect Ratio Dependence



4.2 Minor Loss Coefficients of Tees and Wyes

Like bends, Tees and Wyes are common features of both macro- and micro-flow systems. The empirically-defined minor loss coefficients are based largely on experiments conducted in circular ducts at Reynolds numbers in excess of 10000, yielding coefficients in the range of 0.2 – 1.5. Obtaining relevant data on minor loss coefficients does not, however, allow one to completely characterize the system: flow is commonly biased toward one branch or the other, even when the branch geometries appear to be identical (Blevins, 1984).

In this task, two test pieces were fabricated, each containing a pair of Wyes (60° and 90°) and a pair of Tees ($R/b = 1$, and $R/b = 3$). The test pieces had nominal channel widths of $25\text{ }\mu\text{m}$ and $50\text{ }\mu\text{m}$, and aspect ratios of 6X and 5X, respectively. The test pieces were tested using water over the maximum attainable range of inlet Reynolds numbers.

The results, shown in Figures 4-25 through 4-28, indicate that the total loss coefficient of the Wyes and Tees for both specimens tends towards a constant value at sufficiently high inlet Re . Most of the $25\text{ }\mu\text{m}$ channels seem to approach a value of 5, which is the largest asymptote among the channels tested. This value is actually lower than the values for the total loss coefficient measured for many of the straight channels, suggesting that exit losses may be an important contributor (since the exit losses are reduced by a factor of 4 due to the splitting of the flow).

As can be seen from the charts, the minor loss coefficient of the Tees is generally higher than that of the Wyes, and the 90° Wyes are more lossy than the 60° Wyes. This is as expected, since the trend is toward progressively smaller momentum change. The results for the two versions of Tees, however, are difficult to distinguish, particularly in the laminar flow regime.

Figure 4-25. Minor Loss Coefficients of 25 μ m Wyres

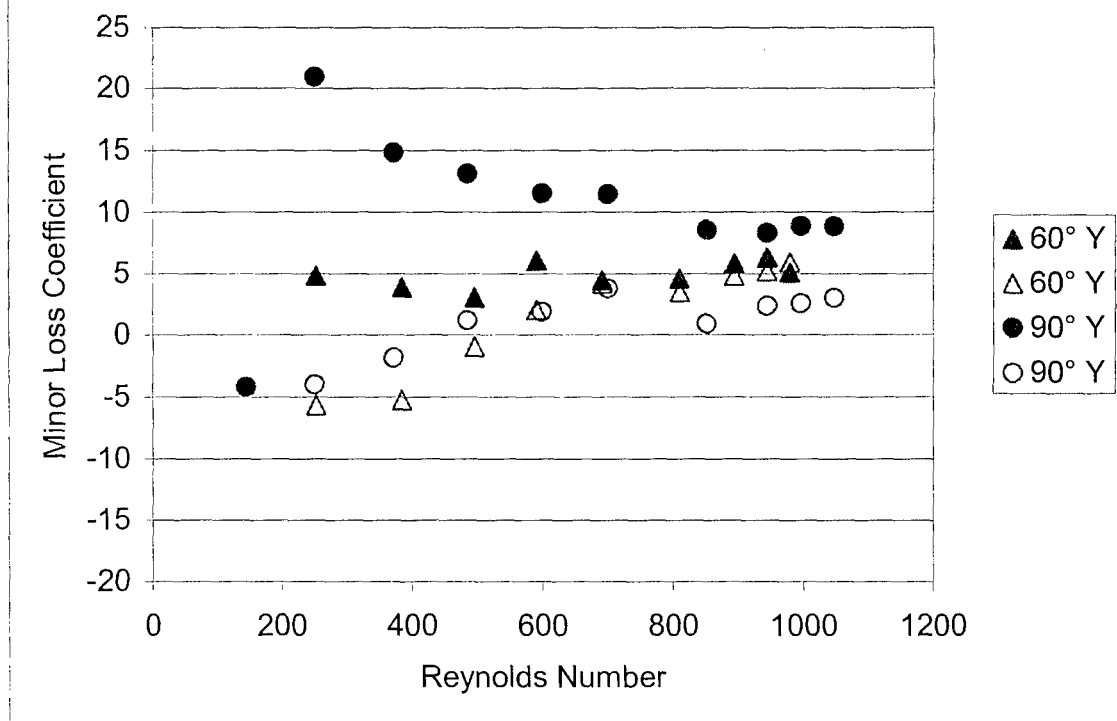


Figure 4-26. Minor Loss Coefficients of 25 μ m Tees

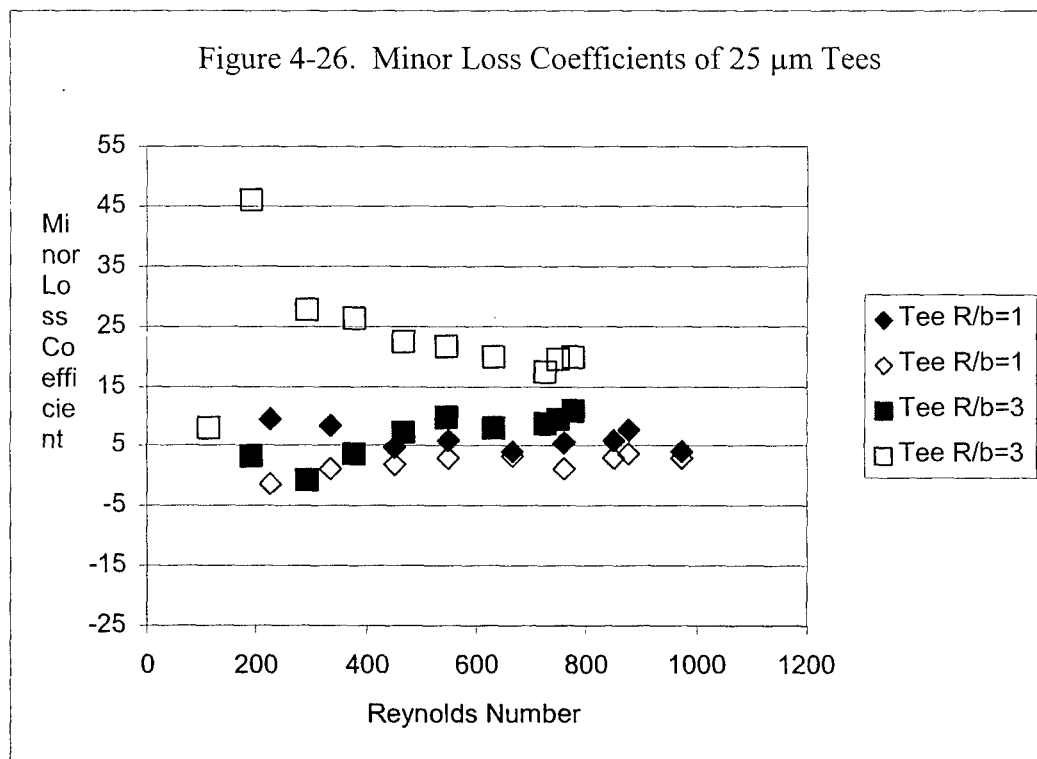


Figure 4-27. Minor Loss Coefficients of 50 μ m Wyes

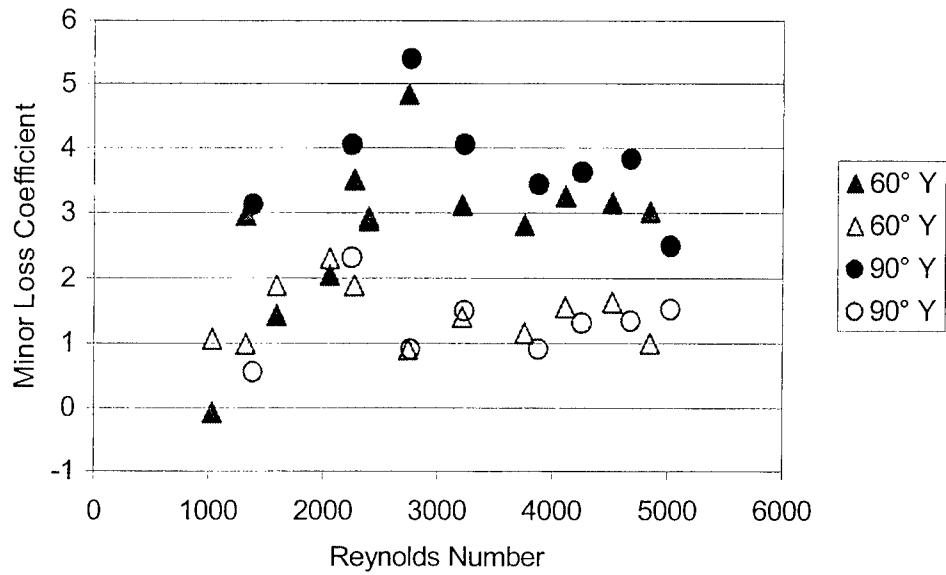
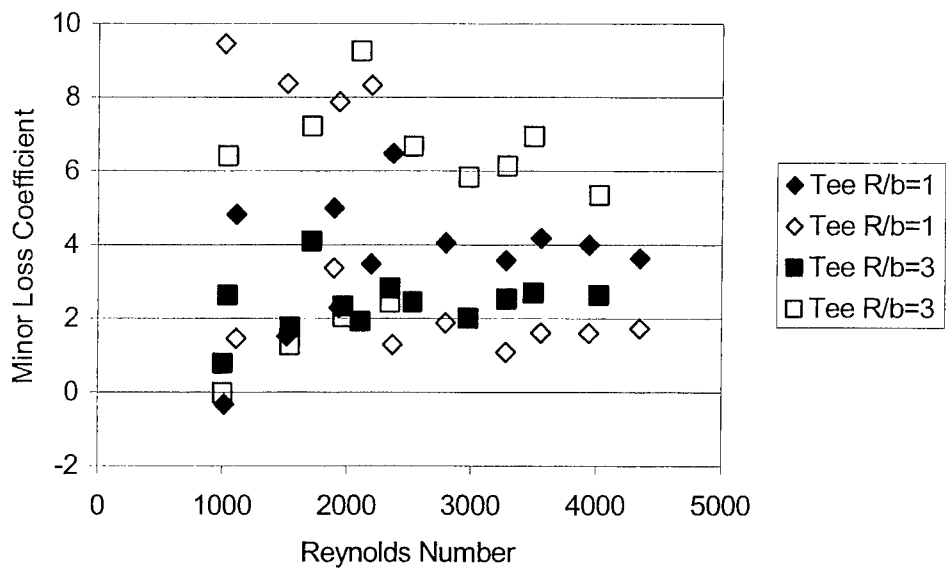


Figure 4-28. Minor Loss Coefficients of 50 μ m Tees



5.0 Summary and Conclusions

5.1 Program Summary & Conclusions

The Micro-Flow Studies program was structured as an experimental heat transfer and fluid flow survey of a variety of relevant micro-geometries. The program was designed to address several fundamental questions which have persisted in the literature, and to provide original data on micro-geometries for which no validated correlations existed. In the pursuit of these goals over 100 flow and heat transfer microchannels were built, and most of these channels were tested with at least two fluids.

The first goal of the program was to verify the experimental approach by comparing the flow data obtained for straight, smooth channels to the theory for laminar flow in rectangular ducts. Ducts of 12.5 μm , 25 μm , and 50 μm were built and tested. Most of the data was within 10% of theory, and all of the data was within 30% of theory. Based on these results, it was felt that the experimental design offered sufficient fidelity to obtain meaningful data.

The second goal was to determine the transition Reynolds number for straight smooth channels. The results of these measurements indicated that transition does not occur until Reynolds numbers of at least 1500. This directly contradicted several reports in the literature concerning observations of transition at Reynolds numbers as low as 300.

The program then focused on evaluating roughness effects on laminar flows in microchannels, since anomalous effects had been reported previously. Samples were prepared with channels of three roughnesses collocated on a single specimen. The flow tests showed a distinct increase in laminar friction factor with increasing roughness, and a decrease in transition Reynolds number with increasing roughness. These results were unexpected, and, if substantiated in future investigations, may be very important to MEMS designers facing the surface texture control limitations of semiconductor processes.

Following the evaluation of smooth and roughened straight channels, the effort changed gears away from an emphasis on fluids science to the development of an engineering database to support the MEMS community. To this end 72 channels with bends of various sizes, aspect ratios, sharpnesses, and angles were fabricated and tested. Minor loss coefficients were derived for each channel, indicating that the bend losses were somewhat higher than observed in macro-channels, although this may have been due to entrance and exit effects. The bend tests were followed by tests of 4 channels with Wytes and 4 channels with Tees. These experiments indicated that exit effects might be significant contributors to the pressure drop and the pressure drop variation among channels.

The 13-month technical period of performance of the program concluded with heat transfer tests on 4 $\mu\text{Heat Exchange}$ specimens. These were preliminary experiments designed to verify the basic testing approach by comparing the results to laminar heat transfer theory for rectangular ducts. Though the samples experienced significant leakage, the experiments and theory agreed closely for both air and water for the samples with the best integrity. The fabrication difficulties were resolved, enabling future testing with the $\mu\text{Heat Exchange}$ method.

5.2 Recommendations

Based on the results summarized above, the major recommendation is to pursue the investigation of the effect of roughness on momentum and heat transfer in laminar flows in microchannels. Many mechanisms have been postulated to explain these types of effects, but it is unclear which, if any, are really contributing to the observed behaviors. A careful, focused research effort concentrating on identifying or eliminating the candidate mechanisms responsible for the apparent increase in friction factor and decrease in transition Reynolds number would prove very useful to both the MEMS and the fluids communities.

The ASME Fluids Engineering Division Summer Meeting 2000 included a panel session on the status and needs of fluids research in microsystems. Representatives from Oregon State University, Harvard University, the Massachusetts Institute of Technology, and Sandia National Laboratory were on the panel. The consensus of the panel was that simple flows in simple geometries were well understood and behaved in a classical fashion, despite contrary experimental results 5 - 10 years ago. Each member of the panel continued with a list of interesting fluids problems at micro-scales, often with redundant items - the relevant portions of their lists have been taken and summarized here:

- \$ Multi-phase Flows
 - Boiling
 - Surface Tension Effects
 - Non-Condensable Bubble Dynamics
 - Interfacial Instabilities
 - Fluids w/Particles and/or Cells
 - Flows w/Free Surfaces

- \$ Reactive Flows
 - Catalyst Development
 - Mixing Enhancement

- \$ Other
 - Electrokinetic Flows
 - Boundary Interactions
 - Porous Media

All of the panelists also mentioned the need for higher pressure pumps and valves, lower cost fabrication processes, system integration, and improved packaging.

6.0 REFERENCES

- Bau, H. (1998), Private Communication, December 3, 1998.
- Blevins, R. D. (1984), *Applied Fluid Dynamics Handbook*, Van Nostrand, 1984.
- Campbell, G. O., et al. (1998), "Semiconductor Laser Array Cooler Development," Final Report for USAF/PL Contract F29601-94-C-0125, November 1998.
- Desai, A., Bökenkamp, D., Yang, X., Tai, Y-C., Marzluff, E., Mayo, S., "Microfluidic Sub-millisecond Mixers for the Study of Chemical Reaction Kinetics," *1997 International Conference on Solid-State Sensors and Actuators*, Vol. 1, pp. 167-170.
- Dussault, H. (1998), Private Communication, October 20, 1998.
- Evans, J., Liepmann, D., Pisano, A., "Planar Laminar Mixer," *10th Annual International Workshop on Micro Electro Mechanical Systems*, Nagoya, Japan, Jan. 26-30, 1997, pp. 96-101.
- Floryan, J. M. (1997), "Stability of wall-bounded shear layers in the presence of simulated distributed surface roughness," *J. Fluid Mech.*, Vol. 335, 1997, pp. 29 - 55.
- Fried, E., and Idelchick, I. (1989), "Flow Resistance: A Design Guide for Engineers," Taylor and Francis, 1989.
- Hu, Sen (1993), "Heat Transfer and Pressure Drop of Liquid-Cooled Offset Fin Heat Exchangers," PhD Thesis, University of Maryland, 1993.
- Kays, W. M., and A. L. London (1984), "Compact Heat Exchangers, 3rd Edition," McGraw-Hill Book Company, New York, New York, 1984.
- Kim, M., Yi, M., Zhong, J., Bau, H., Hu, H., and Ananthasuresh, S. G. K., "The fabrication of flow conduits in ceramic tapes and the measurement of fluid flow through these conduits," *ASME DSC-Vol. 66, MEMS-1998, ASME Int. Mech. Eng. Congress and Expo.*, Nov. 15 - 20, 1998, Anaheim CA, pp. 171 - 177.
- Mala, Gh. M., and Li, D. (1999), Flow characteristics of water in microtubes, *Int. J. of Heat and Fluid Flow*, Vol. 20, 1999, pp. 142 - 148.
- Mala, Gh. M., Li, D., and Dale, J. D. (1997a), "Heat transfer and fluid flow in microchannels," *Int J. of Heat and Mass Transfer*, Vol. 40, No. 13, pp. 3079 - 3088, 1997.
- Mala, Gh. M., Li, D., Werner, C., Jacobasch, H.-J., and Ning, Y.B. (1997b), "Flow characteristics of water through a microchannel between two parallel plates with electrokinetic effects," *Int. J. of Heat and Fluid Flow*, 18:489-496, October 1997.
- Merkle, C. L., Kubota, T., Ko, D. R. S. (1974), "An analytical study of the effects of surface roughness on boundary-layer transition," Final Report for AFOSR/SAMSO AD/A004786.
- Molho, J. I., Herr, A. E., Kenney, T. W., Mungal, M. G., Deshpande, M., Gilbert, J. R., Garguilo, M. G., Paul, P. H., St. John, P. M., Woudenberg, T. M., and Connell, C. (1988), "Fluid transport mechanisms in microfluidic devices," *ASME DSC Vol. 66, 1998 ASME Int. Mech. Eng. Cong. And Exp., MEMS 1998*, pp. 69 - 76, Nov. 15 - 20, 1998.
- Moody, H. L., et al., (1992), "Integrally Cooled Antenna Program," BMO-TR-92-41, Contract F04704-89-C-0022, July 1992.
- Papautsky, I., Brazzle, J., Ameel, T., and Frazier, A. B. (1999a), "Laminar fluid behavior in microchannels using micropolar fluid theory," *Sensors and Actuators*, Vol 73, pp. 101 - 108, 1999.
- Papautsky, I., Gale, B. K., Mohanty, S., Ameel, T. A., and Frazier, A. B. (1999b) Effects of rectangular microchannel aspect ratio on laminar friction constant. *SPIE Vol. 3877*, pp. 147 - 158, *SPIE Conference on Microfluidic Devices and Systems II, Santa Clara, CA*, September 1999.

- Peng, X. F., et al.(1995a), "Experimental Investigation of Heat Transfer in Flat Plates with Rectangular Microchannels," *Int. J. of Heat and Mass Transfer*, Vol. 38, No. 1, p. 127, 1995.
- Peng, X. F., and G. P. Peterson (1995b), "The Effect of Thermofluid and Geometrical Parameters on Convection of Liquids Through Rectangular Microchannels," *Int. J. of Heat and Mass Transfer*, Vol. 38, No. 4, p. 755, 1995.
- Pfahler, J. et al. (1990), "Liquid Transport in Micron and Submicron Channels," *Sensors and Actuators*, A21-A23, 1990, pp. 431-434.
- Pfahler, J. et al. (1991), "Gas and Liquid Flow in Small Channels," *ASME DSC Vol. 32, Micromechanical Sensors, Actuators and Systems*, pp. 49 - 60, 1991.
- Phillips, R. J. (1988), "Forced-Convection, Liquid-Cooled Microchannel Heat Sinks, AD-A193-337, MIT/LL Technical Report 787, Lexington, MA, 7 January 1988.
- Shaw, R. K. and A. L. London (1978), "Laminar Flow Forced Convection in Ducts," in *Advances in Heat Transfer*, T. F. Irvine, Jr. and J. P. Hartnett (eds.), Academic Press, New York, 1978.
- Tuckerman, D. B. (1984), "Heat Transfer Microstructures for Integrated Circuits," PhD Thesis, Stanford University, 1984.
- Wang, B. X., and X. F. Peng (1994), "Experimental Investigation on Liquid Forced-Convection Heat Transfer Through Microchannels," *Int. J. of Heat and Mass Transfer*, Vol. 37, Suppl. 1, p. 73, 1994.
- Weiting, A. R. (1975), Empirical Correlations for Heat Transfer and Flow Friction Characteristics of Rectangular Offset-Fin Plate-Fin Heat Exchangers," *Journal of Heat Transfer*, Trans. ASME, vol. 97C(2), 1975, p. 488.
- Wu, P., and W. A. Little (1983), "Measurement of Friction Factors for the Flow of Gases in Very Fine Channels Used for Microminiature Joule-Thomson Refrigerators," *Cryogenics*, May 1983, p. 273.
- Wu, P., and W. A. Little (1984), "Measurement of the Heat Transfer Characteristics of Gas Flow in Fine Channel Heat Exchangers Used for Microminiature Refrigerators," *Cryogenics*, August 1984, p. 415.
- Yang, C., and Li, D., "Analysis of electrokinetic effects on the liquid flow in rectangular microchannels," *Colloids and Surfaces, A:Physicochemical and Engineering Aspects*, Vol 143, pp. 339 - 353, 1998.
- Yang, C., Li, D., and Masliyah, J. H., "Modeling forced liquid convection in rectangular microchannels with electrokinetic effects," *Int. J. of Heat and Mass Transfer*, 41:4229-4249, 1998.
- Yin, X., and Bau, H. (1997), "Micro heat exchangers consisting of pin arrays," *Trans. of the ASME, J. of Elec. Packaging*, Vol. 119, March 1997.

Appendix 1 Straight Channel Specimen Descriptions and Test Data

Four straight channel specimens were fabricated and tested during the program. Two of the test pieces, labeled "P" and "A", contained six channels: 3 with a nominal 4X aspect ratio and 3 with a nominal 10X aspect ratio. The channels in "P" were nominally 12.7 μm wide, and the channels in "A" were roughly 25 μm wide. Specimens "G" and "D" had only three channels each, due to the larger channel sizes. Test sample "G" had 50 μm wide channels with a nominal 4X aspect ratio, while Sample "D" had 50 μm channels with a 10X aspect ratio.

Detailed dimensions for each channel are included in the sample descriptions provided in this appendix. The sample data also includes profilometer scans of the top and bottom of each channel, to aid in interpreting the flow data for the roughened channels. All of the samples were tested with water, nitrogen and FC-72: the table below provides a local table of contents to aid in navigating through the sample characterization data and the test data.

Table A-1. Guide to Straight Channel Specimen Descriptions and Test Data

Sample	Width	Height (μm)	Fluid	Page #
P	13	95	Sample Description	A-3
			Water	A-4
			FC-72	A-4
			Nitrogen	A-5
		178	Sample Description	A-4
			Water	A-4
			FC-72	A-4
			Nitrogen	A-5
A	23	148	Sample Description	A-6
			Water	A-8
			FC-72	A-8
			Nitrogen	A-9
		275	Sample Description	A-10
			Water	A-11
			FC-72	A-11
			Nitrogen	A-12
G	53	25.4	Sample Description	A-14
			Water	A-16
			FC-72	A-16
			Nitrogen	A-17
D	53	25.4	Sample Description	A-18
			Water	A-20
			FC-72	A-20
			Nitrogen	A-21

Table A-2. Sample P: 13 μm Straight Channels w/4X and 10X Aspect Ratios

Actual Sample Dimensions (Channel Length = 24079 μm)

Nominal Description		Smooth 4X	2% Roughness 4X	10% Roughness 4X	Smooth 10X	2% Roughness 10X	10% Roughness 10X
Depth (μm)		13	13	13	13	13	13
Width (μm)		95	95	95	178	178	178
e/D_H	Bottom	0.011	0.028	0.10	0.011	0.027	0.090
	Top	0.011	0.034	0.10	0.012	0.037	0.095

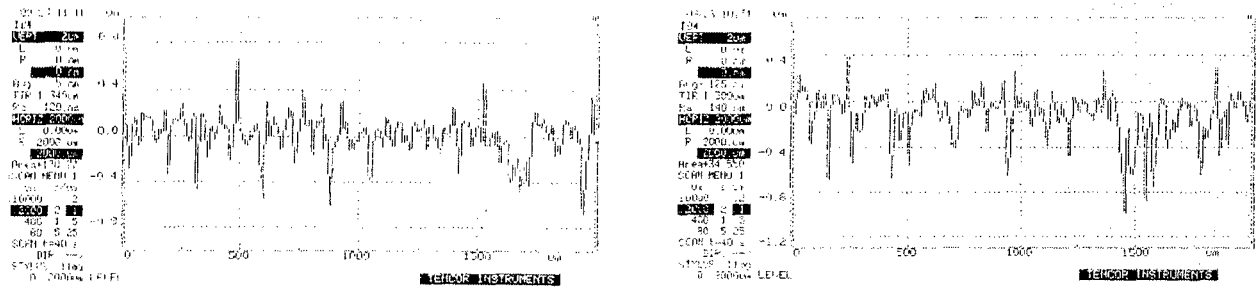


Figure A-1. Profilometer Traces of Bottom (left) and Top (right) Plates: “Smooth” 4X Channels

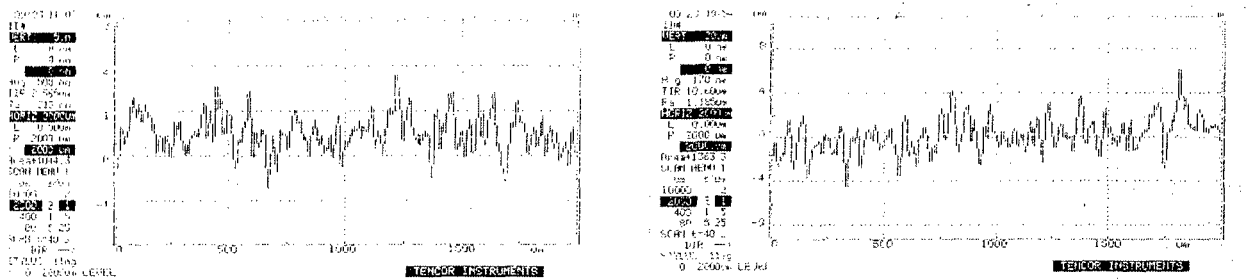


Figure A-2. Profilometer Traces of Bottom (left) and Top (right) Plates: 2% Roughened 4X Channels

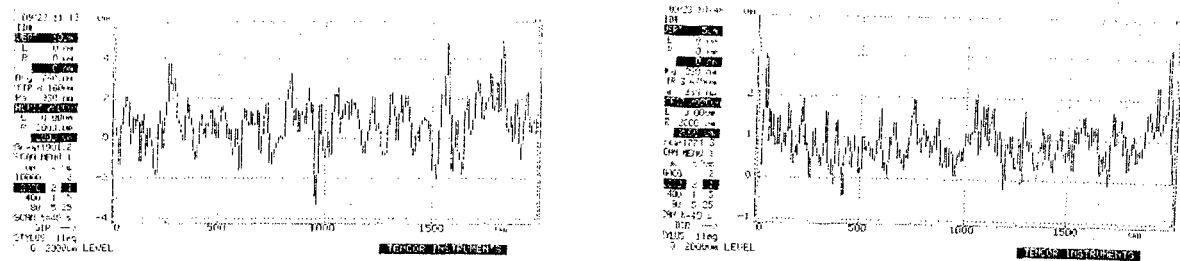
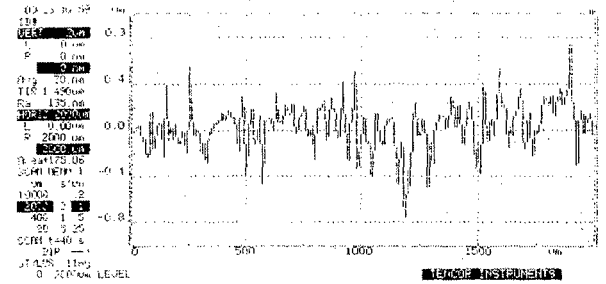
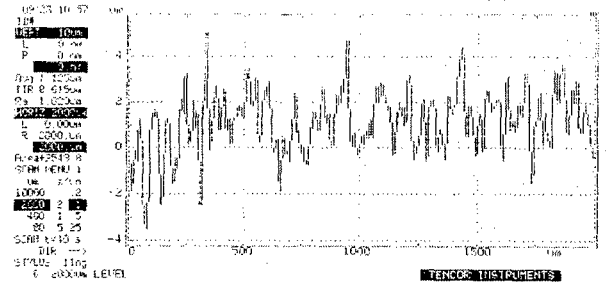
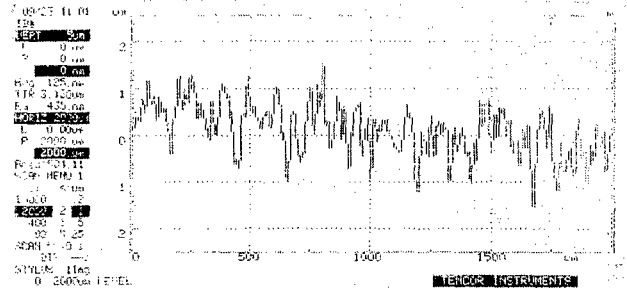


Figure A-3. Profilometer Traces of Bottom (left) and Top (right) Plates: 10% Roughened 4X Channels



0928 11-75
REF Sun
F 100
C 6.40
D 0.00
Sgt 225 Hz
TK 7.530 Hz
Es 20K Hz
MSV 5700
L 0.000
P 2000 Hz
5000 VLS
Dist 157.70
COM RWR 1
UE 5700
10000 2
AES 1 0 P
400 1 S
R0 5.25
SWP 2=40 S
BIR
STATUS 11%
G 200000 LEVEL

15000 INSTRUCTIONS

[illegible]

81

Figure A-7. Straight Channel: 13 μm x 95 μm and 13 μm x 178 μm , Water

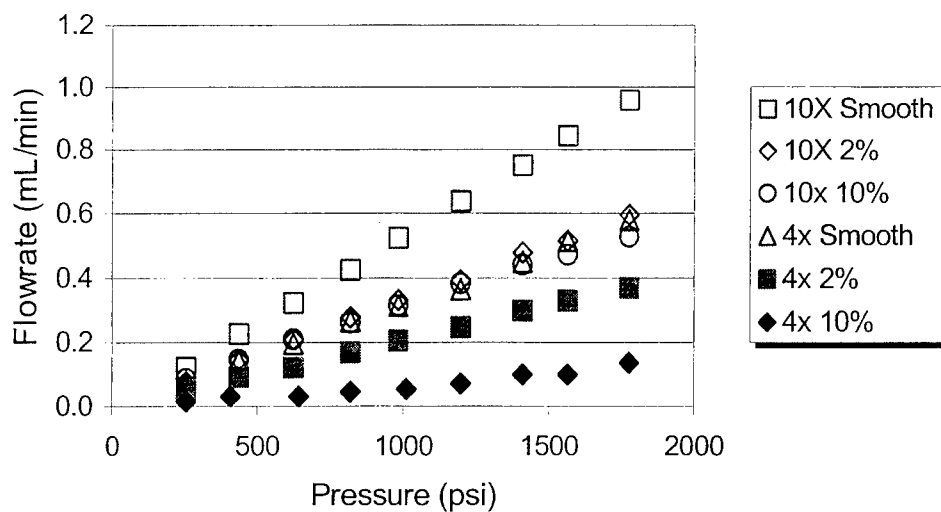


Figure A-8. Straight Channel: 13 μm x 95 μm and 13 μm x 178 μm , FC-72

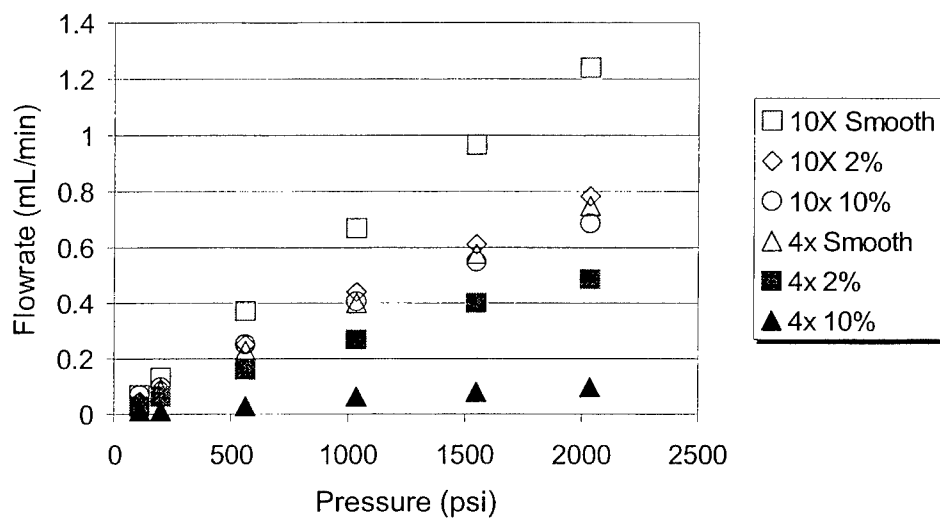


Figure A-9. Straight Channel: 13 μm x 95 μm and 13 μm x 178 μm , Nitrogen

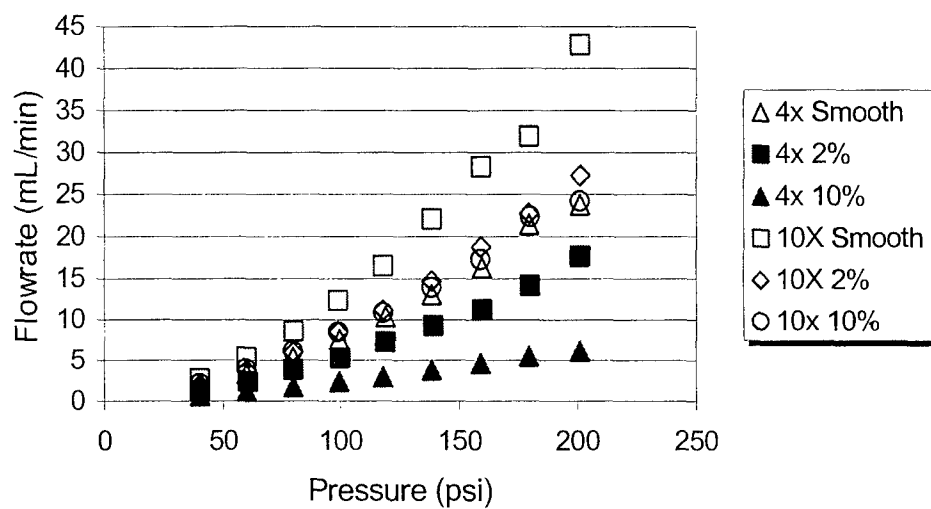


Table A-3. Sample A: 23 μm Straight Channels w/4X and 10X Aspect Ratios

Actual Sample Dimensions (Channel Length = 12700 μm)

Nominal Description		Smooth 4X	2% Roughness 4X	10% Roughness 4X	Smooth 10X	2% Roughness 10X	10% Roughness 10X
Depth (μm)		23	23	23	23	23	23
Width (μm)		140	152	152	267	279	279
e/D_H	Bottom	0.006	0.015	0.075	0.003	0.013	0.070
	Top	0.006	0.016	0.063	0.002	0.061	0.053

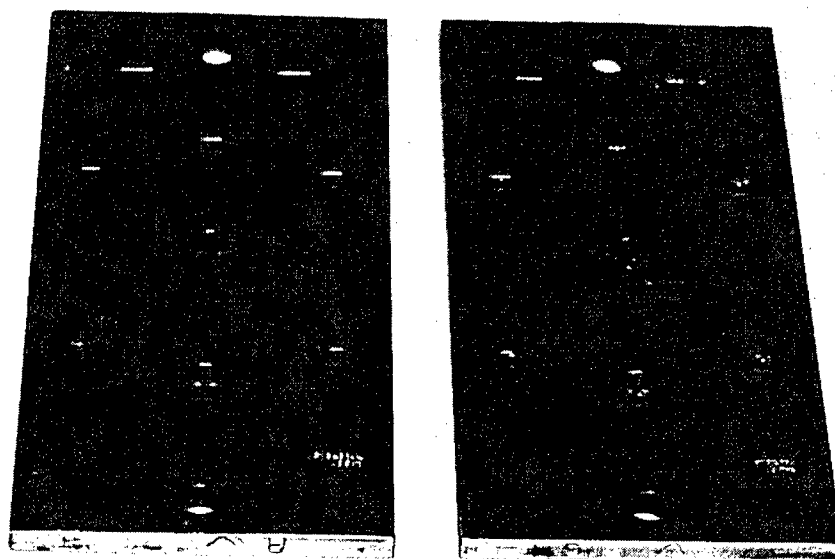


Figure A-10. Sample A. Top and Bottom Steel Plates w/Roughened Areas

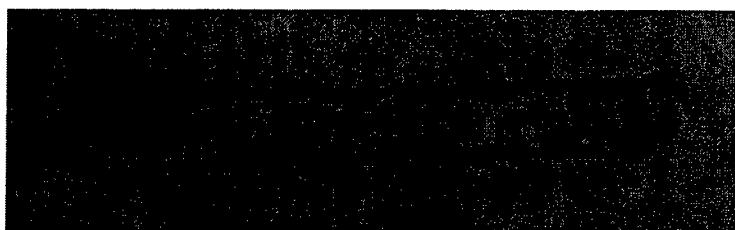


Figure A-11. Photomicrograph of Sacrificial Channel Cross-section (200X)

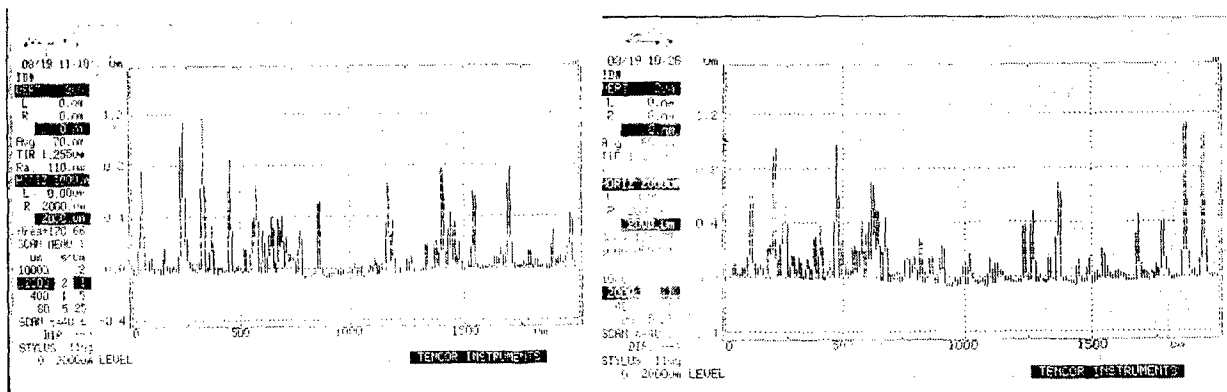


Figure A-12. Profilometer Traces of Bottom(left) and Top (right) Plates: Smooth 4X Channels

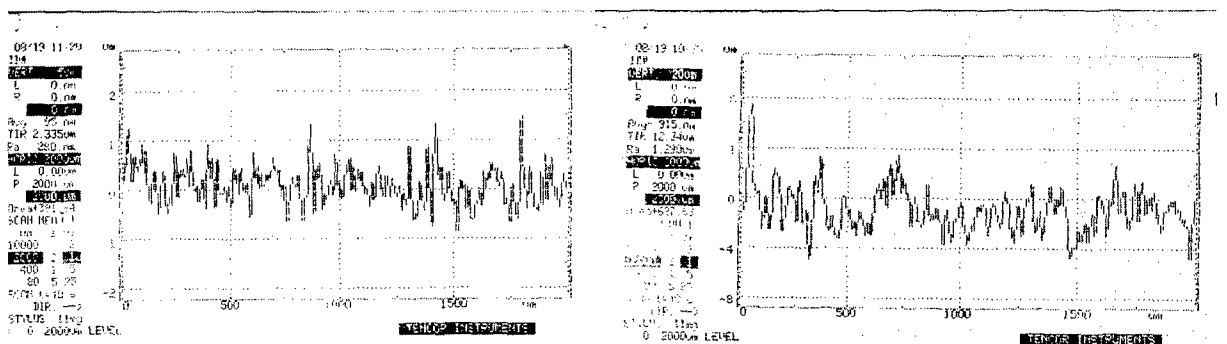


Figure A-13. Profilometer Traces of Bottom (left) and Top (right) Plates: 2% Roughened 4X Channels

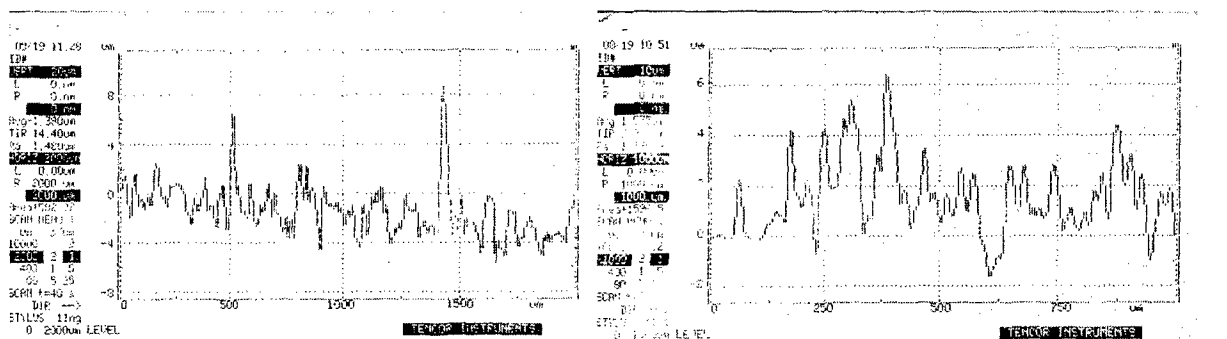


Figure A-14. Profilometer Traces of Bottom (left) and Top (right) Plates: 10% Roughened 4X Channels

Figure A-15. Straight Channel Data: 23 μm x 148 μm , Water

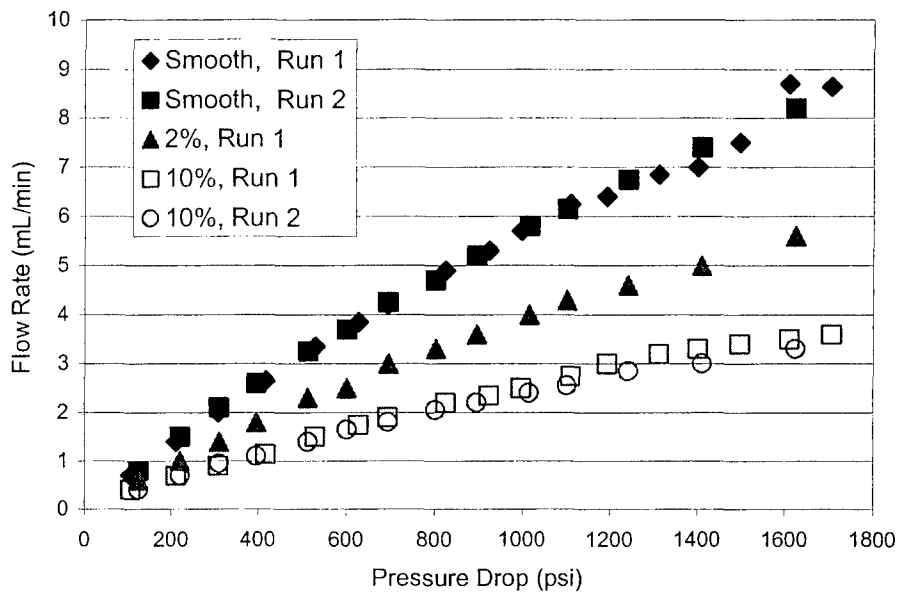


Figure A-16. Straight Channel Data: 23 μm x 148 μm , FC-72

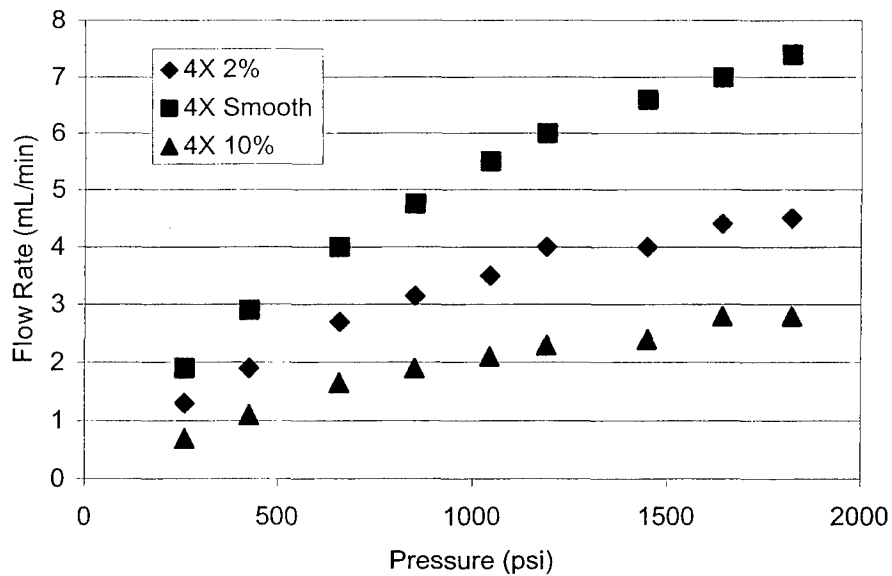


Figure A-17. Straight Channel: 23 μm x 148 μm , Nitrogen

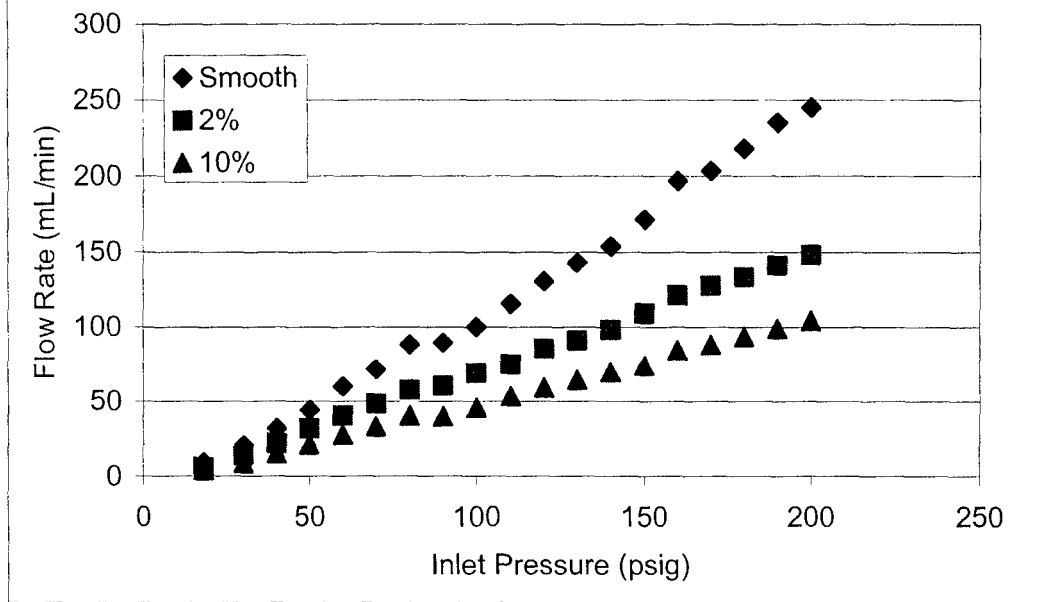


Figure A-21. Straight Channel Data: 23 μm x 275 μm , Water

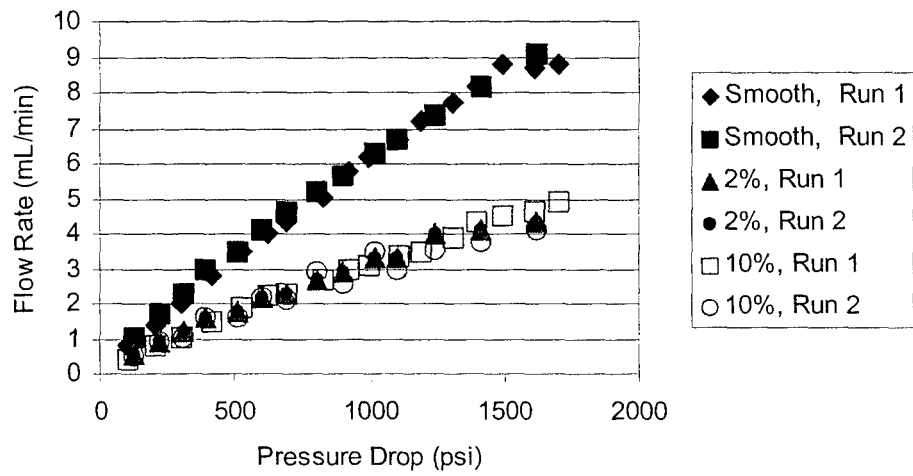


Figure A-22. Straight Channel Data: 23 μm x 275 μm , FC-72

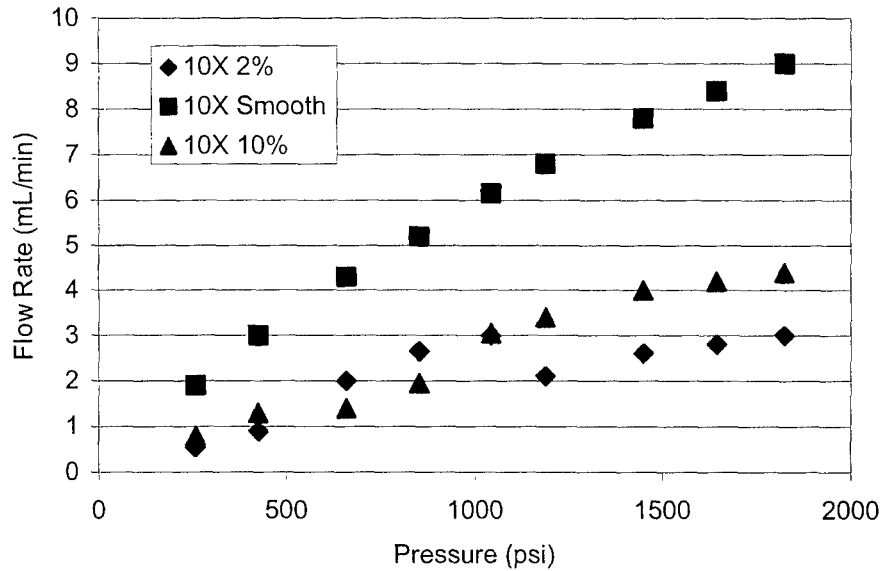


Figure A-23. Straight Channel: 23 μm x 275 μm , Air

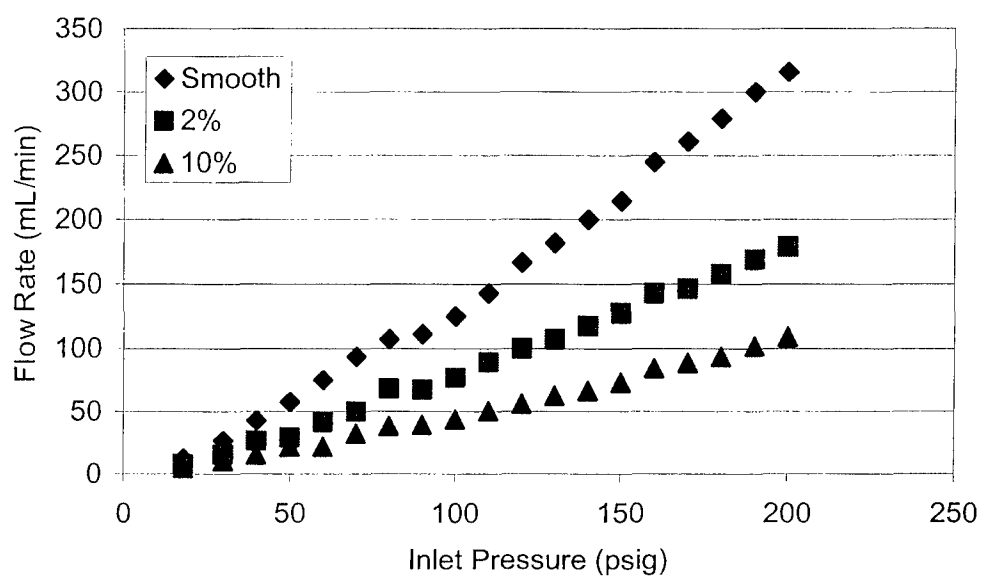


Table A-4. Sample G: 50 μm Straight Channels w/4X Aspect Ratios

Table A-2. Actual Sample Dimensions (Channel Length = 63500 μm)

Nominal Description		Smooth 4X	2% Roughness 4X	10% Roughness 4X
Depth (μm)		66	66	66
Width (μm)		241	241	248
e/D_H	Bottom	0.006	0.015	0.075
	Top	0.006	0.016	0.063

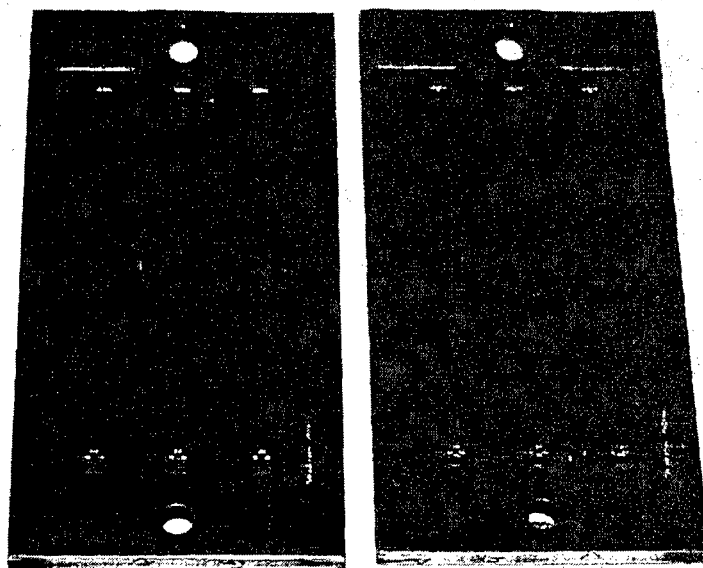


Figure A-24. Sample G. Top and Bottom Steel Plate w/Roughened Areas

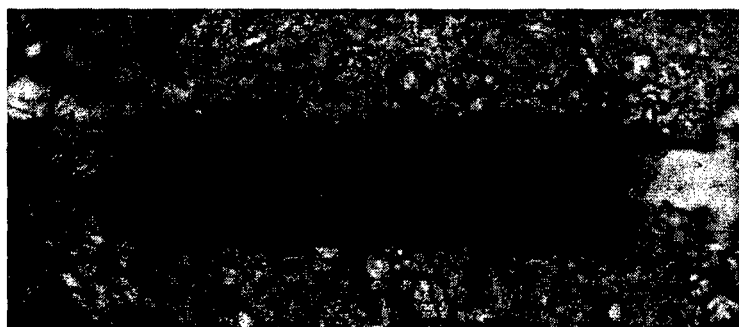


Figure A-25. Photomicrograph of Sacrificial Channel Cross-section (200X)

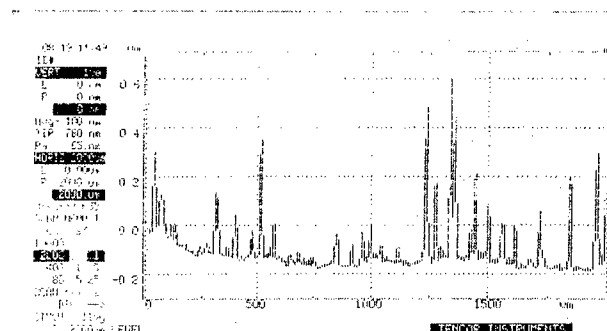
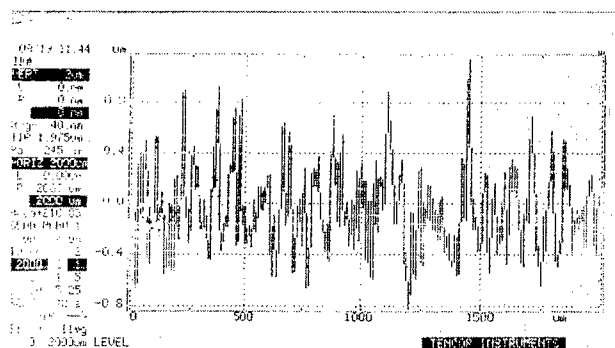
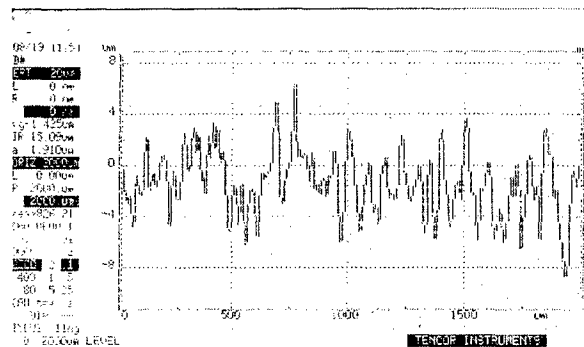
[illegible]

Figure A-27. Profilometer Traces of Bottom (left) and Top (right) Plates: 2% Roughened 4X Channels



93

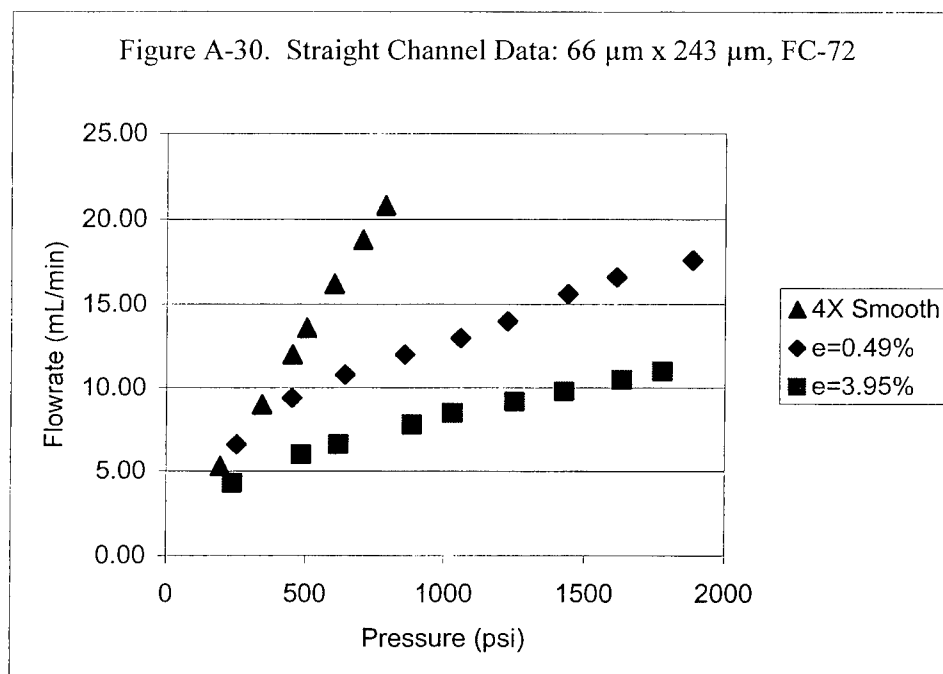
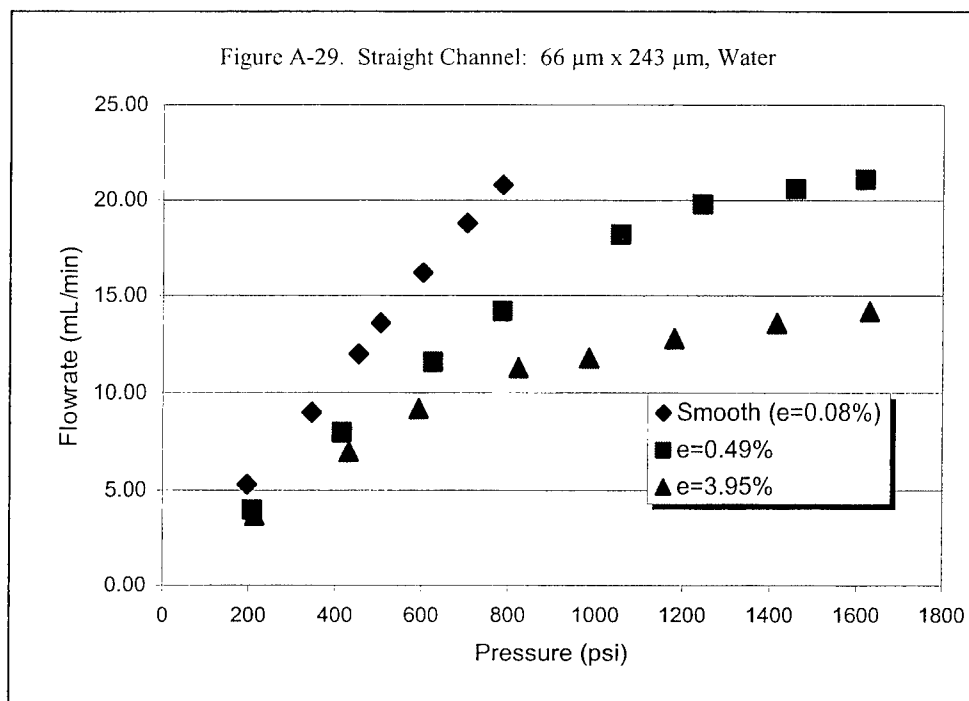


Figure A-31. Straight Channel Data: 66 μm x 243 μm ,
Nitrogen

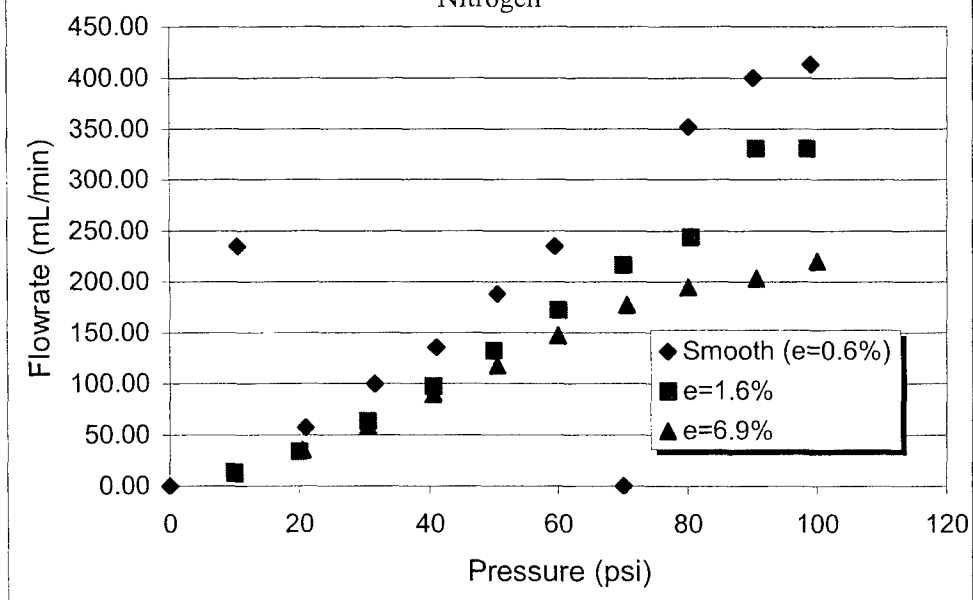


Table A-5. Sample D: 50 μm Straight Channels w/10X Aspect Ratios
Actual Sample Dimensions (Channel Length = 63500 μm)

Nominal Description		Smooth 10X	2% Roughness 10X	10% Roughness 10X
Depth (μm)		57	57	57
Width (μm)		597	597	610
e/D_H	Bottom	0.001	0.005	0.042
	Top	0.001	0.006	0.044

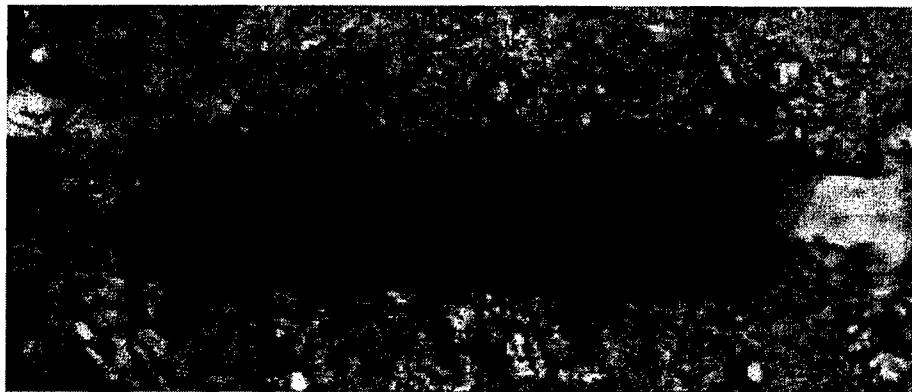


Figure A-32. Cross-Section of Sacrificial Channel (200X)

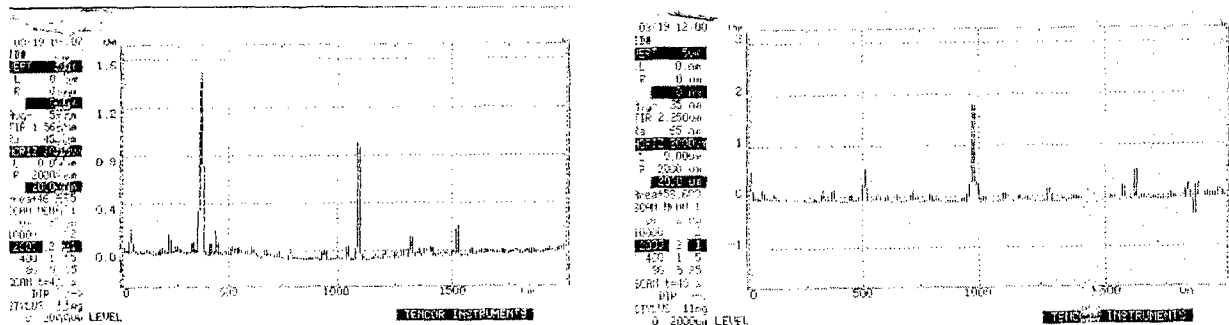


Figure A-33. Profilometer Traces for Bottom (left) and Top (right) Plates: Smooth 10X Channels

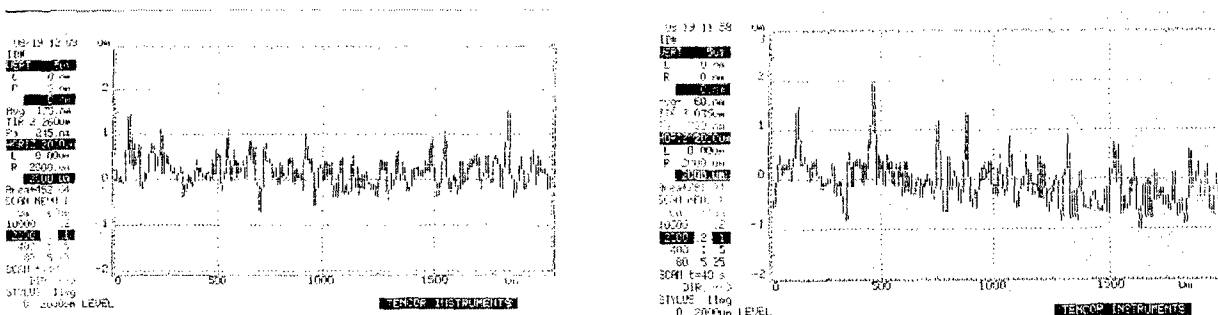


Figure A-34. Profilometer Traces for Bottom (left) and Top (right) Plates: 1% Roughened 10X Channels

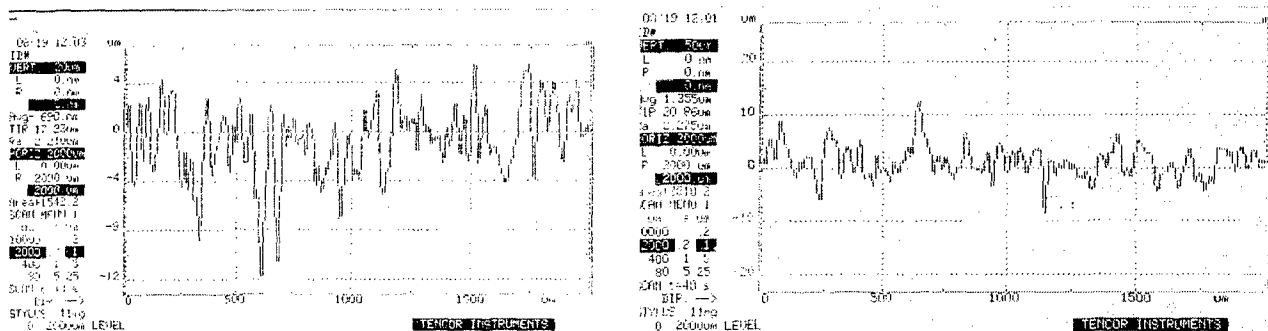


Figure A-35. Profilometer Traces for Bottom (left) and Top (right) Plates: 10% Roughened 10X Channels

Figure A-36. Straight Channel Data: 56 μm x 600 μm , Water

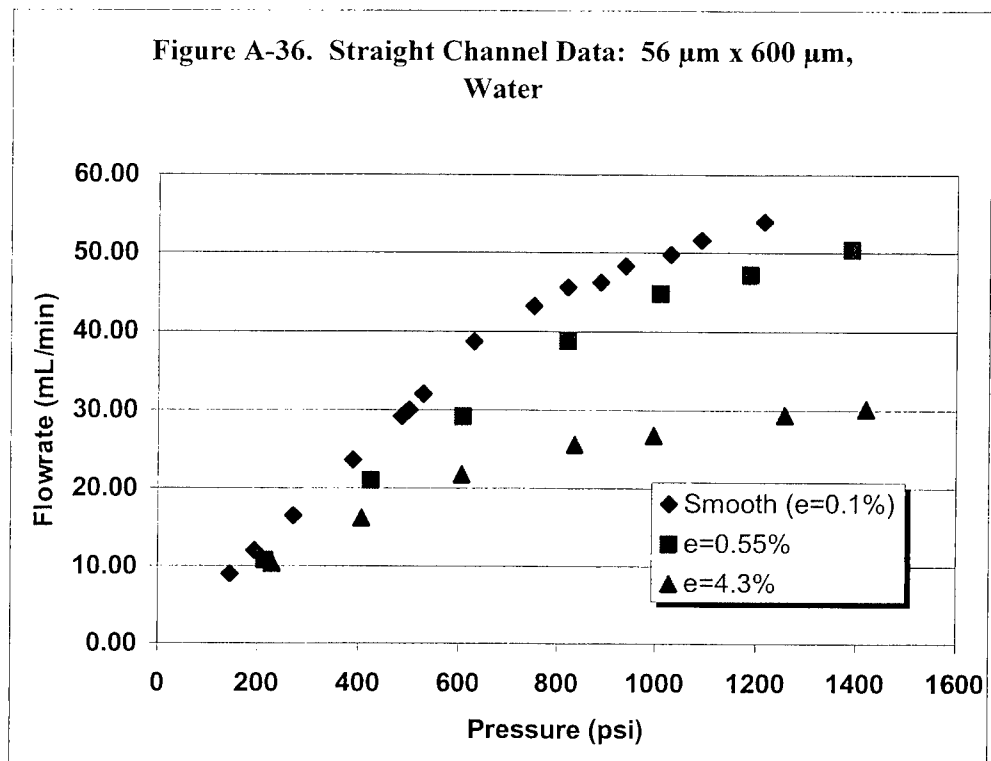


Figure A-37. Straight Channel Data: 56 μm x 600 μm , FC-72

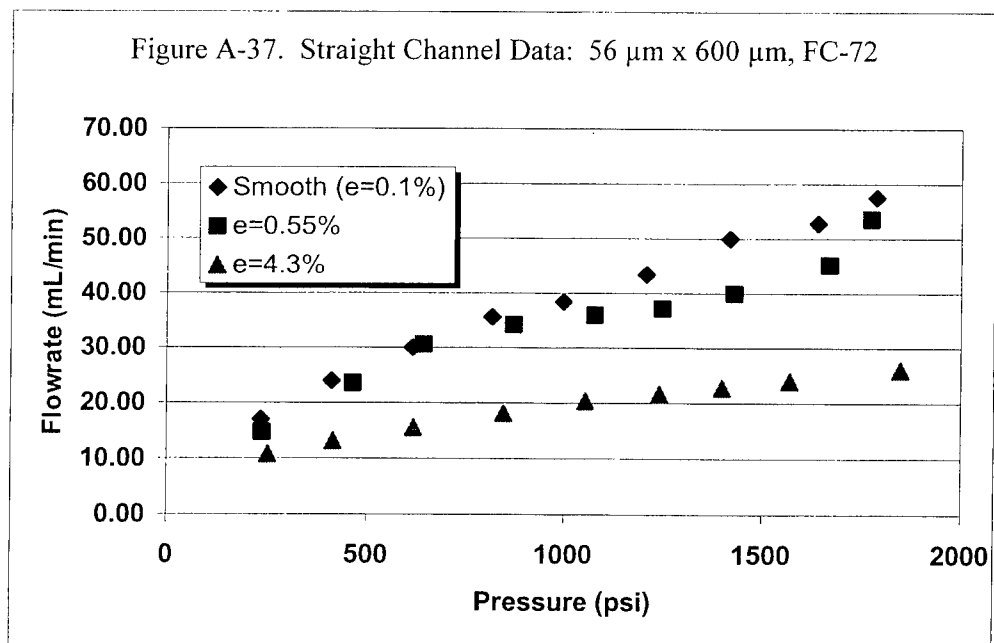
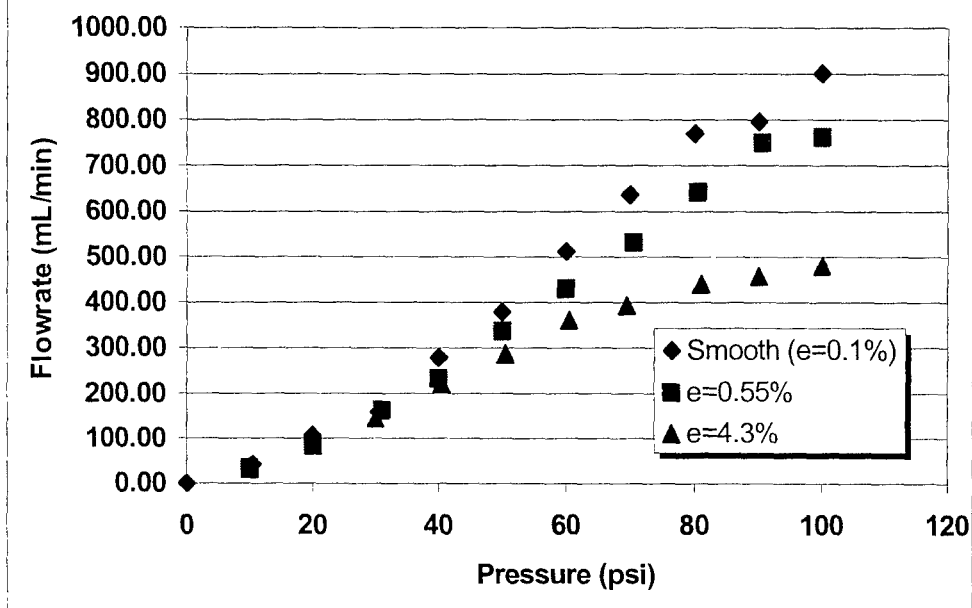


Figure A-38. Straight Channel Data: 66 μm x 600 μm , Air



Appendix 2.

Bend Data

Flow data was collected on 72 channels with varying depths, aspect ratios, bend angles, bend sharpnesses and channel lengths. The raw data from the tests are shown in the following figures, which are ordered dimensionally from the smallest to the largest hydraulic diameter. The test samples were fabricated with 8 channels, 4 with 45° bends, and 4 with 90° bends. The data for each sample is separated by test fluid, and the data for each fluid is broken out into the 45° bend data and the 90° bend data.

Approximately half of the samples were tested with water, nitrogen and FC-72. The other half were tested with water only: in these cases it was felt that conducting tests with all three fluids would be redundant and not cost effective. The table below lists the samples and figures in this bend section.

Table A-6. Summary of Bend Channel Specimens and Tests

Sample	Width	Height (μm)	Length (mm)	Fluid	Figure
K	23	128	31.75	Water	A-24
L	23	149	10.16	Water	A-26
				FC-72	A-27
				Nitrogen	A-28
				Water	A-30
M	23	172	10.16	FC-72	A-31
				Nitrogen	A-32
				Water	A-36
B	23	226	31.75	Water	A-36
N	53	235	25.4	Water	A-38
				FC-72	A-39
				Nitrogen	A-40
E	53	241	31.75	Water	A-42
F	53	344	31.75	Water	A-44
O	53	356	25.4	Water	A-46
				FC-72	A-47
				Nitrogen	A-48

Table A-7. Sample K: Data for 23 μm Channel w/5.5X Aspect Ratio
Channel Dimensions (Length = 31.75 mm)

	45° R/b=10	45° R/b=1	90° R/b=1	90° R/b=3	45° R/b=3	45° R/b =5	90° R/b=5	90° R/b=10
Depth (μm)	23	23	23	23	23	23	23	23
Width (μm)	121	140	140	121	121	140	127	114

Figure A-39. 45° Bend Data, 23 μm x 128 μm Channel, Water

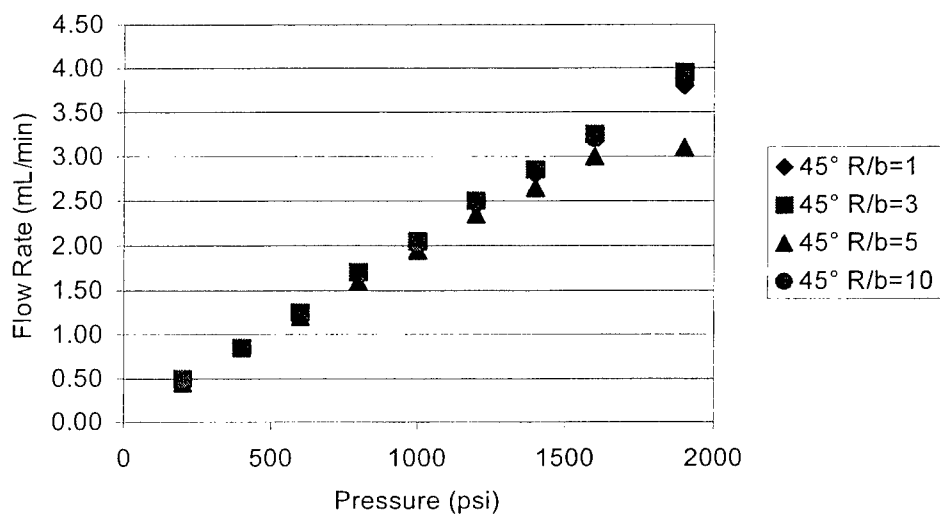


Figure A-40. 90° Bend Data, 23 μm x 128 μm Channel, Water

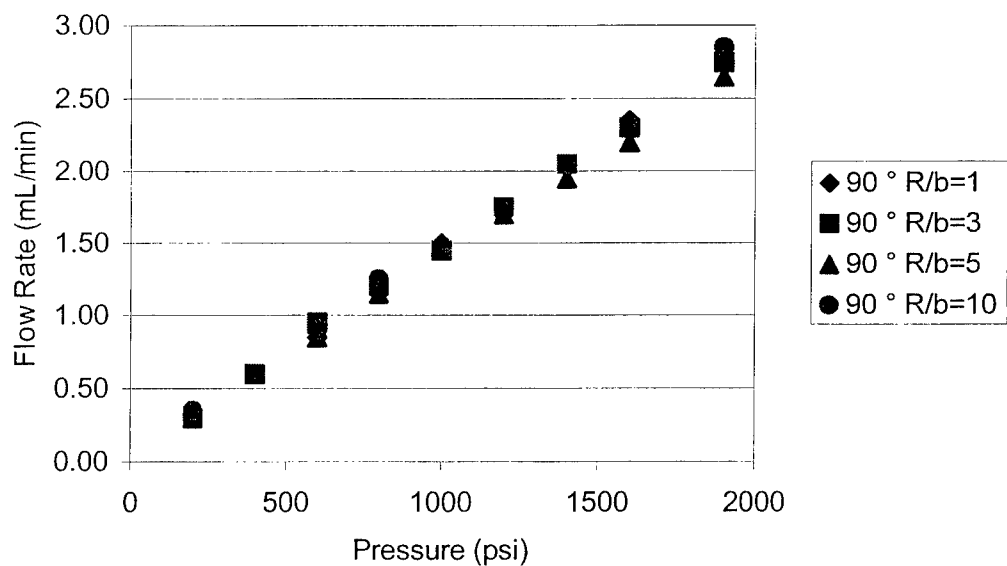


Table A-8. Sample L: 23 μm Channels w/6.5X Aspect Ratio
Channel Dimensions (Length = 10.16 mm)

	45° R/b=10	45° R/b=1	90° R/b=1	90° R/b=3	45° R/b=3	45° R/b=5	90° R/b=5	90° R/b=10
Depth (μm)	23	23	23	23	23	23	23	23
Width (μm)	140	152	140	140	178	165	140	140

Figure A-41. 45° Bend Data: 23 μm x 149 μm Channels, Water

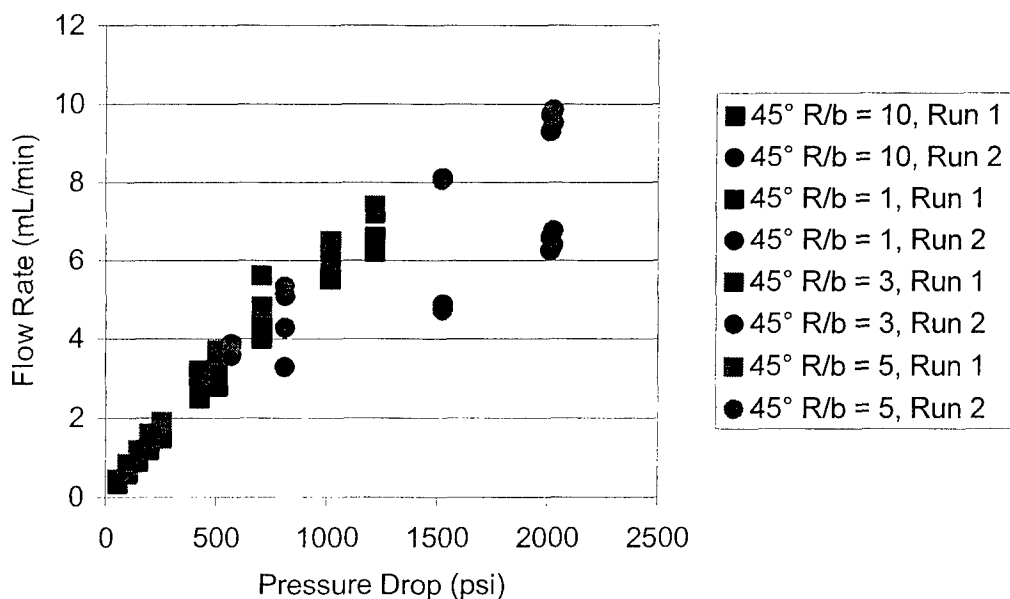


Figure A-42. 90° Bend Data: 23 μm x 149 μm Channels, Water

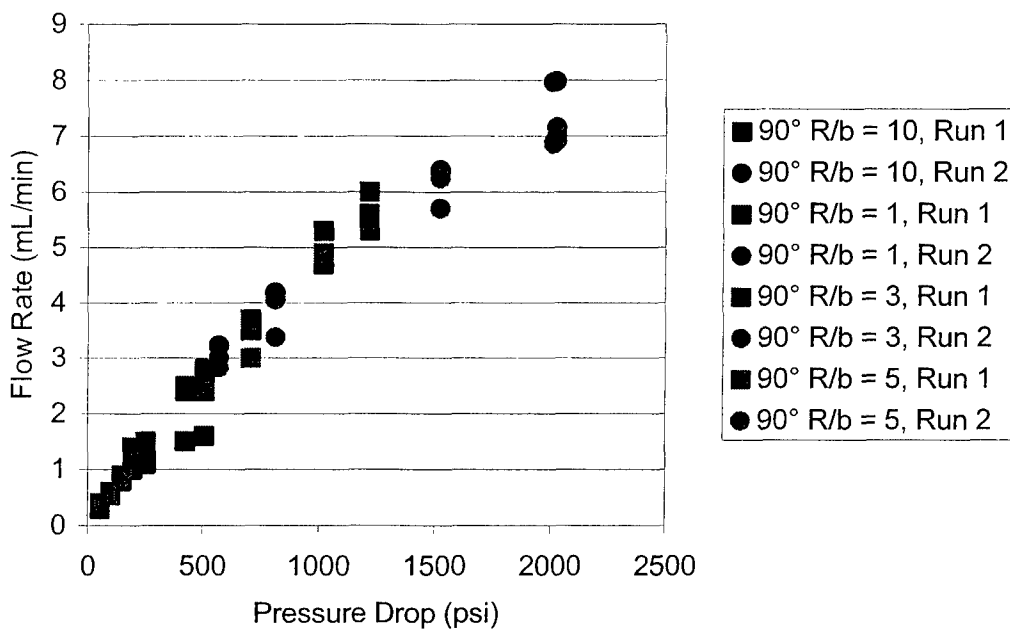


Figure A-43. 45° Bend Data: 23 μm x 149 μm Channels, FC-72

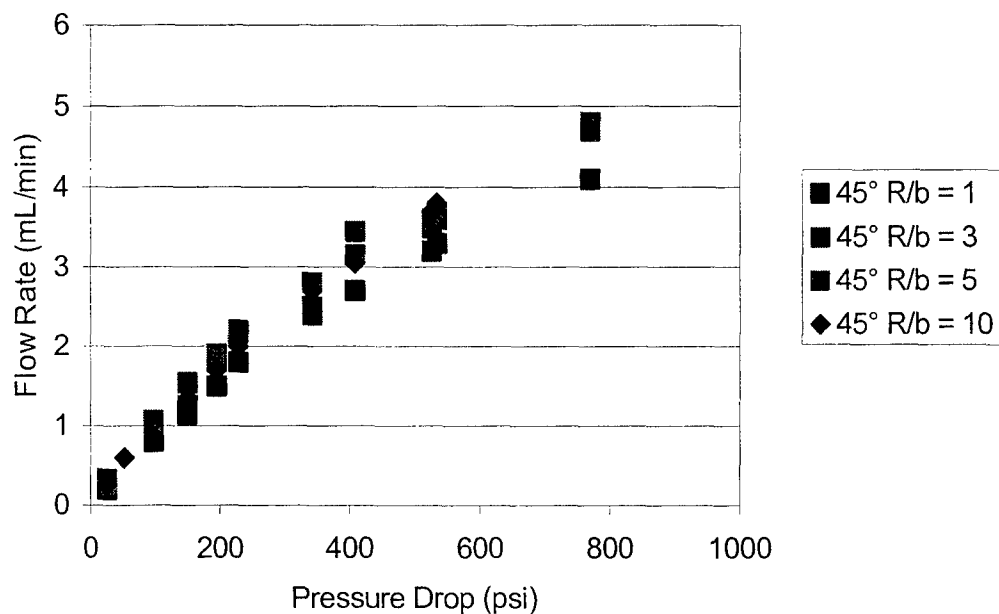


Figure A-44. 90° Bend Data: 23 μm x 149 μm Channels, FC-72

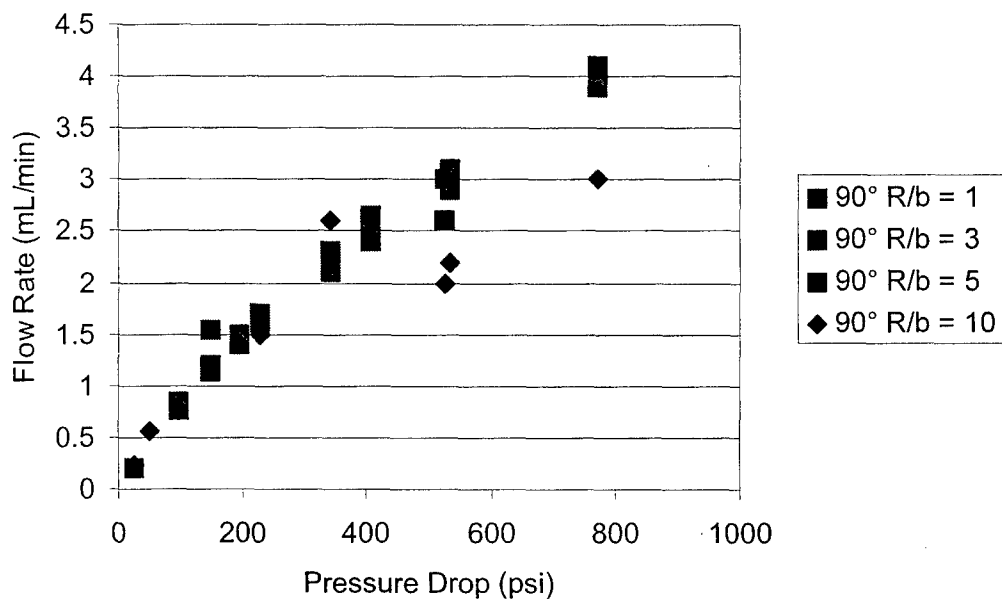


Figure A-45. 45° Bend Data: 23 μm x 149 μm Channels, Nitrogen

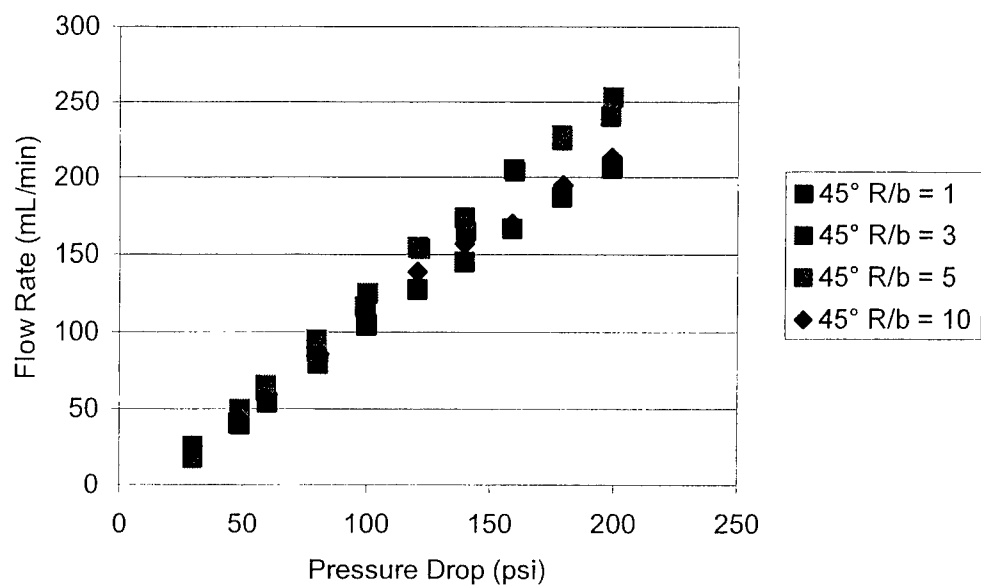


Figure A-46. 90° Bend Data: 23 μm x 149 μm Channels, Nitrogen

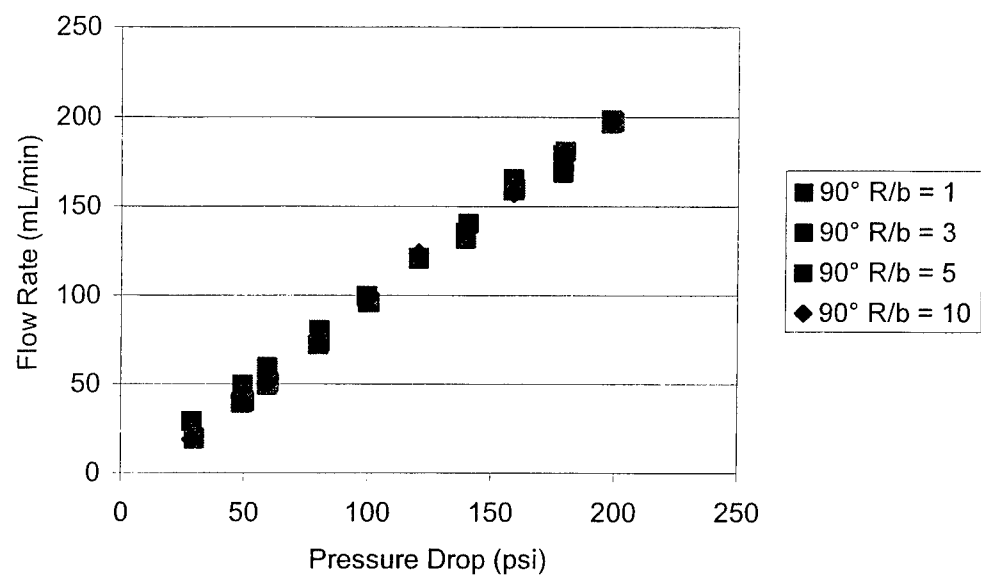


Table A-9. Sample M: 23 μm Channels w/7.5X Aspect Ratio
Channel Dimensions (Length = 10.16 mm)

	45° R/b=10	45° R/b=1	90° R/b=1	90° R/b=3	45° R/b=3	45° R/b=5	90° R/b=5	90° R/b=10
Depth (μm)	23	23	23	23	23	23	23	23
Width (μm)	178	178	165	165	178	178	165	165

Figure A-47. 45° Bend Data: 23 μ m x 172 μ m, Water

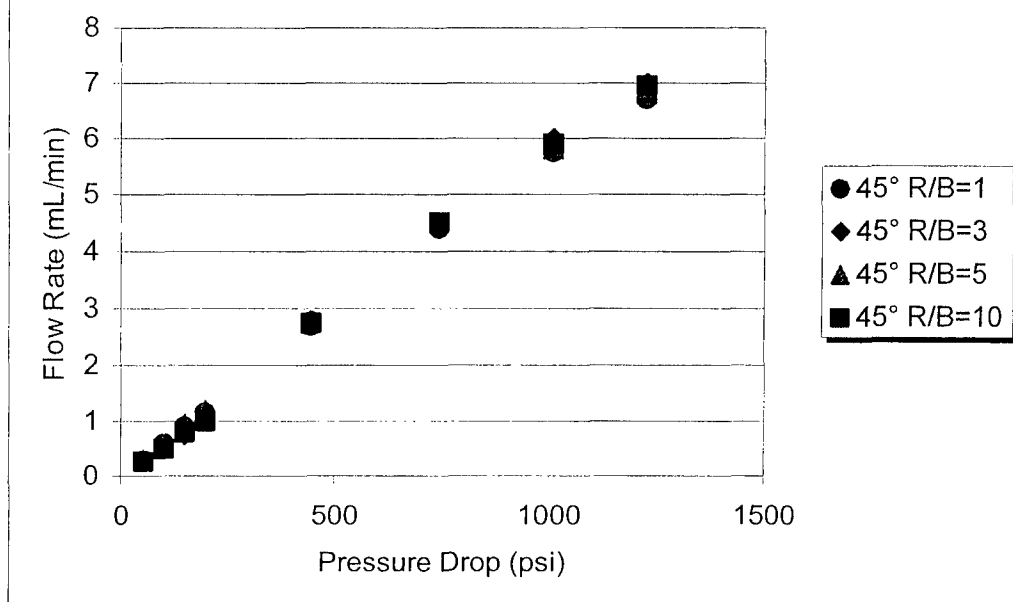


Figure A-48. 90° Bend Data: 23 μ m x 172 μ m, Water

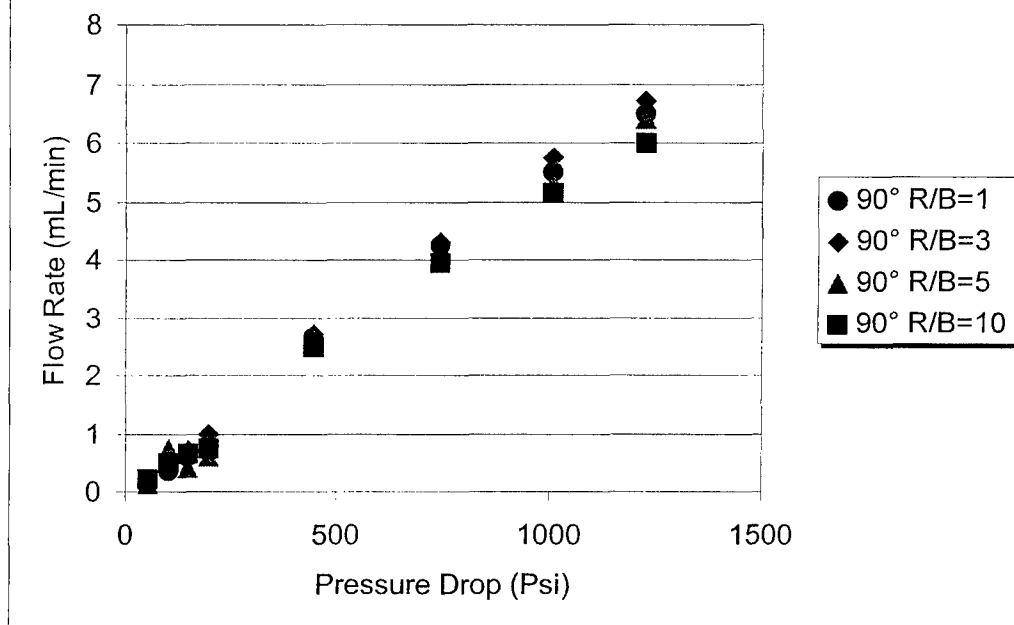


Figure A-49. 45° Bend Data: 23 μ m x 172 μ m, FC-72

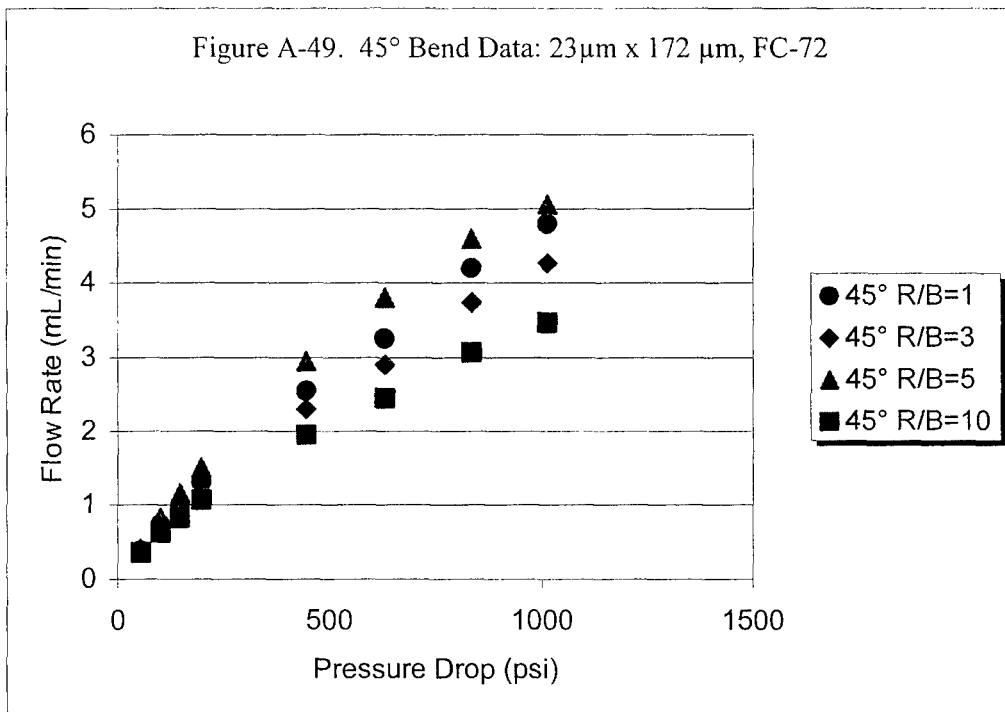


Figure A-50. 90° Bend Data: 23 μ m x 172 μ m, FC-72

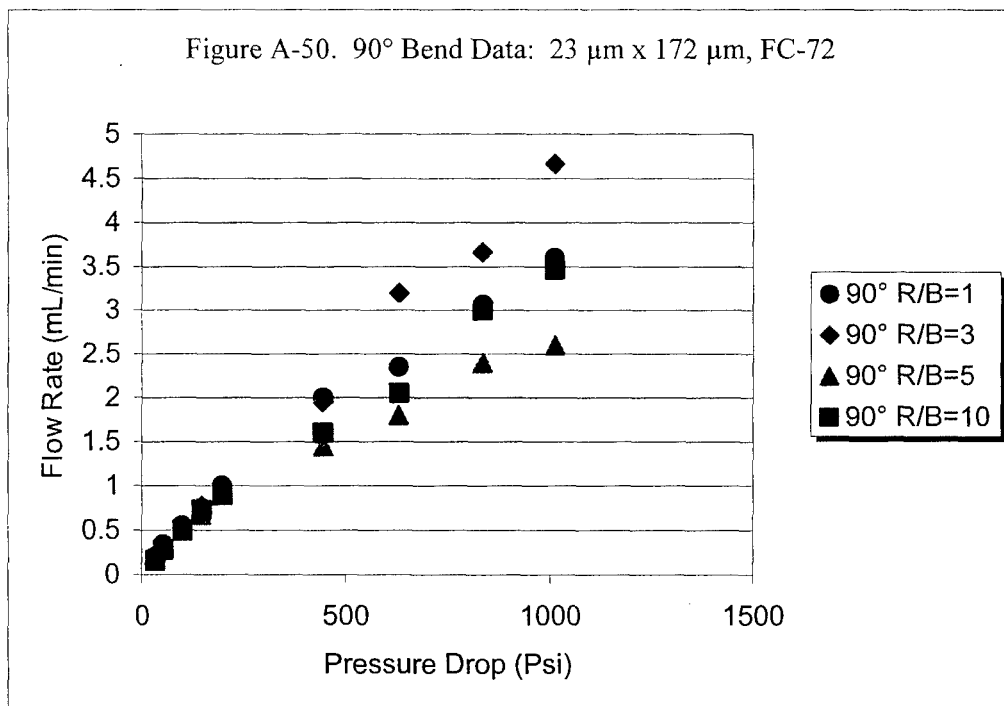


Figure A-51. 45° Bend Data: 23 μm x 172 μm , Nitrogen

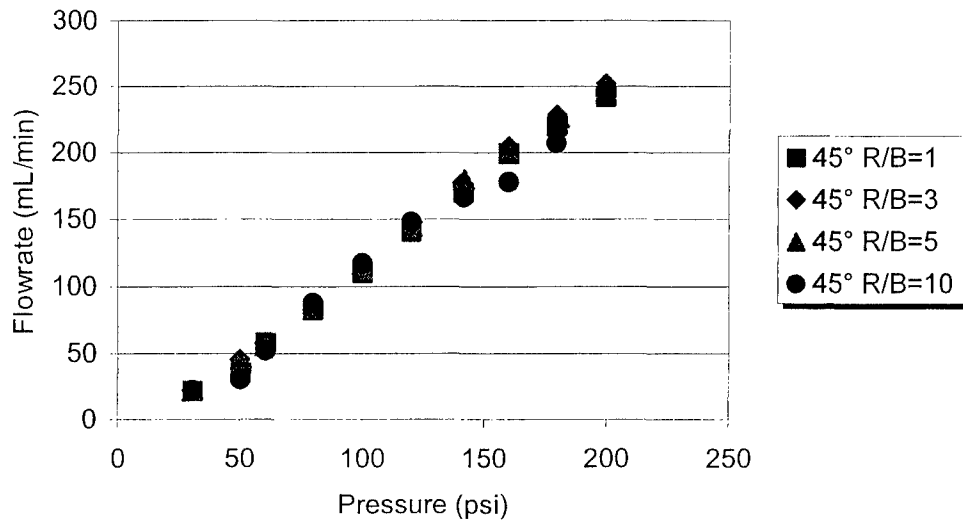


Figure A-52. 90° Bend Data: 23 μm x 172 μm , Nitrogen

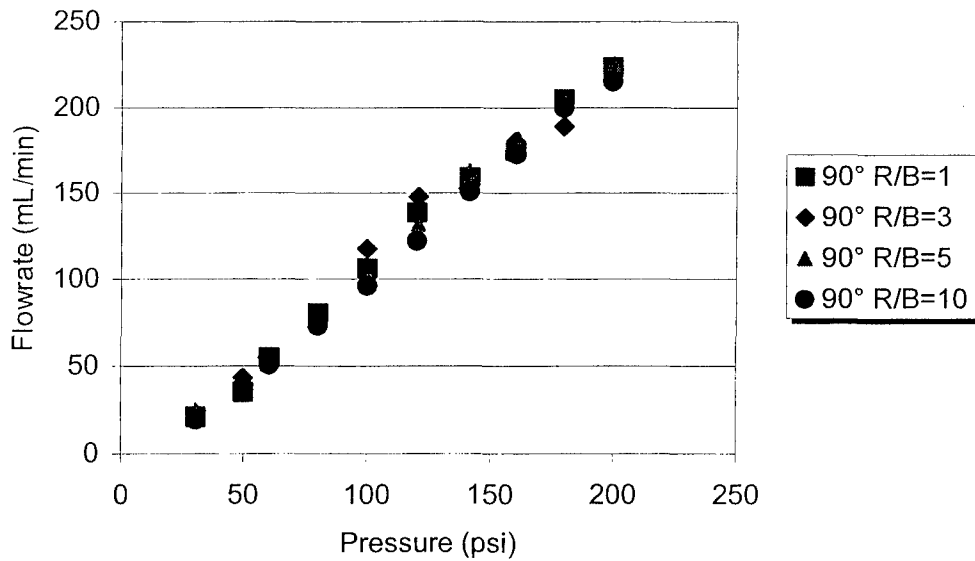


Table A-10. Sample J: 23 μm Channels w/8X Aspect Ratio
Channel Dimensions (Length = 31.75 mm)

	45° R/b=10	45° R/b=1	90° R/b=1	90° R/b=3	45° R/b=3	45° R/b=5	90° R/b=5	90° R/b=10
Depth (μm)	23	23	23	23	23	23	23	23
Width (μm)	178	204	204	184	178	191	178	165

Figure A-53. 45° Bend Data: 23 μm x 185 μm Channel, Water

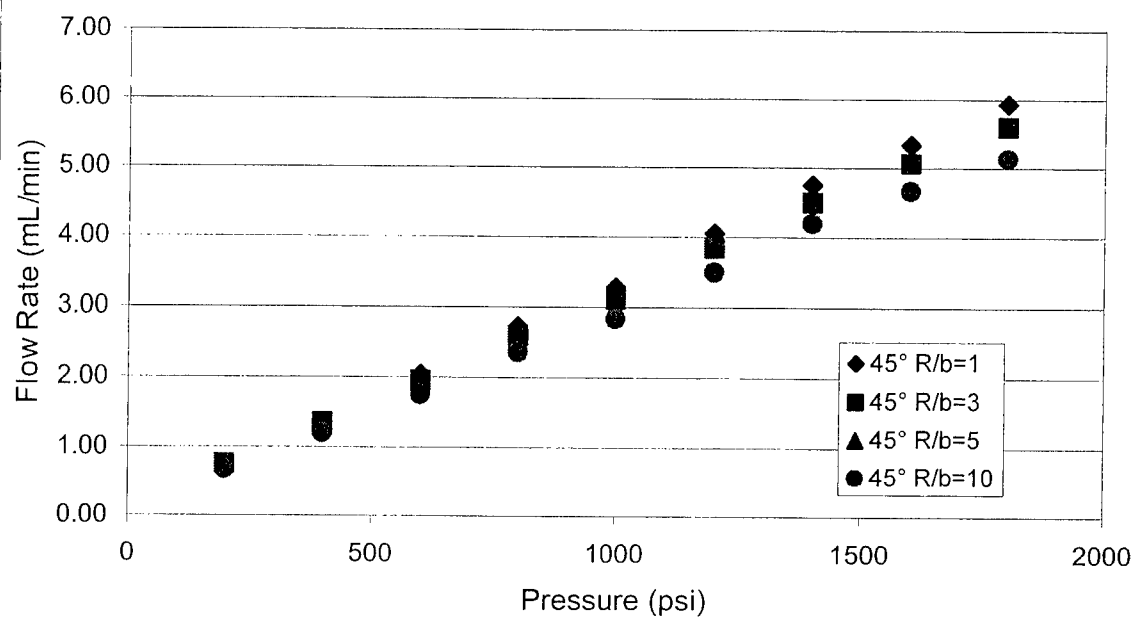


Figure A-54. 90° Bend Data: 23 μm x 191 μm Channel, Water

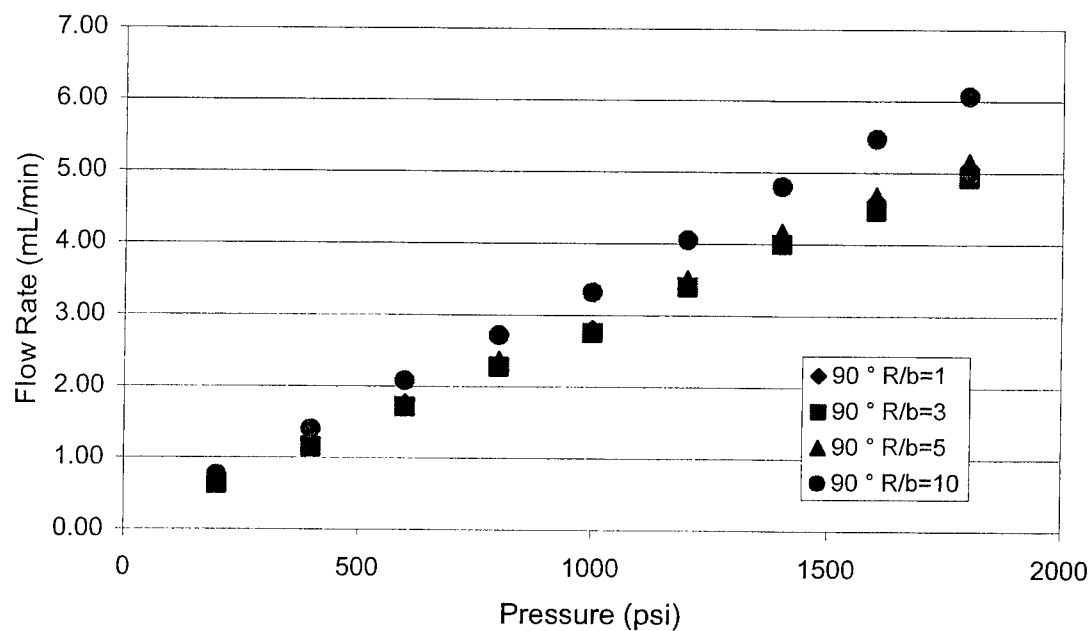


Table A-11. Sample B: 23 μm x 226 μm x 3750 μm Channels w/45° and 90° Bends

Actual Dimensions

	45° R/b=10	45° R/b=1	90° R/b=1	90° R/b=3	45° R/b=3	45° R/b=5	90° R/b=5	90° R/b=10
Depth (μm)	23	23	23	23	23	23	23	23
Width (μm)	210	229	241	216	216	241	241	216

Figure A-55. 90° Bend Data, 23 μm x 226 μm Channel, Water

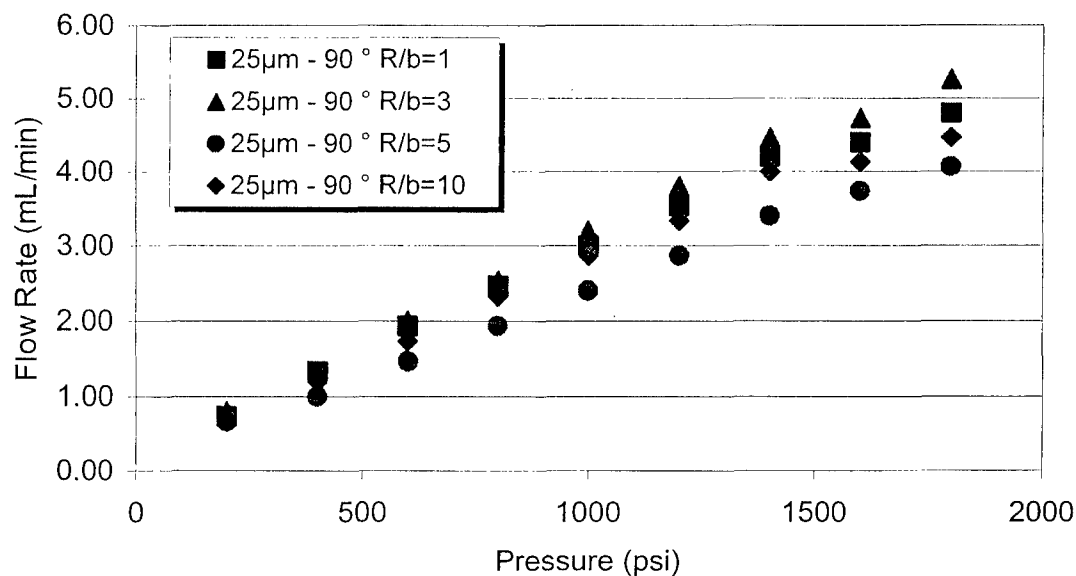


Figure A-56. 45° Bend Data, 23 μm x 226 μm Channel, Water

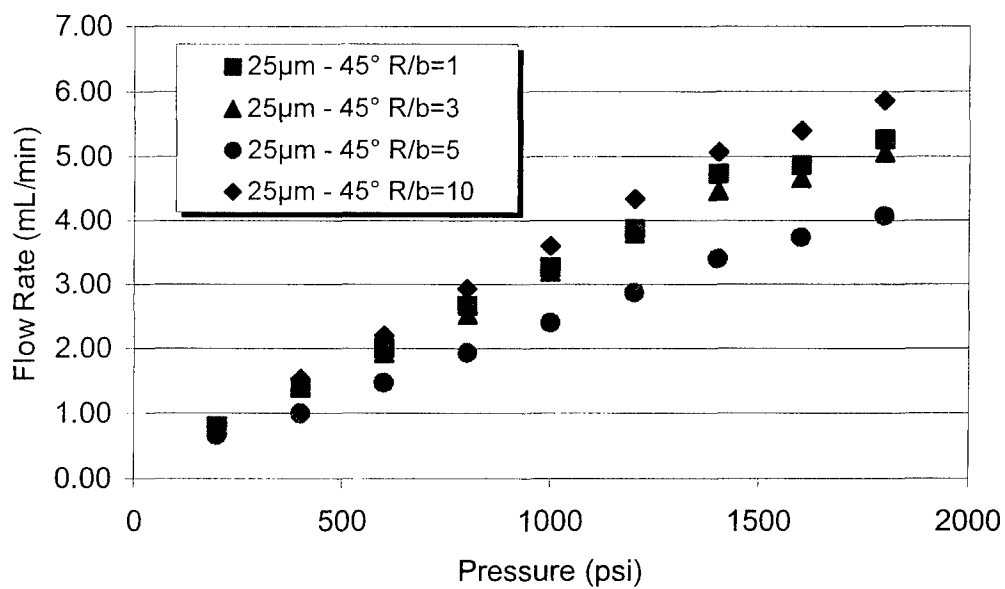


Table A-12. Sample N: 53 μm Channels w/4.5X Aspect Ratio

Channel Dimensions (Length = 25.4 mm)

	45° R/b=10	45° R/b=1	90° R/b=1	90° R/b=3	45° R/b=3	45° R/b=5	90° R/b=5	90° R/b=10
Depth (μm)	53	53	53	53	53	53	53	53
Width (μm)	248	248	229	229	229	229	229	235

Figure A-57. 45° Bend Data: 53 μm x 235 μm , Water

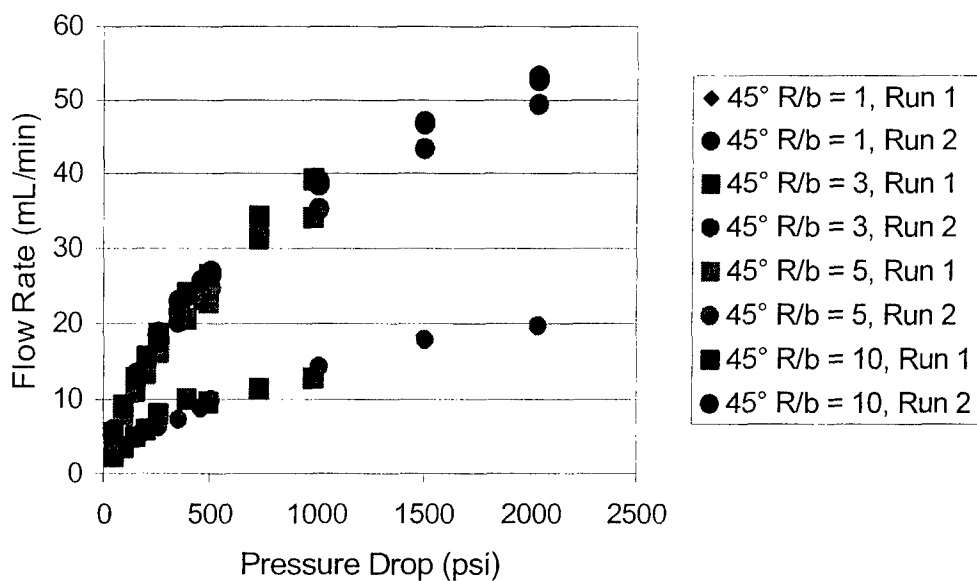


Figure A-58. 90° Bend Data: 53 μm x 235 μm , Water

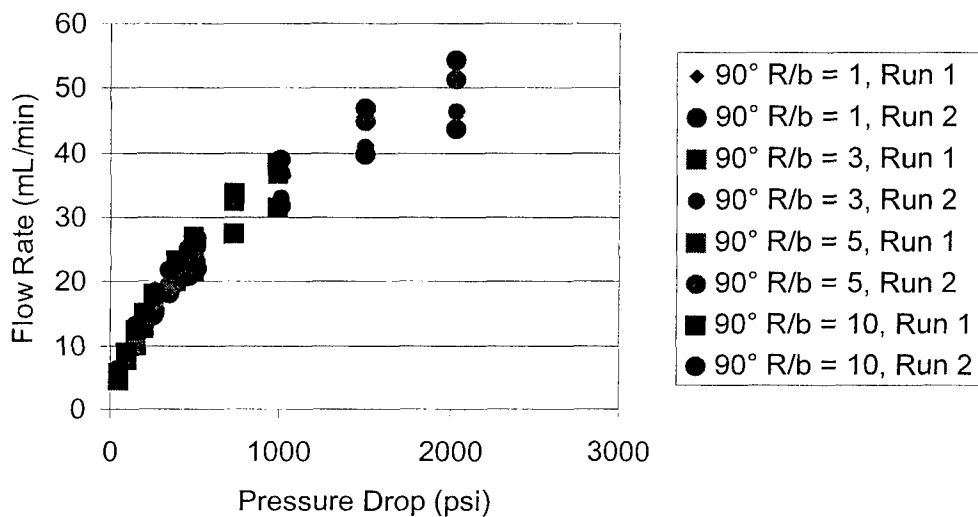


Figure A-59. 45° Bend Data: 53 μm x 235 μm , FC-72

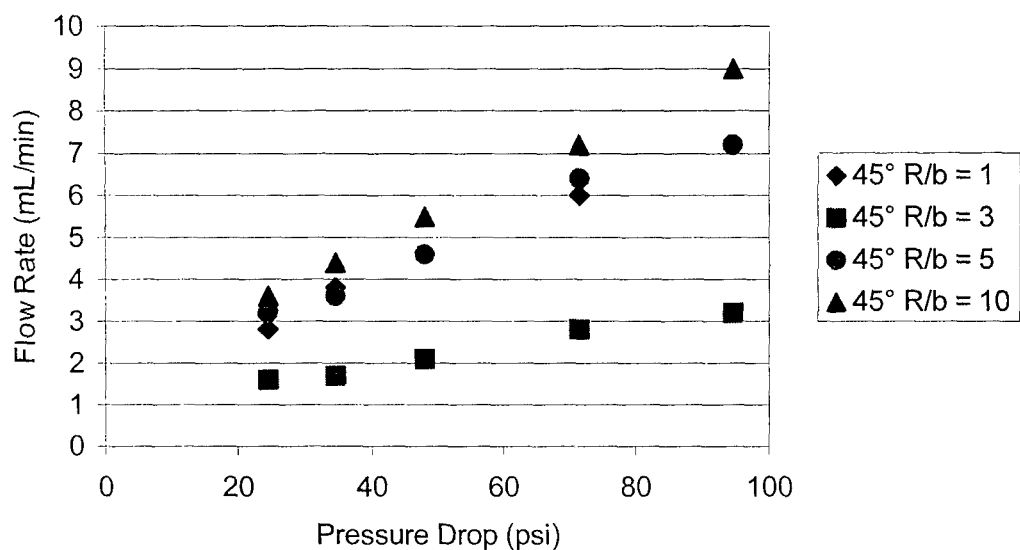


Figure A-60. 90° Bend Data: 53 μm x 235 μm , FC-72

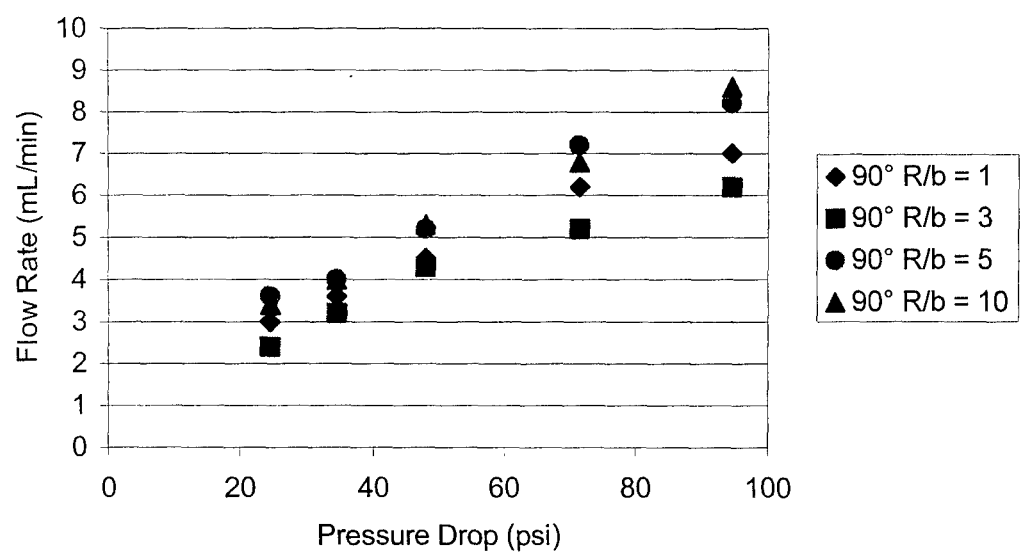


Figure A-61 45° Bend Data: 53 μm x 235 μm , Nitrogen

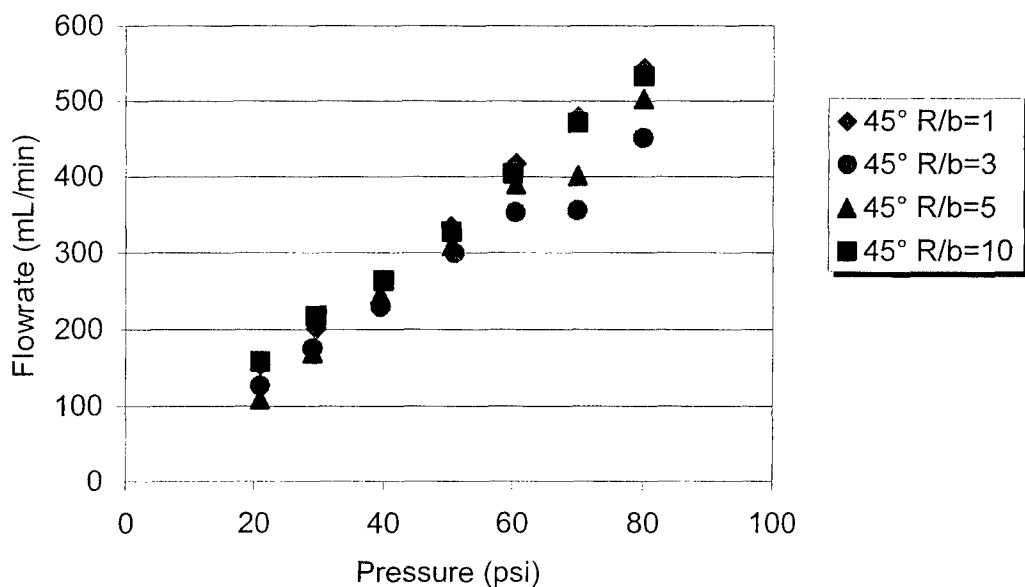


Figure A-62. 90° Bend Data: 53 μm x 235 μm , Nitrogen

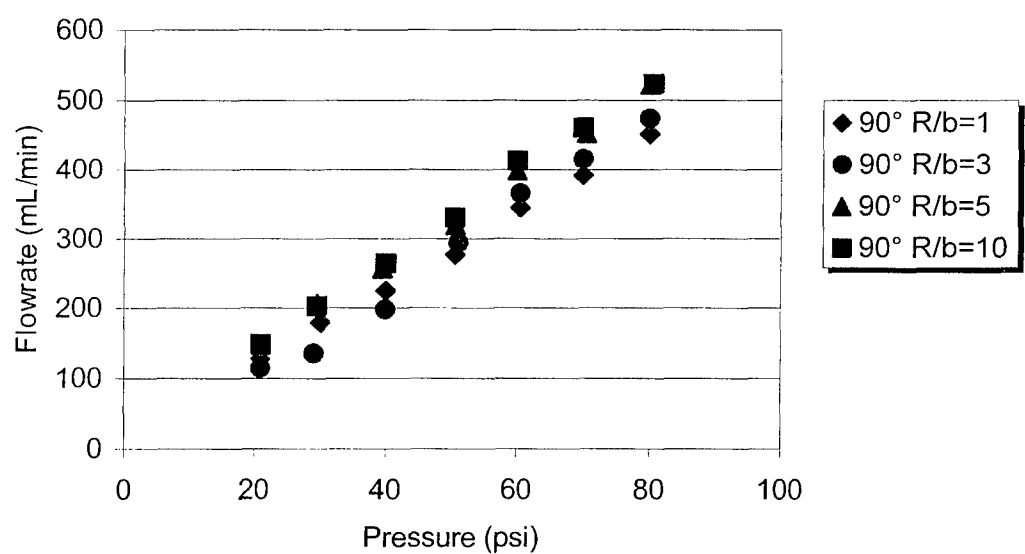


Table A-13. Sample E: 53 μm Channels w/4.5X Aspect Ratio

Channel Dimensions (Length = 31.75 mm)

	45° R/b=10	45° R/b=1	90° R/b=1	90° R/b=3	45° R/b=3	45° R/b=5	90° R/b=5	90° R/b=10
Depth (μm)	53	53	53	53	53	53	53	53
Width (μm)	235	248	235	241	229	248	248	229

Figure A-63. 45° Bend Data: 53 μm x 241 μm Channels, Water

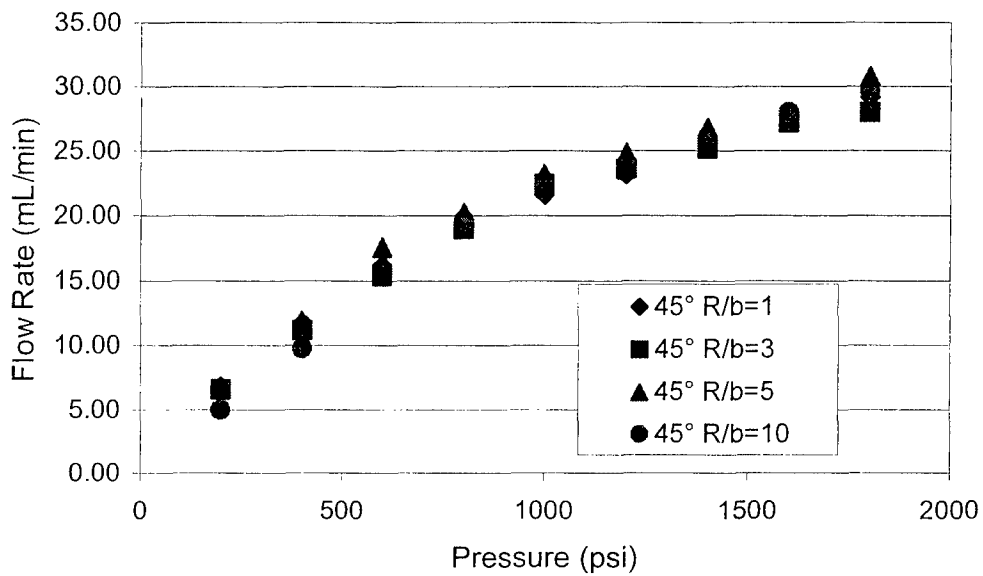


Figure A-64. 90° Bend Data: 53 μm x 241 μm Channels, Water

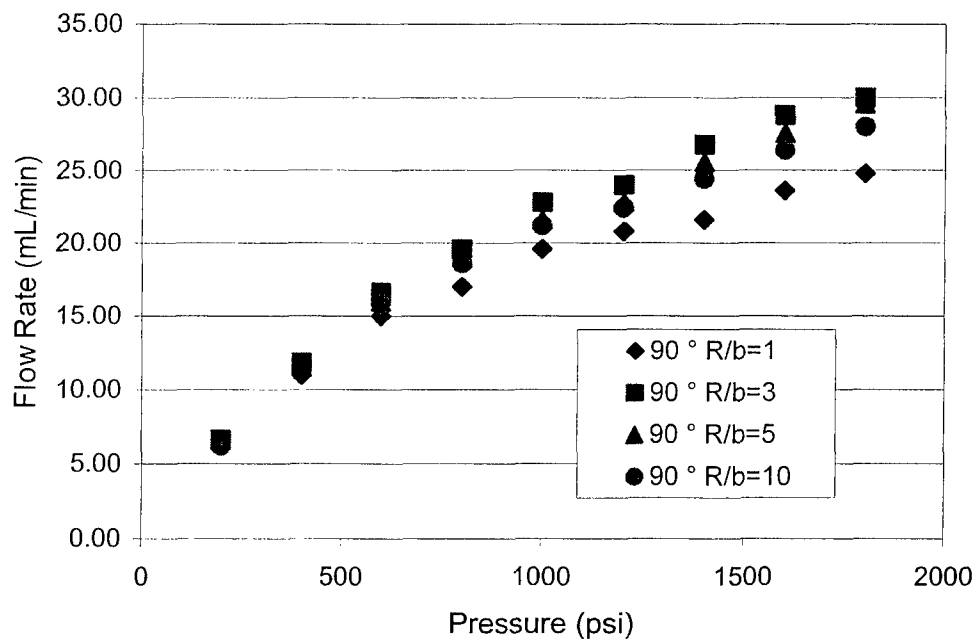


Table A-14. Sample F: 53 μm Channels w/6.5X Aspect Ratio
Channel Dimensions (Length = 31.75 mm)

	45° R/b=10	45° R/b=1	90° R/b=1	90° R/b=3	45° R/b=3	45° R/b=5	90° R/b=5	90° R/b=10
Depth (μm)	53	53	53	53	53	53	53	53
Width (μm)	337	356	343	330	330	356	362	337

Figure A-65. 45° Bend Data, 53 μm x 344 μm , Water

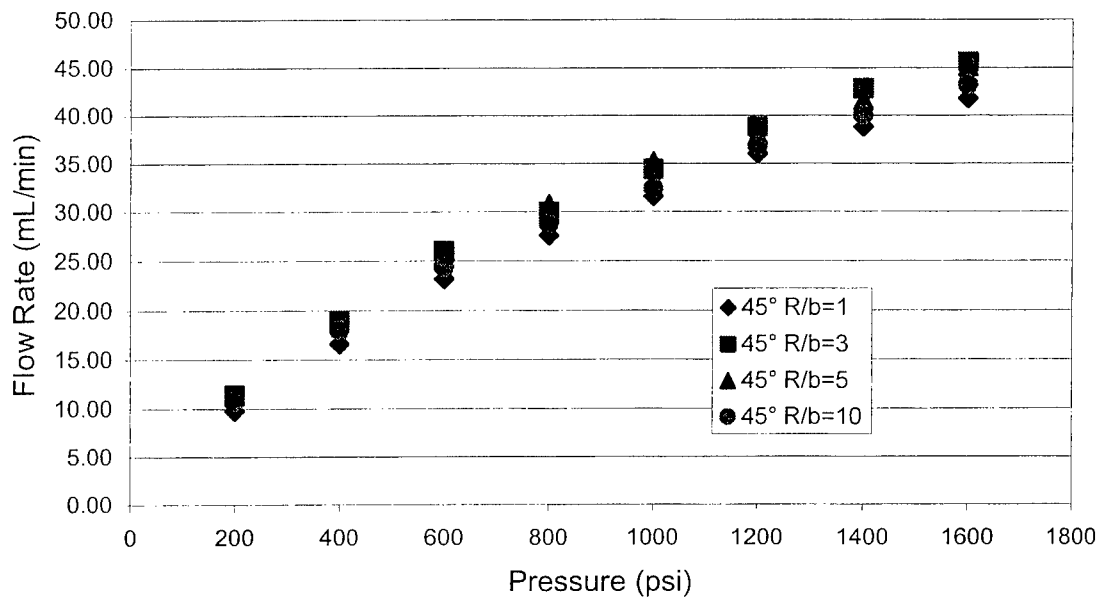


Figure A-66. 90° Bend Data, 53 μm x 344 μm , Water

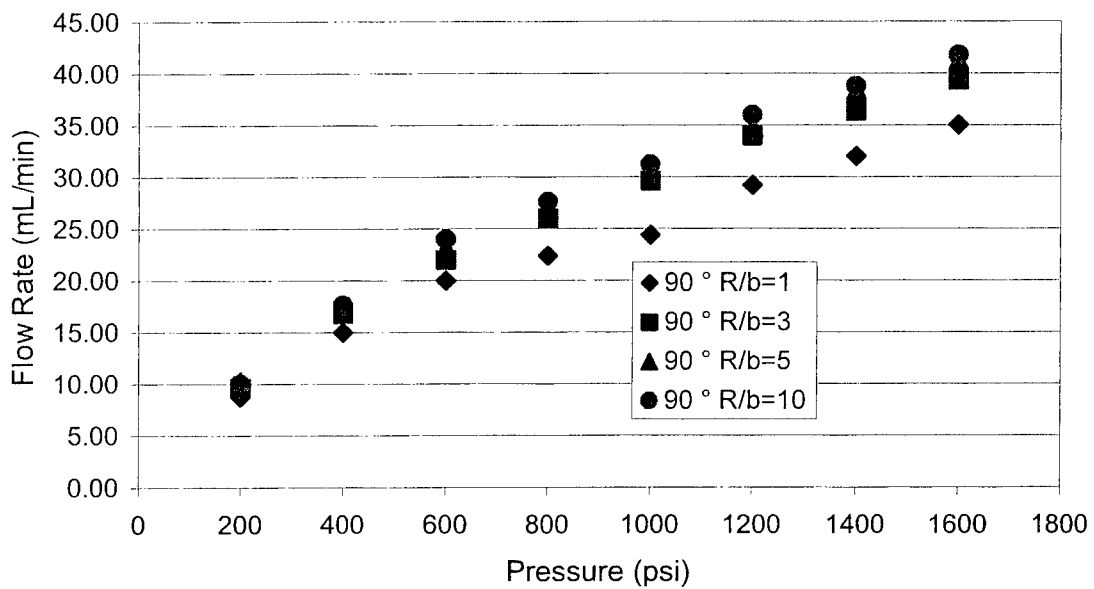


Table A-15. Sample O: 53 μm Channels w/6.5X Aspect Ratio

Channel Dimensions (Length = 25.4 mm)

	45° R/b=10	45° R/b=1	90° R/b=1	90° R/b=3	45° R/b=3	45° R/b=5	90° R/b=5	90° R/b=10
Depth (μm)	53	53	53	53	53	53	53	53
Width (μm)	356	356	356	356	356	356	356	356

Figure A-67. 45° Bend Data: 53 μm x 356 μm , Water

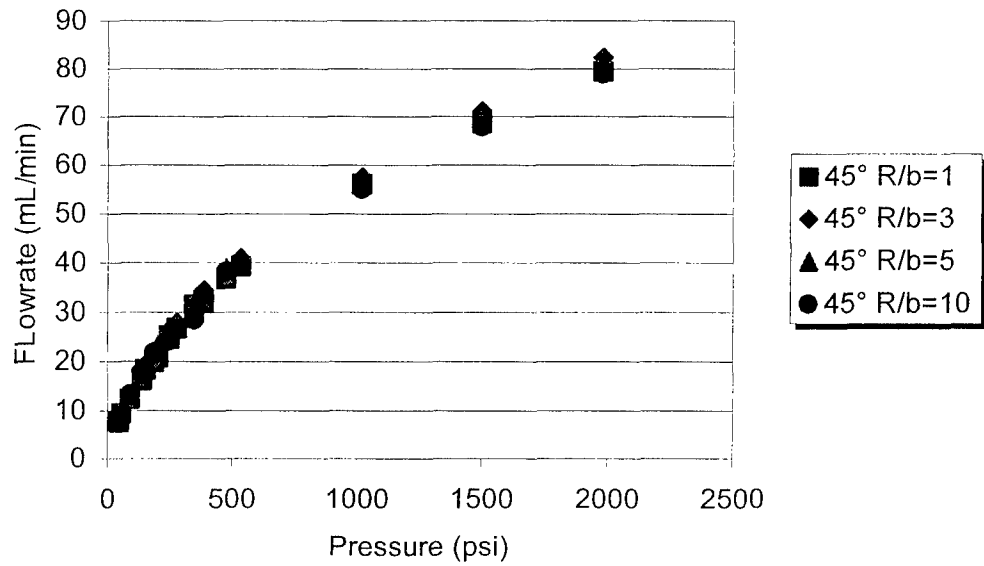


Figure A-68. 90° Bend Data: 53 μm x 356 μm , Water

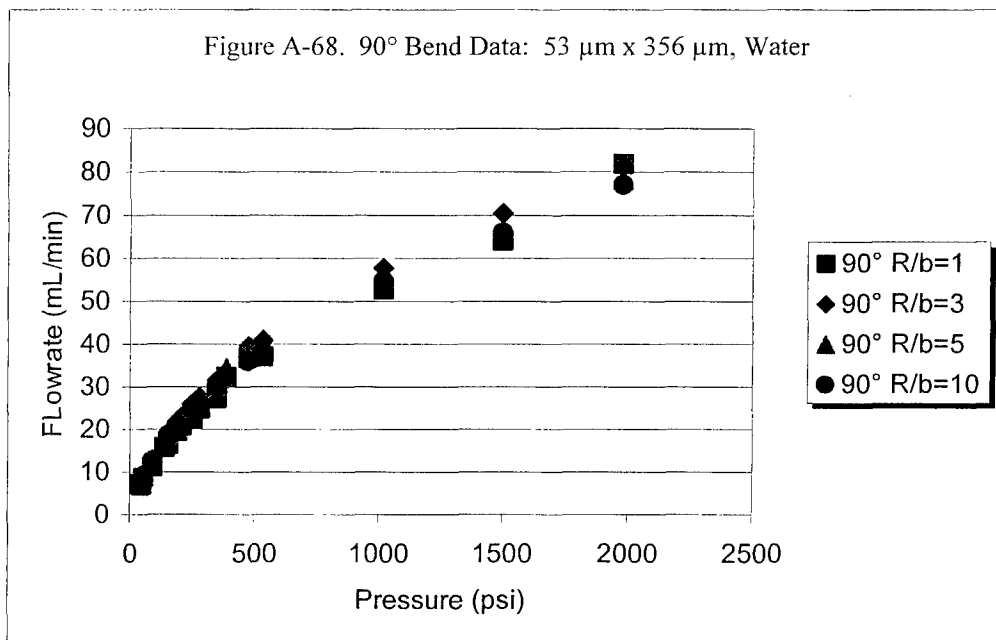


Figure A-69. 45° Bend Data: 53 μm x 356 μm , FC-72

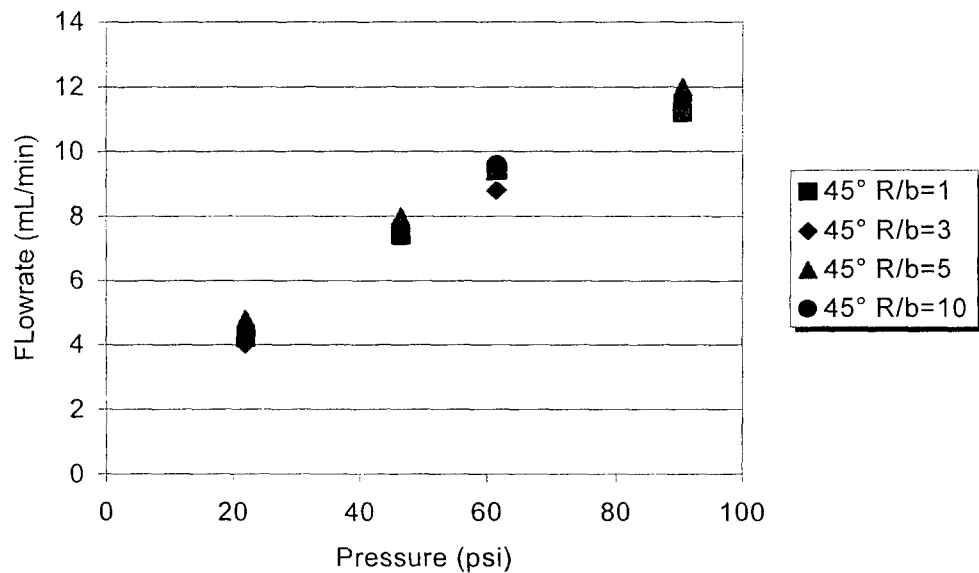


Figure A-70. 90° Bend Data: 53 μm x 356 μm , FC-72

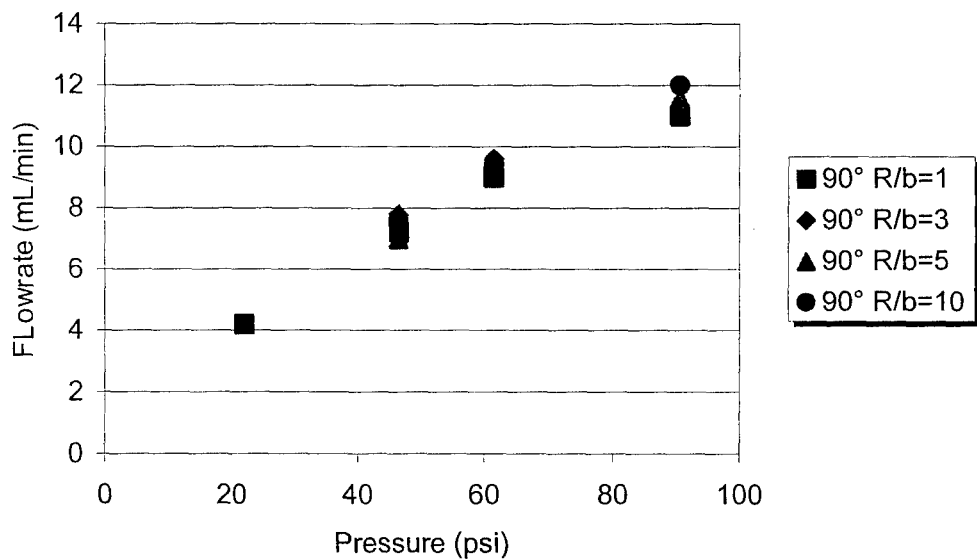


Figure A-71. 45° Bend Data: 53 μm x 356 μm , Nitrogen

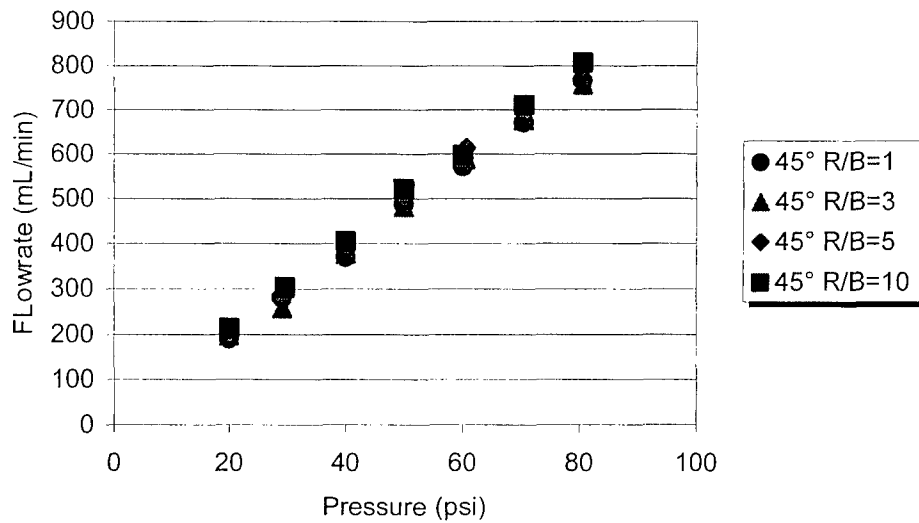
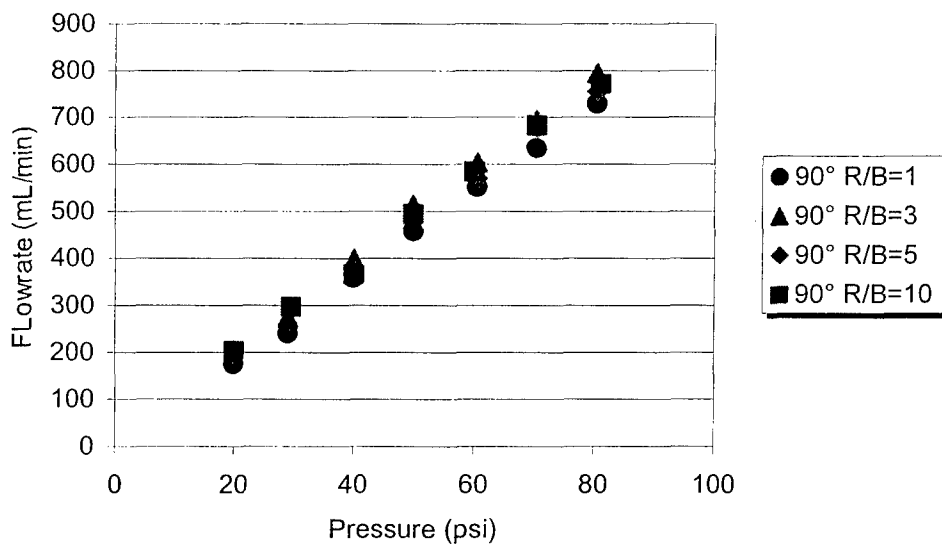


Figure A-72. 90° Bend Data: 53 μm x 356 μm , Nitrogen



List of Symbols

Symbol	Definition
f	Friction Factor
f_{lam}	Laminar Friction Factor
Re	Reynolds Number
$Re_{(Transition)}$	Transition Reynolds Number
K_{MINOR}	Minor Loss Coefficient
N_u	Nusselt Number
C_f	Empirical Constant (function of microchannel geometry)
D_h	Hydraulic Diameter
W_c	Channel to Channel Spacing
H	Channel Height
W	Channel Width
Pr	Prandtl Number
ΔT	Maximum Temperature Rise
ΔP	Maximum Pressure Rise
ρ	Density
C_p	Heat Capacity at Constant Pressure
Δp	Change in Pressure
V	Velocity
L	Passage Length
D	Passage Hydraulic Diameter
C	Geometric Constant
R	Radius of Bend
b	Width of Channel in Bending Plane
μm	Micrometer (micron)
Tee	T-Shaped Channel
Y, Wye	Y-Shaped Channel
ASME	American Society of Mechanical Engineers
psi	Pounds per Square Inch

List of Acronyms

Symbol	Definition
DARPA	Defense Advanced Research Projects Agency
AFRL	Air Force Research Laboratory
FC-72	Non-polar Liquid Fluorocarbon
MTO	Microsystems Technology Office
CAD	Computer Aided Design
MEMS	Micro ElectroMechanical Systems
MicroFlume	MicroFluidic Molecular Systems
BioFlips	Bio-Fluidic Chips
IFTC	Advanced Computing Branch, Information Directorate
LLNL	Lawrence Livermore National Laboratory
MIT/LL	Massachusetts Institute of Technology/Lincoln Laboratory
2D	Two Dimensional
3D	Three Dimensional
PAO	Polyalphaolefin
UCI	University of California, Irving
CHF ₃	Trifluoromethane (Fluoroform)
O ₂	Oxygen
°C	Degrees Centigrade
UV	Ultra Violet
SF ₄	Sulfur Tetrafluoride
HF	Hydrofluoric Acid
KOH	Potassium Hydroxide
LPCVD	Low Pressure Chemical Vapor Deposition
RMS	Rout Mean Square
PNL	Pacific National Laboratory
e/D	Roughness Ratio
μHeat	Micro Heat
L	Liter

List of Definitions

Term	Definition
Friction Factor	Complex function of system geometry, fluid properties and flow rate in a system.
Reynolds Number	Calculated by the average velocity of flow times the diameter of the tube times the mass density of the fluid divided by its absolute viscosity. At macro-scales whenever the Reynolds number is less than about 2,000, flow in a pipe is generally laminar (steady), while above Reynolds numbers of 2,000 flows are normally turbulent.
Minor Loss Coefficient	Losses in energy of a fluid due to entries, exits, fittings and valves.

***MISSION
OF
AFRL/INFORMATION DIRECTORATE (IF)***

The advancement and application of Information Systems Science and Technology to meet Air Force unique requirements for Information Dominance and its transition to aerospace systems to meet Air Force needs.